LONGITUDINAL DOUBLE-SPIN ASYMMETRIES FOR DI-JET PRODUCTION AT INTERMEDIATE PSEUDORAPIDITY IN POLARIZED P+P COLLISIONS AT $\sqrt{s}$ = 200 GEV

Ting Lin, Scott Wissink, Brian Page

Version 4.0

March 28, 2018

Contents

List of Figures

List of Tables

Chapter 1

Experiment and Data

1.1   EEMC Calibration

Endcap Electromagnetic Calorimeter (EEMC) must be calibrated in order to relate an observed ADC signal to the actual transverse energy deposited in the calorimeter. One common method used for the gain calibration of electromagnetic calorimeters is rely on the electron E/p, where the electron energy determined from the calorimeter is matched to the momentum measured by tracking chambers for identified electrons. The identification of well-known resonances, such as the π^0 through the double photons decay or Z boson via the electron and positron decay can also used for calibration. However, due to the falling TPC tracking efficiency in the EEMC region, calibration methods which rely on the TPC, such as the electron E/p method used in the BEMC, are of limited use. In addition, an absolute calibration based on the reconstruction of the neutral pion invariant mass was not practical before 2009 due to problems with the simulation of the EEMC. Given these issues, the MIP method (identify the minimum ionizing particles) was chosen for the calibration of the EEMC.

1.1.1 Calibration Overview

This method is to identify the MIPs and determine energy gains using the mean expected energy loss of a MIP passing through known thickness of scintillator. The Barrel Electromagnetic Calorimeter (BEMC) was initially calibrated using this method.

A MIP is any energetic charged hadron that passes through the detector lose it energy slowly and uniformly by ionizing atoms without depositing significant energy (that is, beyond ionization) or showering. In practice, these are mostly charged pions. MIPs are copiously produced with high purity, but there are several limitations:

1. the energy loss of a MIP in scintillator depends on the type of particles, its energy and its angles of incidence;

2. the distribution of the deposited energy inside the scintillator is not Gaussian

3. a MIP does not generate showers, so the sampling fraction is needed to get the absolute gain factors

The lack of particle identification from the TPC over a significant amount of the EEMC means that charged hadron tracks could not be tagged as possible MIP candidates, so a calorimeter based MIP identification / calibration scheme was developed. The MIPs from *pp* minimum bias events are used to set the absolute gains for all the EEMC layers including the towers, SMD strips and pre/post-shower layers. The MIP identification procedure relies on finding an isolated amount of energy, consistent with the expected MIP response, deposits in all layers of the calorimeter for a given tower. To ensure that there is only a single MIP presented, transverse isolation is enforced by requiring a coincidence of "hits" in two neighbouring SMD strips in both planes but requiring several empty strips on either side. MIP trajectory is further required to be well within the tower boundaries by using the fiducial cut by two sets of fired strips. With MIP candidates selected, the calibration of a given layer (preshower layers 1 and 2, SMD layers U and V, the postshower layer, and the entire tower) in a given EEMC tower proceeds by requiring an energy deposit consistent with a MIP in all other layers.

An "all but one" layer coincidence method are used to observe the MIP response in each layer. For example: we require that the energies deposited in the two SMD planes, the preshowers and postshowers should be consistent with a MIP in order to calibrate the corresponding towers. This method works very good with lots of layers.

1.1.2 Calibration Procedure

Firstly, in the SMD layers, we determine the strip-to-strip relative gains by fitting the slopes of ungated min-bias spectra; then use isolation cuts in U and V and tower fiducial cuts to identify the MIP candidates, there are 6912 SMD stips in total and a sample plot is shown in Fig.1.1. In this step, we assume the spectra fall off exponentially with ADC, this method works very good for the SMD relative gains among channels.
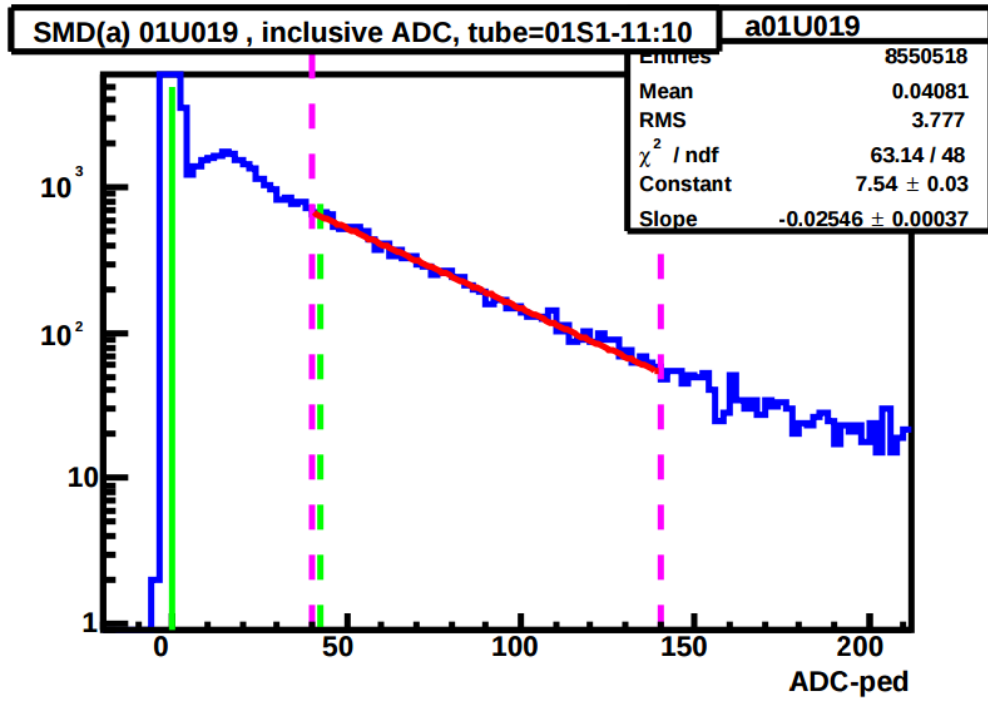
Figure 1.1: SMD ADC - pedestal spectrum

After we get the MIP candidates from SMD, gate all components in stack (SMD, pre-shower 1, pre-shower 2 , tower and post-shower) by requiring valid hits in all other components of the stack, a pure MIP sample can be identified.

3

Imposing these cuts, we can calculate the absolute gains for pre/post-showers using the Landau fit parameters. The most probable values from Landau distribution is then converted into the gains using the known factors through the formula:

$$gain_i(channel/\text{GeV}) = \frac{MPV_i \times \tanh(\eta_i)}{\Delta E_0} \tag{1.1}$$

where η_i is the pseudorapidity of the sector i, $\Delta E_0 = 5mm \times 1.8\text{MeV}/\text{cm} = 0.0009\text{GeV}$ energy loss of per plastic. A sample plot for Pre-shower 1 is shown in Fig.1.2.

Imposing the MIP cut, the absolute tower gains can be calculated using the Gaussian fit distributions, the formula is the same as the pre/post showers $gain_i = \tanh(\eta_i) \times Mean/\Delta E_0$. For tower, $\Delta E_0 = 24/5\% \times 0.4cm \times 1.8\text{MeV}/\text{cm}$ (tower has 24 layers of 4mm plastic with a $dE/dx \sim 1.8\text{GeV}/\text{cm}$ and the sampling fraction is about 5%), a sample plot is shown in Fig.1.3.

After that we get the first-pass gain which is very close to the final values with the reasonable cut setting. We can sum sets of 12 consecutive SMD strips to get the absolute SMD gains and then do another iteration, see if the deduced gains are stable.

2009 $pp200$ final tower gains as function of the rapidity bins is shown in Fig.1.4, its about 10% lower than the ideal values (Ideally, each tower HV should be adjusted so that $E_T = 60\text{GeV}$ would be in channel 4095).

The gains used in this analysis were based on 2009 MIP calibrations[1]. Data and simulation agreement is better compared to previous samples using the final 2008 gains adopted from 2006 MIP calibration as shown in Fig.1.5 and Fig.1.6.

1.1.3 Relative Gain Change

MIP calibrations produce reliable and stable results, then the relative gains can used to check the performance and stability of the EEMC system over time. As shown in Fig1.7, we separate the whole 2009 data sets by two different periods based on the time those data taken, and calibrate them individually, the y-axis is the average ratio of the MIP gains over the ideal tower gains and

Pres1(a) 01PA03 , inclusive ADC

a01PA03	
Entries	8550518
Mean	0.5907
RMS	5.789
Integral	8.548e+06
χ^2 / ndf	5745 / 2
Constant	6.546e+06 $\pm$ 3.049e+03
Mean	0.1292 $\pm$ 0.0002
Sigma	0.5182 $\pm$ 0.0002

Pres1(e) 01PA03 , ADC, tag: mipT UxV 2*thr

e01PA03	
Entries	1118
Mean	32.06
RMS	27.65
Integral	1116
χ^2 / ndf	80.59 / 58
ampl-G	112 $\pm$ 11.9
mean-G	0.3231 $\pm$ 0.1155
sig-G	1.265 $\pm$ 0.124
const-L	221.1 $\pm$ 11.0
MPV-L	20.53 $\pm$ 0.75
sig-L	8.638 $\pm$ 0.391
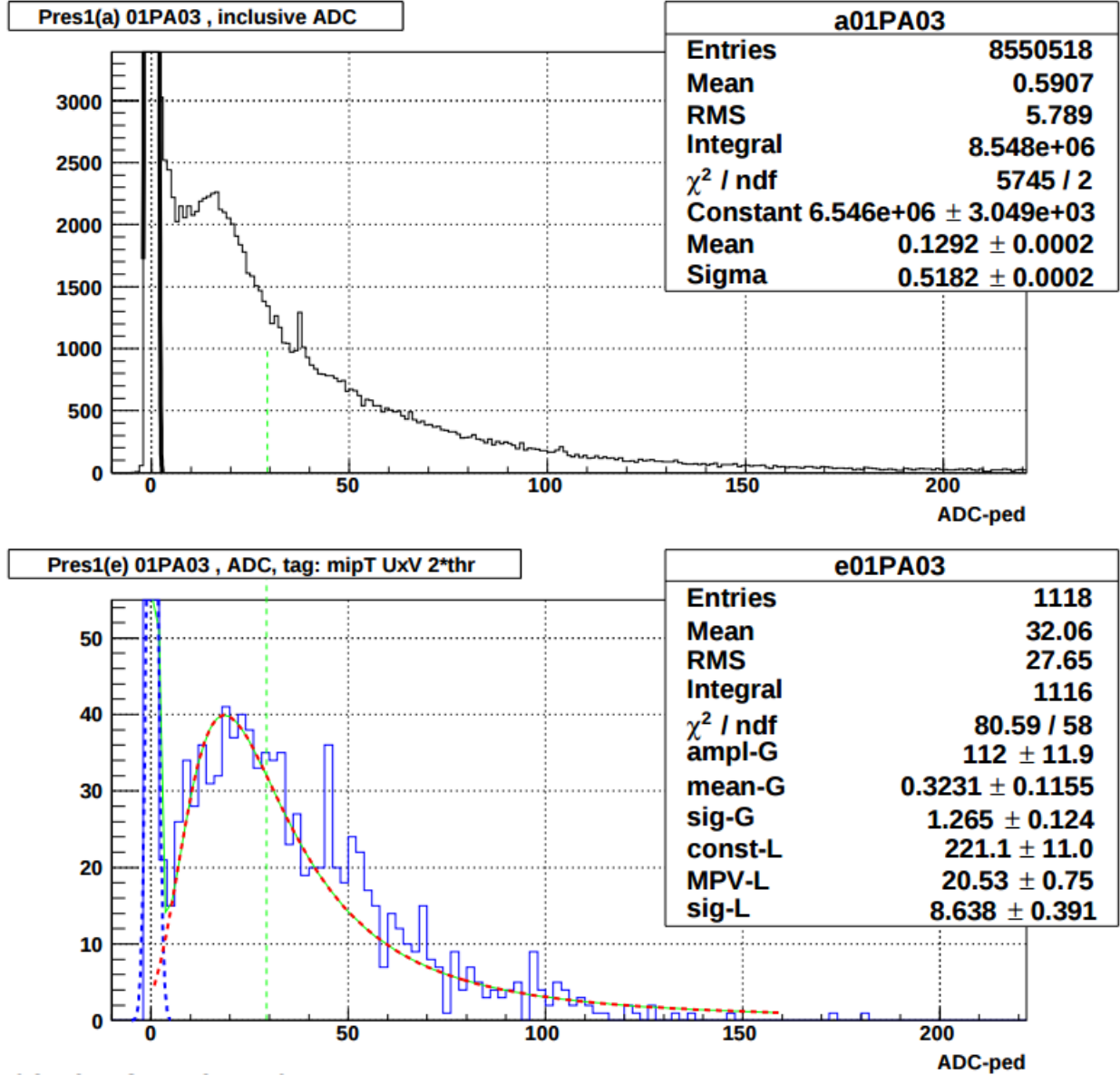
Figure 1.2: Pre-shower 1, ADC - pedestal spectrum before the MIP cuts (upper plot) and after the MIP cuts (lower plot)

the x-axis is the time of date with January 1st, 2009 as 0. We found that the EEMC gain decrease about 1% in 2009 (Fig. 1.7), this is negligible. But if we use the same method for 2012, 2013 and 2017 as shown in Fig. 1.8, in 2012 both pp200 and pp500 decrease $\sim$ 2%; but 2013, the overall decrease is about 5%. 1% increase of the EEMC high voltage would increase the gains by $\sim$ 8%. Between the 2012 pp200 and pp500, the high voltage was increased by 1% and before 2017, there is a 2% high-voltage increase on EEMC. These changes are visible in the relative gain comparison
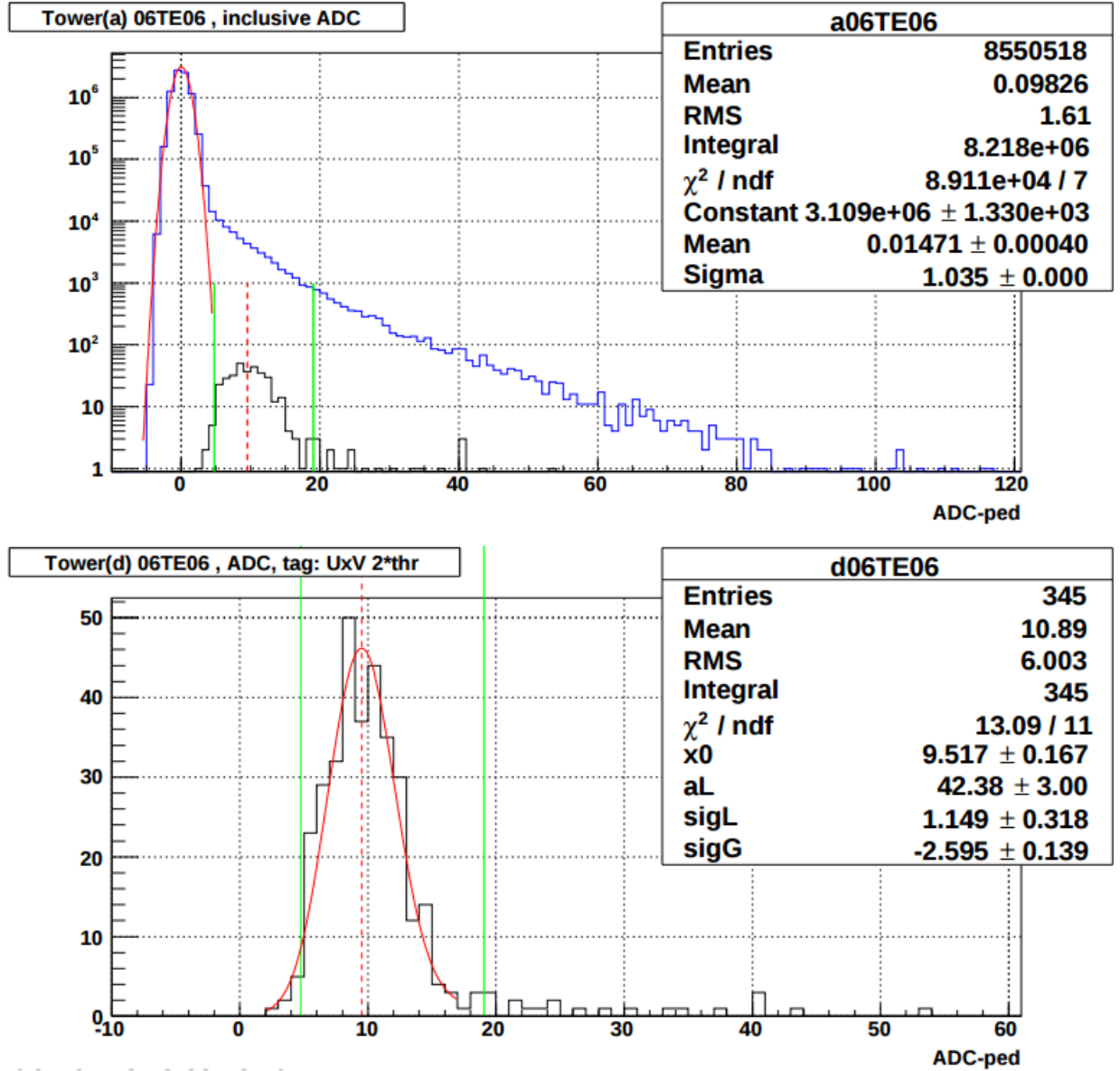
Figure 1.3: Tower, ADC - pedestal spectrum before the MIP cuts (upper plot) and after the MIP cuts (lower plot)

plots.

The reason for the gain decrease is still an unknown problem, it may related to the radiation damage of the scintilltors. Typically the EEMC gains were calculated and used through the whole data set every year. With the fact that gain would change over time, and due to the limited statistic, a slightly different approach was proposed. After the 2012 $pp500$, for a given tower, calculate its average gain from entire data set, and then split entire days of running period into four equal

2009 Final EEMC tower gains from MIPs w/ UxV
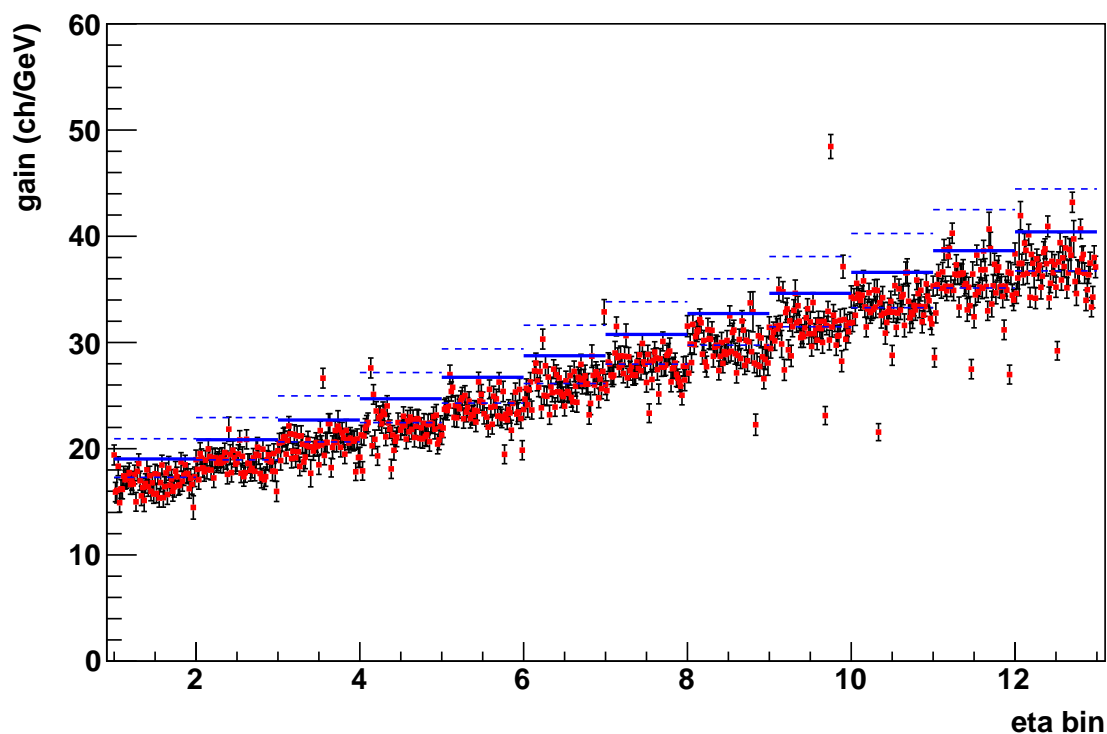
Figure 1.4: 2009 pp200 final tower gains vs. eta bins
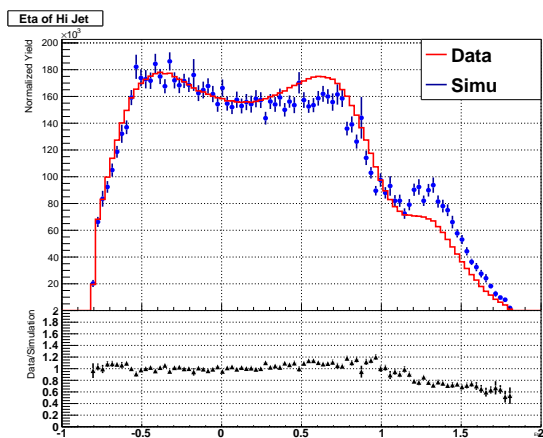
Figure 1.5: Jet Eta distribution using 2006 EEMC gains
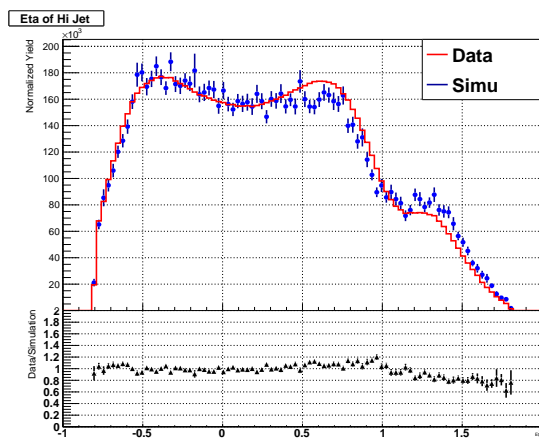
Figure 1.6: Jet Eta distribution using 2009 EEMC gains

quarters, extrapolate the tower gains at middle of each quarter using the slope of fit line and the average gains. The final values in the EEMC official database is the 4 gain sets with 4 different timestamp, which means the real data taken at different time would use different gain factors.
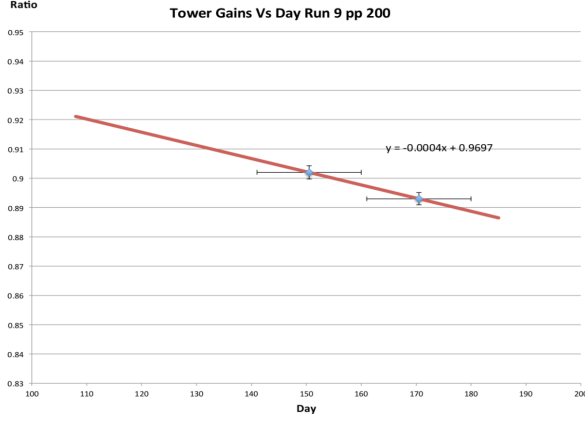
Figure 1.7: 2009 $pp200$ EEMC Relative Gain Comparison
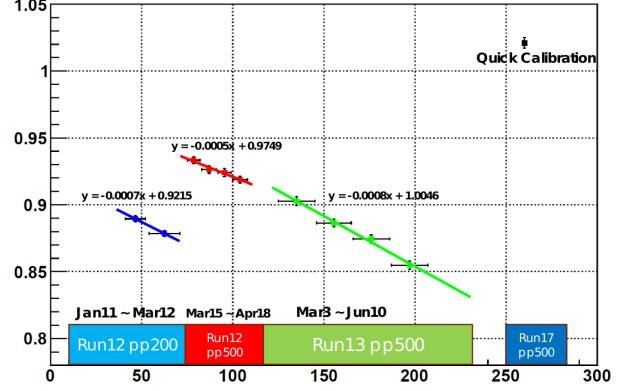
Figure 1.8: 2012, 2013, 2017 EEMC Relative Gain Comparison

1.2 Data Sample

The data used in this analysis were recorded by the Solenoidal Tracker at RHIC (STAR) collaboration in 2009 at $\sqrt{s}$ = 200 GeV with 21 pb^{-1} integrated luminosity. The luminosity-weighted polarizations of the two beams were P_B = 56% and P_Y = 57%. The STAR detector subsystems used to reconstruct jets are the Time Projection Chamber (TPC) and the Barrel and Endcap Electromagnetic Calorimeters (BEMC, EEMC) [4]. The TPC provides charged particle tracking in a 0.5 T solenoidal magnetic field over the nominal range $|\eta| \leq 1.3$ in pseudorapidity and 2π in azimuthal angle. The BEMC and EEMC are segmented lead-scintillator sampling calorimeters, which provide full azimuthal coverage for $|\eta| < 1$ and $1.09 < \eta < 2$, respectively. The calorimeters measured electromagnetic energy deposition and provided the primary triggering information via fixed $\Delta\eta \times \Delta\phi = 1 \times 1$ calorimeter regions (jet patches). A jet patch trigger was satisfied if the transverse energy in a single jet patch exceeded either 5.4 GeV (JP1 trigger, prescaled) or 7.3 GeV (JP2 trigger), or if two jet patches adjacent in azimuth each exceeded 3.5 GeV (AJP trigger). In addition, the Beam-Beam Counters (BBCs) [25] were used in the determination of the integrated luminosity and, along with the zero-degree calorimeters (ZDCs) [4], in the determination of helicity-dependent relative luminosities.

The duration from when the beams are fully injected into the rings to when the beams are

8

dumped is called a RHIC fill and data samples was divided into different runs which are taken for a certain period for different fills. Same run list is used as 2009 dijet measurements at Mid-Rapidity [8], see the appendix A.

1.2.1 Data Quality Assurance

The run selection and QA were done during the 2009 dijet measurement at mid-rapidity. It was completed in several steps. Firstly, a list that contains runs longer than 3 minute and inlude the TPC, BEMC and EEMC were created. This list includes a sets of diagnostic by STAR collaborations during the data taken. Then only those with the trigger setups: production2009_200Gev_Hi, production2009_200Gev_Lo, and production2009_200Gev_Single were retained. The trigger setup denotes the specific triggers included in the data: production2009_200Gev_Hi contains only the L2JetHigh triggered events, production2009_200Gev_Lo contains only the JP1 triggered events, and production2009_200Gev_Single contains both 2JetHigh and JP1 triggered events.

Run by run QA were also done by looking at the various quantities of interest to the analyses, for example the number of reconstructed tracks or the energy deposited in the calorimeter. Individual runs for which the per event mean of some quantity deviates more than 5σ from the global means are discarded. Furthermore, runs that do not have associated polarization values, the relative luminosity and valid spin bit values are also not used, as these information is essential for double spin asymmetry calculation. Finally we get a list of runs that has 888 runs from 2009 pp200.

1.2.2 Trigger System

The STAR Trigger [12] is designed to facilitate the related heavy ion researches and the quest to understand the interior of hadrons. It is a multi-level, modular, pipelined system in which digitized signals from the fast trigger detectors are examined at the RHIC crossing rate and then the information is used to determine whether to begin the amplification-digitization-acquisition (ADA) cycle for slower, more finely grained detectors which provide the information where the interested physics lies in. In this analyses, the relevant trigger system are the Level 0 and Level 2.

9

Level-0

Level-0 is the 1st layer of trigger electronics which consists of a tree of Data Storage and Manipulation (DSM) boards and a Trigger Control Unit (TCU). It processes the trigger data for every RHIC crossing and only accept the event that is interested to initiate the data taking. The detector front-end electronics that feeds Level-0 is spread out over the several detectors and crates. The decision of the trigger was based on deposition energy in fixed regions of BEMC and EEMC which are called jet patches when triggering on jets, and there are 30 jet patches in 2009 configuration as shown in table.1.1. The trigger logic gets the ADC sum from the jet patch towers and compared to the trigger thresholds, events passing the thresholds were recorded.

ϕ Location	BEMC East $-1 < \eta < 0$	BEMC Middle $-0.6 < \eta < 0.4$	BEMC West $0 < \eta < 1$	EMC Overlap $0.4 < \eta < 1.4$	EEMC $1 < \eta < 2$
10 o'clock (150°)	BEMC-JP6	BEMC-JP12	BEMC-JP0	Overlap-JP0	EEMC-JP0
12 o'clock (90°)	BEMC-JP7	BEMC-JP13	BEMC-JP1	Overlap-JP1	EEMC-JP1
2 o'clock (30°)	BEMC-JP8	BEMC-JP14	BEMC-JP2	Overlap-JP2	EEMC-JP2
4 o'clock (−30°)	BEMC-JP9	BEMC-JP15	BEMC-JP3	Overlap-JP3	EEMC-JP3
6 o'clock (−90°)	BEMC-JP10	BEMC-JP16	BEMC-JP4	Overlap-JP4	EEMC-JP4
8 o'clock (−150°)	BEMC-JP11	BEMC-JP17	BEMC-JP5	Overlap-JP5	EEMC-JP5

Table 1.1: 2009 jet patch geometry

There are three different thresholds used for the trigger decision. JP2, JP1 or JP0 bits are set separately if the ADC sum of the jet patch is above the highest, middle or lowest thresholds. The jet patch thresholds were changed over the course of Run 9 to normalize yields across the BEMC and EEMC. It was believed the latter had lower gains. The jet patch threshold changes are summarized in table 1.2, the equivalent transverse energy is approximated by $E_T \approx 0.236 \times (ADC - 5) GeV$. The Adjacent Jet Patch (AJP) were implemented here for the jet patches overlapping in the ϕ direction, and it is set if two of the 24 BEMC and EEMC jet patches (no EMC overlapping) that is adjacent in ϕ fire the lowest threshold. In this jet analyses, we only interested in the JP2, JP1 and AJP triggers.

Label	set 1 (ADC)	set2 (ADC)	set 1 $E_T(GeV)$	set 2 $E_T(GeV)$
BEMC-JP-th0	20	20	3.5	3.5
BEMC-JP-th1	28	28	5.4	5.4
BEMC-JP-th2	36	36	7.3	7.3
EMC-overlap-JP-th0	20	19	3.5	3.3
EMC-overlap-JP-th1	28	26	5.4	5.0
EMC-overlap-JP-th2	36	34	7.3	6.8
EEMC-JP-th0	20	18	3.5	3.1
EEMC-JP-th1	28	25	5.4	4.7
EEMC-JP-th2	36	32	7.3	6.4

Table 1.2: 2009 jet patch thresholds. Set 1 ends with run 10125061.

Level-2

The events that are accepted by Level 0 ultimately reach Level 2 where they undergo more detailed analysis. This level is entirely software based and more sophisticated triggering algorithm can be implemented here. L2 Trigger presented in this analyses is the L2JetHigh that contains event in which the JP2 or AJP bits are set. The algorithm also look for energy deposit in 1×1 regions in the calorimeters but with a much finer granularity than the 30 fixed jet patches at L0. It scans 330 unique 5×5 areas of the calorimeter, and find two 1×1 regions of the detector separated at least 30 degree away in ϕ which contain the most energies.

There are three trigger categories here: monojet, dijet and random. Monojet trigger is satisfied if the high patch transverse energy is above the threshold, typically set around 6.5 GeV; the dijet trigger is fired if both patches are above a dijet thresholds which are somewhat lower than the monojet threshold. There are three sets of dijet thresholds and which set is used is based on the sum of the energy weighted η positions of the two patches. This functionality was included because patches at forward pseudorapidities tend to have lower transverse energies so lower thresholds are needed in the forward region to keep the dijet accept rate somewhat constant across the detector. The random trigger accepts random events at a set rate regardless of whether or not the event would have passed either the monojet or dijet conditions. A given event can satisfy multiple L2Jet trigger categories simultaneously but events which do not satisfy any of the above categories are dropped and not used in these analysis.

Chapter 2

Jet and Di-jet

Almost every event of interest at high-energy colliders contains collimated collections of particles known as jets. Due to the color confinement, a parton radiates gluons and further splits into other gluons and quark-antiquark pairs as it moves out from the collision point. The quarks and gluons then hadronize into color-neutral objects, some of which decay into stable or metastable particles which can be measured in the experiments. The radiation is predominantly in the direction of the original hard parton; thus the 4-momentum sum of the final state particles should approximate the 4-momentum of the hard parton that was originally produced in the collison, which provide a window into short-distance physics. Jets are produced through the fragmentation and hadronization of the hard scattered partons, which reflects the configuration of quarks and gluons at short distances. These are important observables, both in Standard Model studies and in searches for physics beyond the Standard Model [10].

2.1 Jet Reconstruction

Jets are the collimated sprays of hadrons that result from the fragmentation of a high-energy quarks or gluons, and so one can probe the behavior of the original 'parton' that produced them by measuring the jet 4-momentum. The properties of the jets must be well defined and reproducible in order to be used. A jet definition includes its algorithms, parameters, and recombination scheme,

which can be applied equally to experimental information such as calorimeter towers and charged particle tracks, final state particles, or the partonic events of perturbative QCD calculations [30].

2.1.1 Jet Algorithms

Most jet algorithms belong to one of two broad classes: sequential recombination algorithms and cone algorithms. Sequential recombination algorithms usually identify the pair of particles that are closest in some distance scale, estimate their total transverse momentum p_T, recombine them, and then repeat the procedure over and over again, until some stopping criterion is reached. Cone algorithms put together particles within specific conical angular regions, adjusting them such that the momentum sum of the particles contained in a given cone coincides with the cone axis [17].

Typically the algorithms are required to be infrared and collinear (IRC) safe, which means if one modifies an event by a collinear splitting or the addition of a soft emission, the set of hard jets that are found in the event should remain unchanged. This safety is important in several ways. Firstly, a hard parton undergoes many collinear splittings as part of the fragmentation process and the non-perturbative dynamics also lead to collinear splittings. There is always some emission of soft particles in QCD events, both through perturbative and non-perturbative effects. Secondly, the divergence cancellation between real and virtual corrections in fixed-order perturbative QCD calculations may be broken by an IRC unsafe jet algorithm. Furthermore, because of the finite resolution and non-zero momentum thresholds, the experimental detectors themselves also provide some regularization of collinear and infrared unsafety.

The STAR jet analyses have mainly used two different algorithms in their results. Before the 2009 run analysis, inclusive jet results [3] [5] used the midpoint cone algorithm; for all later runs the inclusive jet [7] and dijet [8] analyses used the anti-k_T algorithm.

Midpoint Cone

The midpoint cone algorithm is a cone algorithm originally used by the CDF and D∅ groups for their Run II jet analysis [13]. Cone algorithms form jets by associating together particles that

lie within a cone of a specific radius in $\eta \times \phi$ space around the energy-weighted centroid as shown in equation 2.1.

$$\eta^C = \frac{\sum_{i \subset C} E_T^i \eta^i}{E_T^C}, \qquad \phi^C = \frac{\sum_{i \subset C} E_T^i \phi^i}{E_T^C}, \qquad E_T^C = \sum_{i \subset C} E_T^i. \qquad (2.1)$$

The algorithm begins by collecting a list of individual particles from tracks and fired towers which serve as seeds for the initial jet cones or proto-jets when passing through the cone algorithm. Then additional proto-jets are formed from the midpoints between seeds within a distance $\Delta R < 2R$ and added to the list; in this stage individual particles can be shared by several proto-jets. At the splitting and merging stage, the jet algorithm decides whether to split or merge two proto-jets with overlapping cones. The decision is based on the fraction of energy shared by the lower p_T proto-jet. Proto-jets that share a fraction greater than f (50%) would be merged, while the others would be split, with the shared particles individually assigned to the proto-jet that is closest in $\eta - \phi$ space. The algorithm always works with the highest E_T proto-jet, and the ordering of the list is checked after each instance of merging or splitting.

Anti-k_T Algorithm

This algorithm is a sequential recombination algorithm that repeatedly combines pairs of particles which are closest to each other. It was introduced and studied in Ref. [16]. This algorithm introduces the distance d_{ij} between entities (particles, pseudojets) i and j and d_{iB} between entity i and the beam (B):

$$d_{ij} = min(1/p_{ti}^2, 1/p_{tj}^2) \frac{\Delta R_{ij}^2}{R^2}$$

$$d_{iB} = 1/p_{ti}^2, \qquad (2.2)$$

where $\Delta R_{ij} = \sqrt{(\eta_i - \eta_j)^2 + (\phi_i - \phi_j)^2}$ and p_{ti}, η_i and ϕ_i are respectively the transverse momentum, rapidity and azimuth of particle i. R is the radius parameter of the jets in $\eta - \phi$ space. In this analysis R is set to 0.6. This algorithm finds the distances d_{ij} and d_{iB} for all the particles and pairs, and then identifies the minimum value. If the minimum value is d_{ij}, then it recombines the

14

two particles i and j, and recalculates d_{ij} and d_{iB}. If the minimum value is d_{iB}, then particle i is a final state jet and it is removed from the list of particles. The distances are recalculated and the procedure repeated until no entities are left. The anti-k_T algorithm essentially behaves like an idealised cone algorithm, and is less susceptible to diffuse soft backgrounds from underlying event and pile-up contributions. These latter concerns will be discussed in later chapters.

2.1.2 Jet Selection

The jet reconstruction procedures follow those used in the 2009 inclusive jet analysis [7]. Jets were found using the anti-kT algorithm [15] implemented in the FastJet [17] package, with resolution parameter R = 0.6. In addition to the jet algorithm's parameters, there are other requirements imposed on the TPC tracks and calorimeter towers which serve as input to the jet algorithm at the detector level.

Track Conditions

Tracks with $p_T \geq 0.2$ GeV/c and pseudorapidy η between -2.5 and 2.5 were analyzed. The tracks are also required to contain more than 5 fit points in the TPC, and > 51% of the maximum number of fit points allowed by the TPC geometry and active electronic channels. A p_T-dependent DCA cut (distance of closest approach) is applied, where the DCA is the distance between the event vertex and the charged particle track trajectory at the point when the trajectory is closest to the vertex. This helps reduce the pile-up effect. This cut retains tracks with a DCA < 2 *cm* for track p_T below 0.5 GeV/c, and DCA < 1 *cm* for p_T above 1.5 GeV/c. This cut is linearly interpolated in the intermediate p_T region.

The charged particle tracks are reconstructed when the ionization electrons they produce as they traverse the TPC volume drift to the endcaps and avalanche onto readout pads. These pads are situated in rows (padrows) oriented roughly perpendicular to a straight radial line emanating from the interaction point. A fit point is any padrow that contributes to a track in order for it to be reconstructed. The condition on the number of fit points differs from the 2009 inclusive jet analysis,
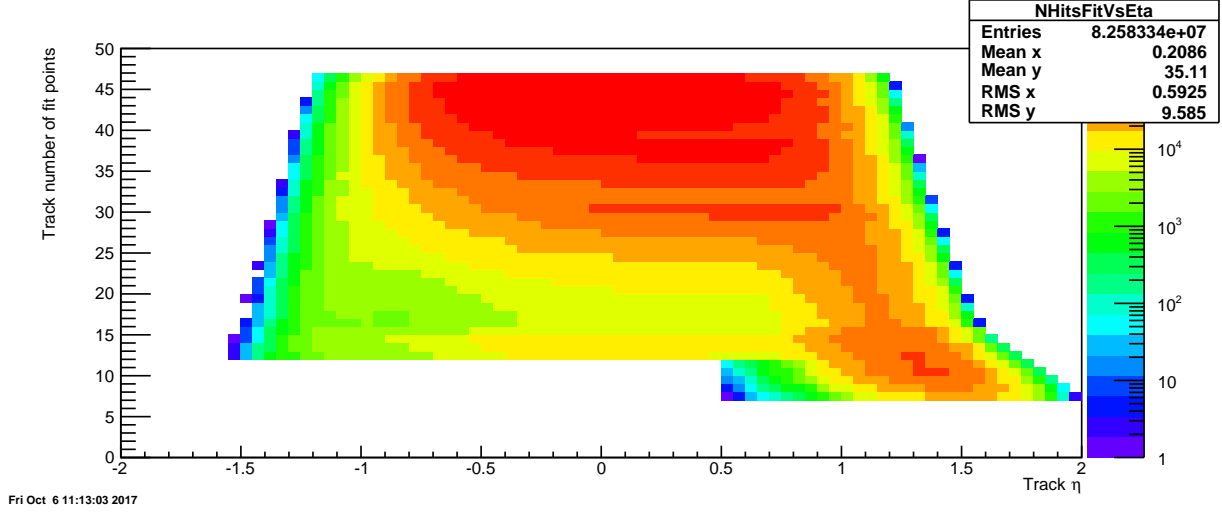
Figure 2.1: Track: number of fit points vs. η from data.
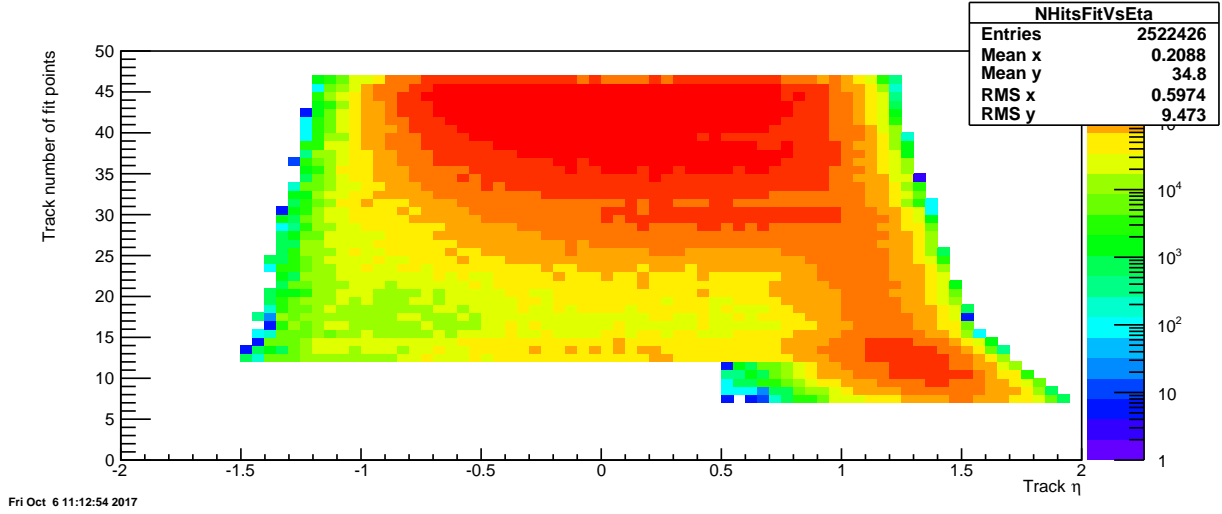
Figure 2.2: Track: number of fit points vs. η from simulation.

which required that tracks have more than 12 hits in order to be reconstructed. Tracks which point to the EEMC deposit charge over fewer points (padrows) due to the geometry of the TPC. Reducing the number of required hits allows more tracks to be included in the jet reconstruction, which improves our jet p_T determination. The 5 point tracking does not extend over the full TPC, and is only implemented for tracks with $\eta > 0.5$, as shown in Figs. 2.1 and 2.2.

Fig. 2.3 shows the average jet p_T ratio between the particle and detector level (see Chapter 4) as a function of the detector pseudorapitity. The red points are the results for 5 points fits, while

16
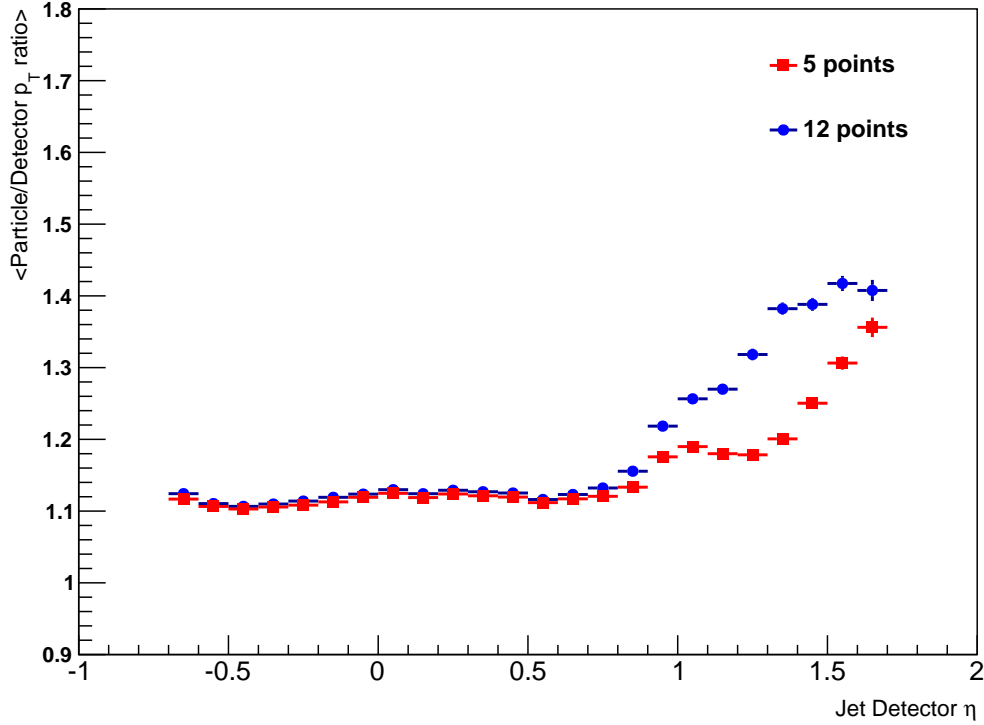
Figure 2.3: Average jet particle over detector level p_T ratio vs. detector η with different number of fit points required.

blue is for 12 points. As expected, the average value below detector pseudorapidity 0.5 is the same after implementing the 5-points threshold. Detector pseudorapidity 1.0 to 1.3 is where the tracking efficiency decreases significantly, and great improvement is found there; the difference is also reduced at higher pseudorapidity range where even 5-point tracking fails.

Tower Conditions

All calorimeter towers with $E_T \geq 0.2$ GeV and tower ADC larger than the pedestal + 4 and pedestal + RMS were included in the jet analysis.

Particles measured as TPC trajectories are assumed to be charged pions (default mass 0.1396 GeV), whereas energy deposits in the electromagnetic calorimeters are assumed to be massless photons. To avoid double-counting the jet energy contributions from the TPC and calorimeters, towers with tracks pointing to them had the $p_T c$ of the track subtracted from the E_T of the tower.

If the track $p_T c$ is greater than the energy of the tower, the tower E_T is set to zero. This method reduces the residual jet momentum corrections and sensitivity to fluctuations in the hadronic energy deposition, resulting in an improved jet momentum resolution [7]. Tracks and towers are both converted to Lorentz 4-momentum vectors and then merged as the input to the jet finder where the jet algorithm is applied. Reconstructed jets with $p_T > 5$ GeV/c were kept.

2.2   Di-Jet Selection

Di-jets are pairs of jets which arise from the same partonic hard scattering event. For each event, dijets were selected by choosing the two jets with the highest p_T that fell in the pseudorapidity range $-0.8 \leq \eta \leq 1.8$. Other conditions were the same as those used in the 2009 dijet measurements at mid-rapidity [8]. The steps used to determine which jets in an event are identified as a dijet candidate are below (in order):

1. Select the highest ranked vertex in event (vertex must have rank > 0),

2. Require vertex to have $|z| < 90$ cm,

3. Select all jets satisfying $-0.8 \leq \eta \leq 1.8$ and $-0.7 \leq \eta_{detector} \leq 1.7$,

4. Select the two highest p_T jets,

5. Require that at least one jet satisfies one of the trigger categories.

The steps above are exactly the same as those used for the 2009 Barrel-Barrel dijet measurement [8] except for the cuts on pseudorapidity, which are used for both the data and detector level simulation. When using the unbiased full Pythia sample, the $\eta_{detector}$ requirement in step 3 is omitted. The detector pseudorapidity $\eta_{detector}$ is defined by projecting the jet thrust axis from the collision vertex to the BEMC/EEMC detector, and taking the η component of the projected vector as expressed in the STAR detector coordinate.

The two jets selected using the steps above define a dijet candidate, and only one dijet candidate per event. The candidate dijets constructed using the procedure above must meet additional requirements in order to be used in the analyses. The procedures below are placed after the Underlying Event subtraction (chapter 4) and jet p_T shift (chapter 5):

- Opening angle cut: $\cos(\Delta\phi) \leq 0.5$,

- Neutral fraction cut: One jet must have a neutral fraction < 1.0,

- Asymmetric p_T cut: High p_T jet ≥ 8.0 GeV/c and low p_T jet ≥ 6.0 GeV/c,

- p_T balance cut.

The two jets arising from a partonic hard-scattering event should be roughly back-to-back in azimuth (ϕ). Jets which are closer to each other in azimuth likely do not represent the $2 \rightarrow 2$ hard scattering process. To remove these events from the analysis, an opening angle cut was placed on the two jets of the dijet event such that the azimuthal angle between them must be more than $120°$.

A p_T balance cut is used to remove the highly unbalanced p_T events that are likely a result of finite resolution in the track curvature measurement (overestimating the track p_T) and not from the hard scattering. Jets which contain a track with $p_T \geq 30$ GeV are kept if the p_T ratio of this jet over the associated one is between $\frac{2}{3}$ and $\frac{3}{2}$, otherwise the event is discarded. To facilitate comparison with theoretical predictions, an asymmetric condition (one jet had $p_T \geq 8.0$ GeV/c and the other jet had $p_T \geq 6.0$ GeV/c) was placed on the transverse momentum of the jets.

In the inclusive jet analysis, a neutral energy cut is applied to remove jets comprised primarily of background energy. The cut was usually placed such that jets with greater than 95% of their transverse momentum coming from the calorimeter towers are rejected. This kind of cut is not useful when studying jets in the EEMC, because the falling TPC efficiency means that jets in this region will have few tracks and therefore large neutral fractions. It is unlikely that a background jet will be coincident with a physics jet, so the requirement can be loosened and we only reject the dijet candidates where both jets are purely neutral, instead of putting a neutral energy cut on the jets.

Detector-level dijets were reconstructed from the simulated TPC and calorimeter responses using the same algorithms as the data (see chapter 4). We also reconstruct the jets at particle and parton level using the anti-k_T algorithm. Particle-level dijets were formed from stable, final-state particles produced in the simulated event. All stable particles are used, including those which arise from the underlying event and beam remnants. The parton-level dijets were reconstructed from the hard-scattered partons emitted in the collision, including initial and final-state radiation, but not beam remnants or underlying event effects. Because there is no detector information, the neutral fraction cut and the p_T balance cut are not used when selecting dijets at the particle and parton levels from the full unbiased Pythia sample.

In order to compare with the theory calculation, in this analysis, jets with $-0.8 < \eta < 0.8$ are considered **Barrel Jets**, while those with $0.8 < \eta < 1.8$ are **Endcap Jets**. There is no detector pseudorapidity requirement here, so it is possible that Barrel jets would have a detector pseudorapidity larger than 0.8 (Endcap region), and Endcap jets might also have a detector pseudorapidity smaller than 0.8 (Barrel region).

2.3 Di-Jet Kinematics

The leading-order kinematics of the two scattered partons can be approximated by the relativistic two-body scatterings $1 + 2 \rightarrow 3 + 4$. This leads to the kinematic relations shown in equation 2.3, assuming massless partons:

$$x_1 = \frac{p_{T,3}}{\sqrt{s}}(e^{\eta_3} + e^{\eta_4}) \tag{2.3a}$$

$$x_2 = \frac{p_{T,4}}{\sqrt{s}}(e^{-\eta_3} + e^{-\eta_4}) \tag{2.3b}$$

$$M = \sqrt{x_1 x_2 s} \tag{2.3c}$$

$$y = \frac{1}{2}\ln\left(\frac{x_1}{x_2}\right) = \frac{\eta_3 + \eta_4}{2} \tag{2.3d}$$

$$|\cos\theta| = \tanh\left(\frac{\eta_3 - \eta_4}{2}\right), \tag{2.3e}$$

where x_1 and x_2 are the momentum fractions of the colliding partons, M is the invariant mass of this interaction, y is the rapidity, and θ is the center-of-mass scattering angle. $p_{T,3}$ and $p_{T,4}$ are the outgoing partonic transverse momenta, and η_3 and η_4 are their pseudorapidities, respectively. A detailed derivation is provided in appendix B.

The (squared) true dijet invariant mass is found by taking the square of the sum of the 4-momenta of the two jets which make up the dijet:

$$M^2 = (P_3 + P_4)^2 \tag{2.4}$$

$$M = \sqrt{m_3^2 + m_4^2 + 2\sqrt{m_3^2 + p_{T3}^2}\sqrt{m_4^2 + p_{T4}^2}cosh(\Delta y) - 2p_{T3}p_{T4}cos(\Delta\phi)}. \tag{2.5}$$

The dijet kinematics show the advantage of using correlation measurements in accessing the x dependence of Δg, compared to inclusive jet measurements, which integrate over a large range in x of the initial state partons for a given transverse momentum of the final state. For example, in leading order QCD, the dijet invariant mass is proportional to the square-root of the initial state momentum fractions, $M = \sqrt{s}\sqrt{x_1 x_2}$, while the sum of the jet pseudorapidities determines their ratio $\eta_1 + \eta_2 = \ln(x_1/x_2)$. The initial partons' information is therefore embedded in the dijet observables, which would allow us to characterize the initial state more completely.

2.4   Trigger Selection

A dijet event is categorized based on the triggers satisfied by the individual jets. An individual jet can fall into one of three categories: L2JetHigh, JP1Lo, and JP1Hi. If a jet does not fall into one of these categories, it is considered untriggered. The conditions a jet must satisfy to be placed in one of these categories are listed below:

- L2JetHigh: The jet must be geometrically matched to a jet patch which fired the L0 L2JetHigh trigger with $p_T \geq 8.4$ GeV.

- JP1Lo: The jet must be geometrically matched to a jet patch which fired the L0 JP1 trigger with $p_T \leq 8.4$ GeV.

- JP1Hi: The jet must be geometrically matched to a jet patch which fired the L0 JP1 trigger with $p_T \geq 8.4$ GeV, and the L0 L2JetHigh trigger did not fire.

The jet patch geometrical matching requires that the thrust axis of a jet must be within 0.6 in $\eta - \phi$-two dimensional space of the center of the jet patch (or the E_T-weighted centroid of two adjacent jet patches for the AJP component of L2JetHigh). The p_T conditions on the jets are used to make sure no jet can be placed into more than one category.

There are eight combinations of trigger categories for dijets: L2JetHigh-L2JetHigh, L2JetHigh-JP1Lo, L2JetHigh-Untriggered, JP1Lo-JP1Lo, JP1Lo-JP1Hi, JP1Lo-Untriggered, JP1Hi-JP1Hi, and JP1Hi-Untriggered. In the following chapters, **L2 dijet** events refer to the first three trigger samples, while **JP dijet** events are the remaining five combinations.

Chapter 3

Simulation

3.1   Simulation / Embedding Details

To correct for detector effects on the measured jet quantities and study the systematic errors due to the hadronization and the detector response, simulated events generated from PYTHIA 6.425 [33] with the Perugia 0 tune [31] were chosen to run through a STAR detector response package (GSTAR) implemented in GEANT 3 [9]. The simulated events were embedded into 'zero-bias' data, which are real STAR events that were triggered on random bunch crossings over the span of the run, thus allowing the simulation sample to track accurately the same beam background, pile-up, and detector conditions as the real data set.

This simulation sample, originally produced for the 2009 pp200 inclusive jet analysis, has about 21 million events generated in ten separate partonic p_T bins. The simulation is also broken into individual runs, and then embedded into the corresponding 'zero-bias' data files. A trigger filter was used to reduce the time needed to run the simulation, by rejecting events that would not fire the JP1, AJP or BHT3 (Barrel high tower trigger) before the detector response is simulated. This filter rejected about 91% of the Pythia events. The full Pythia record for the rejected events is saved so that corrections to the unbiased sample can be made.

For the Endcap Electromagnetic Calorimeter (EEMC), we needed to incorporate the new gain

calibration results into the simulation. An afterburner method was used, to save the substantial time needed for the simulation production. More details on this method can be found in appendix C.

3.2 Levels of Jet Information

The simulation includes three distinct levels of information, corresponding to the partonic hard scattering, the final state particles from fragmentation and hadronization of the partons, and the response of the detector to those particles. These divisions will be referred to as the parton level, particle level, and detector level, respectively.

Parton Level. The parton level contains information about the hard scattered partons involved in the $2 \rightarrow 2$ hard scattering event generated by Pythia. In this level, various kinematic properties of the hard scattering, such as the center of mass energy, scattering angle, and momentum fractions of the incoming partons, are stored. When we reconstruct the jets on the parton level from the simulation, only the partons involved in the hard scattering, and partons arising from initial or final state radiation, are used in the jet finder. Partons arising from the underlying event or beam remnants are not included in the parton-level jet reconstruction.

Particle Level. The partons generated by Pythia propagate and hadronize into the stable and color-neutral particles recorded at this level. The particle level of the simulation records the kinematic information, particle id, and index of the parent parton for all of these stable particles. When we reconstruct the jets at the particle level, all stable particles are used, including those which arise from the underlying event and beam remnants.

Detector Level. The last level of the the simulation records the detector response to the stable particles from the previous level. As the particles traverse the GEANT model of the detector, they interact with the various volumes in ways consistent with how that particular particle would behave in a specific material. This interaction includes ionizing the gas in the TPC, and depositing energy in the scintillator layers of the calorimeters. This, along with a simulation of the detector readout electronics, allows the simulation to respond to particles the same way as the real detector.

When the jet finder is running on the detector level simulation, it constructs jets from the simulated response of the TPC and calorimeter towers, and their readout electronics.

3.3 Data - Simulation Comparison
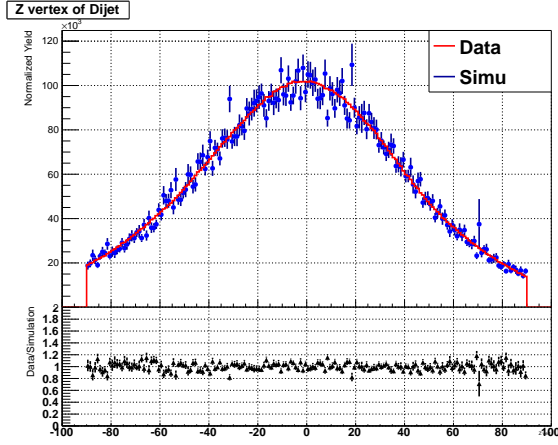
Figure 3.1: Z vertex distribution for L2All.
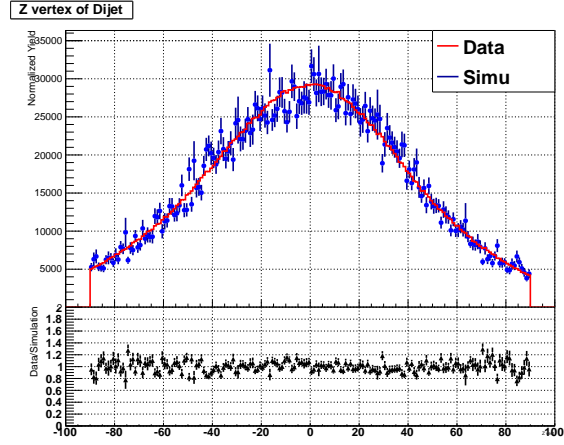
Figure 3.2: Z vertex distribution for JPAll.

The simulated events are generated with some distribution of z-vertex positions, which may not exactly match the z-vertex distribution of the data. In order to achieve the best matching between the data and simulation, the z-vertex distribution of the simulation should be altered to match that of the data. This is done by re-weighting the simulation events. The re-weighting is done by taking the ratio of the z-vertex distribution observed in the data to that of the simulation. This ratio is then fit with a 4th-order polynomial. Each simulation event is thus associated with a re-weighting factor from the 4th-order polynomial functions. Figs. 3.1 and 3.2 show the z-vertex distributions from data and simulation after the z-vertex re-weighting has been applied for two trigger combinations.

Detector-level dijets were reconstructed from the simulated TPC and calorimeter responses using the same jet-finding algorithms as the data. Comparison of the dijets reconstructed from data and simulation confirms that the STAR detector response is well understood. The dijet invariant mass distribution is shown in Figs. 3.3 and 3.4 for L2 and JP triggers, respectively, and in Figs. 3.5 and 3.6 the (higher) jet p_T spectra are presented. Figs. 3.7, 3.8, 3.9 and 3.10 show good geometric
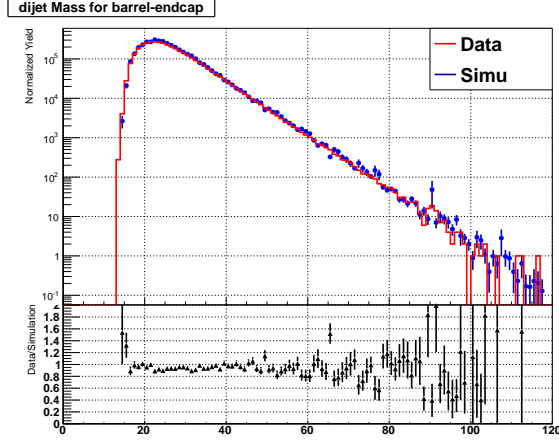
Figure 3.3: Di-jet invariant mass L2All.
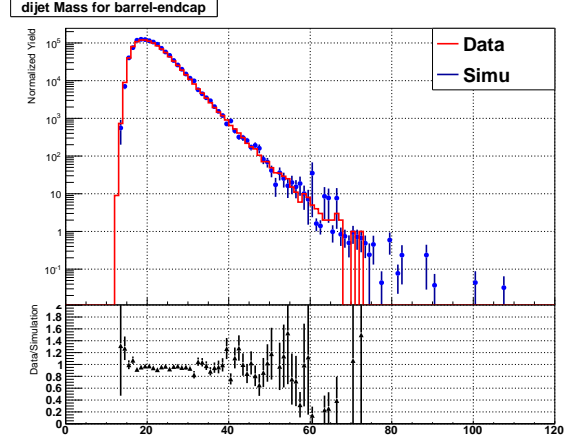
Figure 3.4: Di-jet invariant mass JPAll.
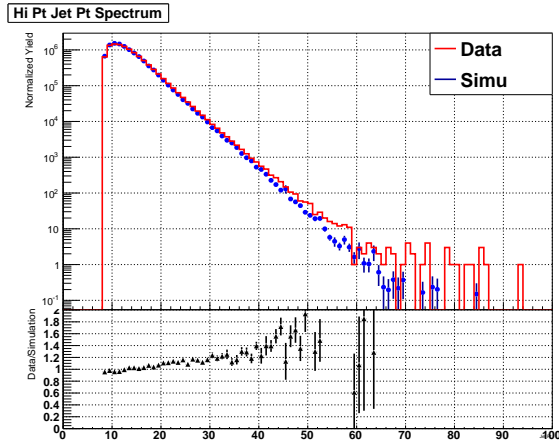
Figure 3.5: Hi p_T jet p_T L2All.
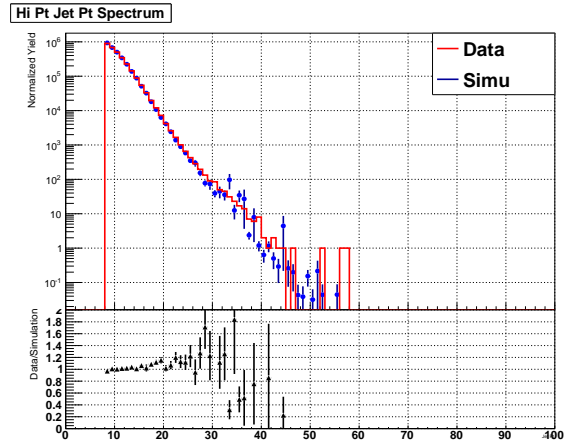
Figure 3.6: Hi p_T jet p_T JPAll.

matching, which means that the detector conditions are simulated very well, as the ϕ spectrum is particularly sensitive to the TPC hardware and its failures. Figs. 3.11 and 3.12 show the jet neutral energy fraction comparisons, also in good agreement, even into the endcap region where the tracking becomes inefficient. In Fig. 3.13 we show the integrated transverse energy profiles within the BEMC and EEMC jets. The shapes of the data distributions are reproduced sufficiently well. Taken together, this means that the detector response and event triggering are well simulated at STAR.

3.3.1 Jet Association

Dijets were also reconstructed in simulation at the particle and parton levels. After we find the detector level dijet, the particle and parton level dijet were associated via the geometric matching condition that $\Delta R = \sqrt{(\eta_{Det} - \eta_{Par})^2 + (\phi_{Det} - \phi_{Par})^2} < 0.5$ for each of the two jets.

A matching condition that requires the particle/parton level z-vertex and detector level z-vertex to be within two centimeters of each other is also imposed to improve the matching. The vertex associated with the particle/parton level is the one which is set when Pythia is run, whereas at the detector level, the vertex is found by emulating the vertex finder which is run on the actual data. The latter may be affected by the 'zero-bias' event, resulting in a different vertex position.
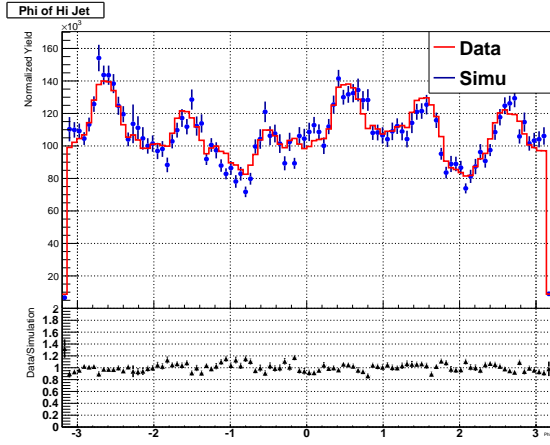
Figure 3.7: Hi p_T jet ϕ L2All.
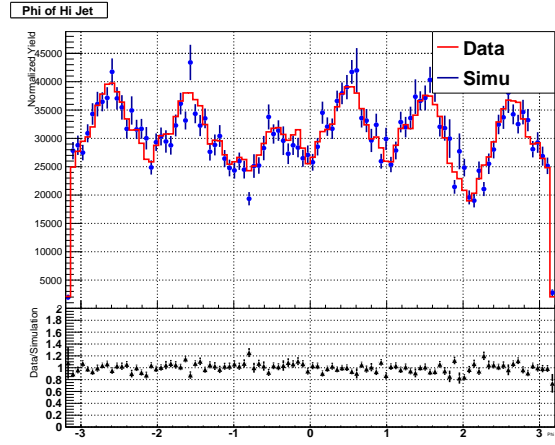
Figure 3.8: Hi p_T jet ϕ JPAll.
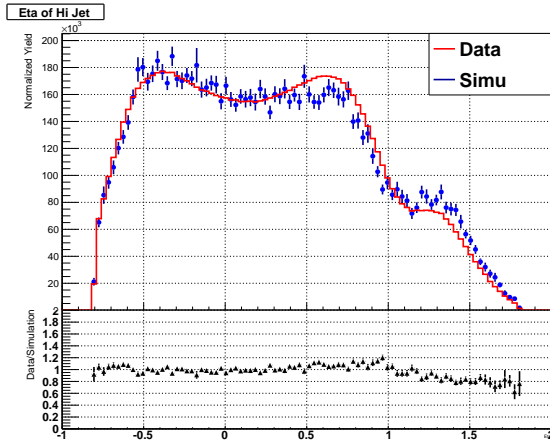
Figure 3.9: Hi p_T jet η L2All.
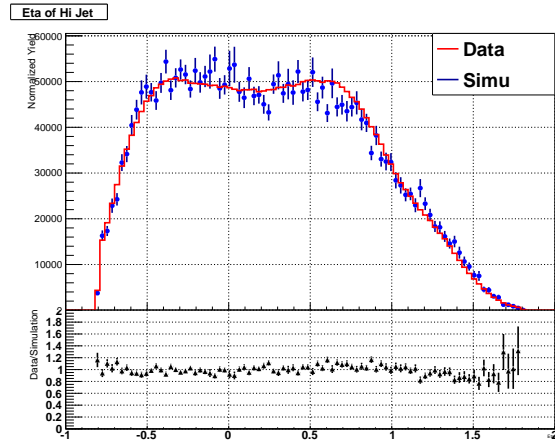
Figure 3.10: Hi p_T jet η JPAll.
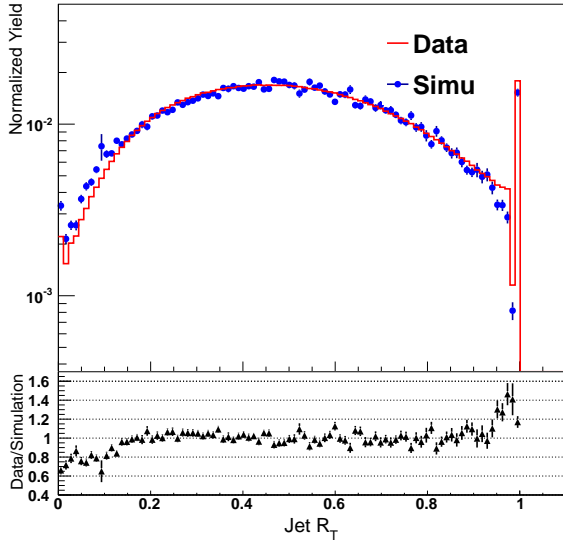
Figure 3.11: Barrel jet R_T L2All.
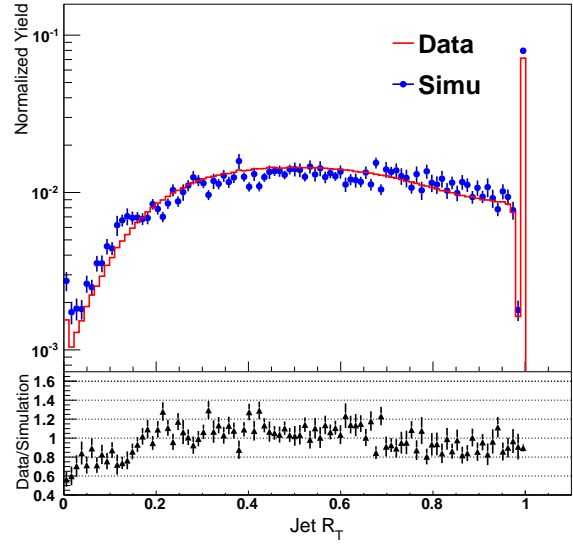
Figure 3.12: Endcap jet R_T L2All.

Tue Jun 20 11:36:06 2017
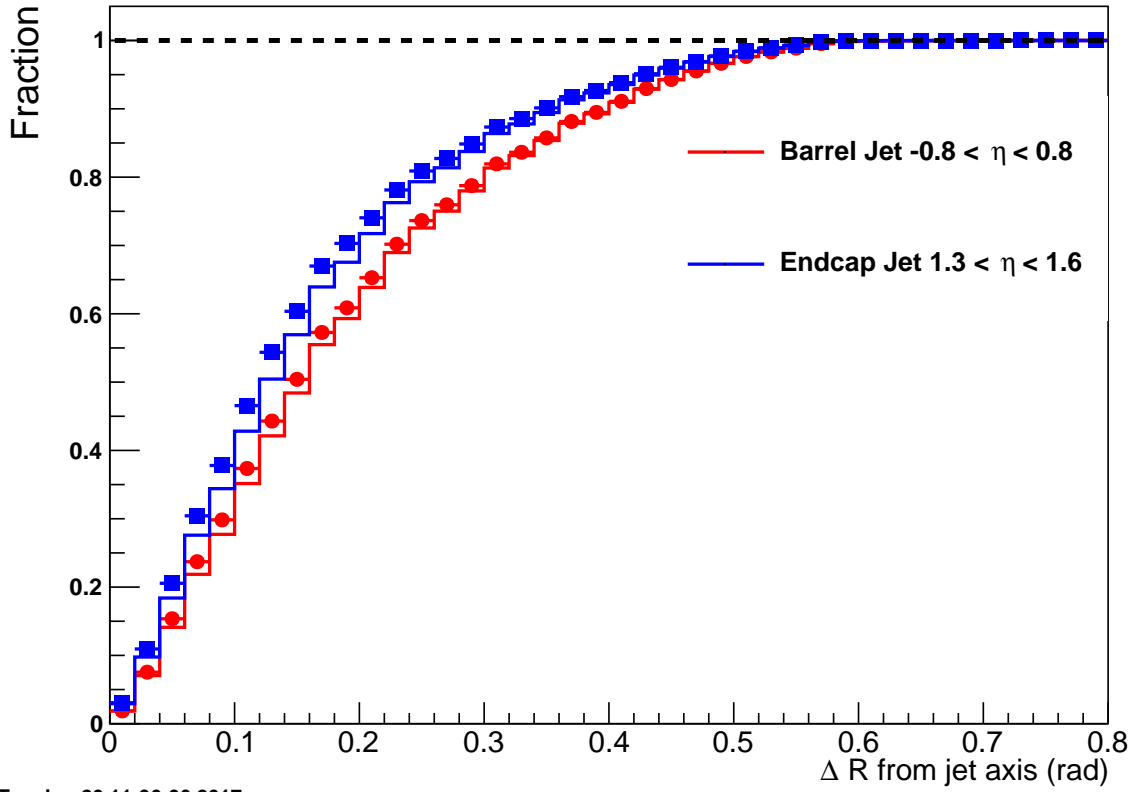
Figure 3.13: Fraction of the total jet transverse energy found within a cone of radius ΔR centered on the reconstructed thrust axis, illustrating the jet profile.

3.4   'Fudge Factor' Reweighting of the p_T Bins

3.4.1   Weight and Fudge Factor Issues

In order to obtain sufficient statistics at high jet p_T, where the jet cross section falls off exponentially, the simulation was subdivided into 10 bins of partonic $\hat{p}_T$: 2 to 3, 3 to 4, 4 to 5, 5 to 7, 7 to 9, 9 to 11, 11 to 15, 15 to 25, 25 to 35, and 35 to infinity, all in GeV/c. To make a smooth spectrum, the events from each partonic $\hat{p}_T$ bin needs to be weighted by a factor of (σ/N_{events}), where σ is the cross section for that partonic $\hat{p}_T$ bin, while N_{events} is the number of generated events from that bin. The weighted distribution is shown in Fig. 3.14.
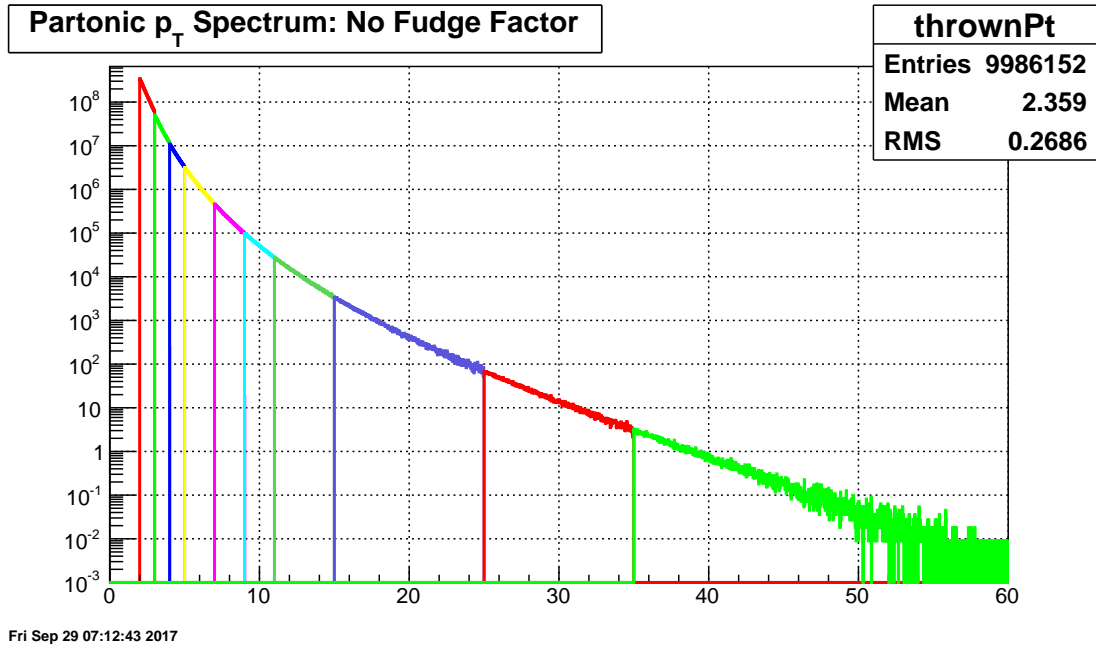
Figure 3.14: Pythia partonic p_T distribution: without fudge factors.

As can be seen in the figure, it was noticed that 'fudge factors' were needed to match the distributions between different bins, especially in the low p_T range where Pythia may get the relative cross section wrong. Fudge factors are necessary in order to compensate for the wrong normalization of Pythia yields, due to its incomplete ability to treat the multiple interactions (MI) contribution to QCD processes. A detailed description can be found in the Pythia manual [33], page 348.

The fudge factors were determined by fitting $e^{A+Bx+Cx^2}$ to each partonic $\hat{p}_T$ bin, and then taking the ratio of those functions at the bin edges. In Figs. 3.15 and 3.16 we show the four lowest p_T bins before and after the fudge factors are applied. It is obvious that this correction makes the distributions between different bins look better. The final values used are listed in Table 3.1
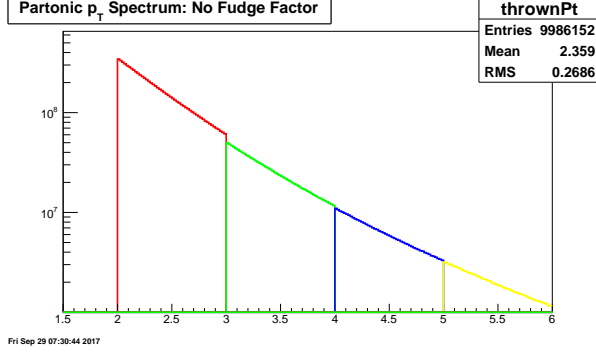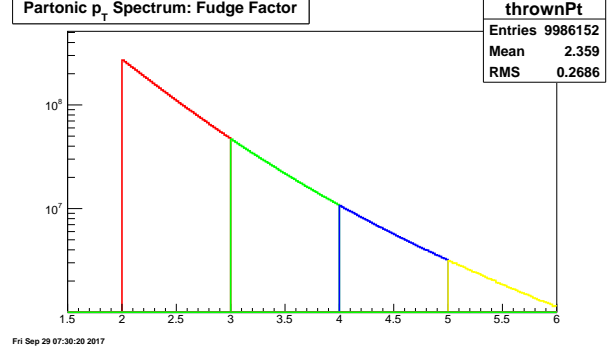
Figure 3.15: Pythia partonic p_T distribution: without fudge factors.

Figure 3.16: Pythia partonic p_T distribution: with fudge factors.

Partonic $\hat{p}_T$	Final Weight	Raw Weight	PYTHIA Events	$\sigma(mb)$	Fudge factor
2-3	70777.2	90056.2	9.98615e+06	8.10515	0.785922
3-4	24328.6	26098.3	5.50909e+06	1.29581	0.932191
4-5	9912.36	10207.8	3.41895e+06	0.314538	0.97106
5-7	9416.2	9529.65	1.58767e+06	0.136360	0.988095
7-9	2027.59	2027.59	1.25672e+06	0.0229651	1.0
9-11	739.407	739.407	827150	0.00551210	1.0
11-15	590.057	590.057	419029	0.00222837	1.0
15-25	145.624	145.624	297222	0.000390089	1.0
25-35	5.67755	5.67755	199332	0.0000101997	1.0
35-∞	1.0	1.00000	59541	0.000000536618	1.0

Table 3.1: Pythia jet embedding weight factors.

3.4.2 Fudge Factor Reweighting

In Pythia, the default for hadron-hadron collisions is to include QCD jet production by $2 \rightarrow 2$ processes. During this process a lower cut-off has to be introduced, as the differential cross section is divergent for $\hat{p}_\perp \rightarrow 0$. However, if we choose the Pythia simulation to run only for $\hat{p}_\perp > 1.25$ GeV, we disable the interpolation of low p_T cross section behavior. More details on this issue are

available in the Pythia manual, section 8.9.3.

If we generate the Pythia simulation events in one bin ($\hat{p}_\perp = 0$ to ∞), instead of the 10 separated bins, the behavior looks quite different at low partonic values, as can be seen in Fig. 3.17.
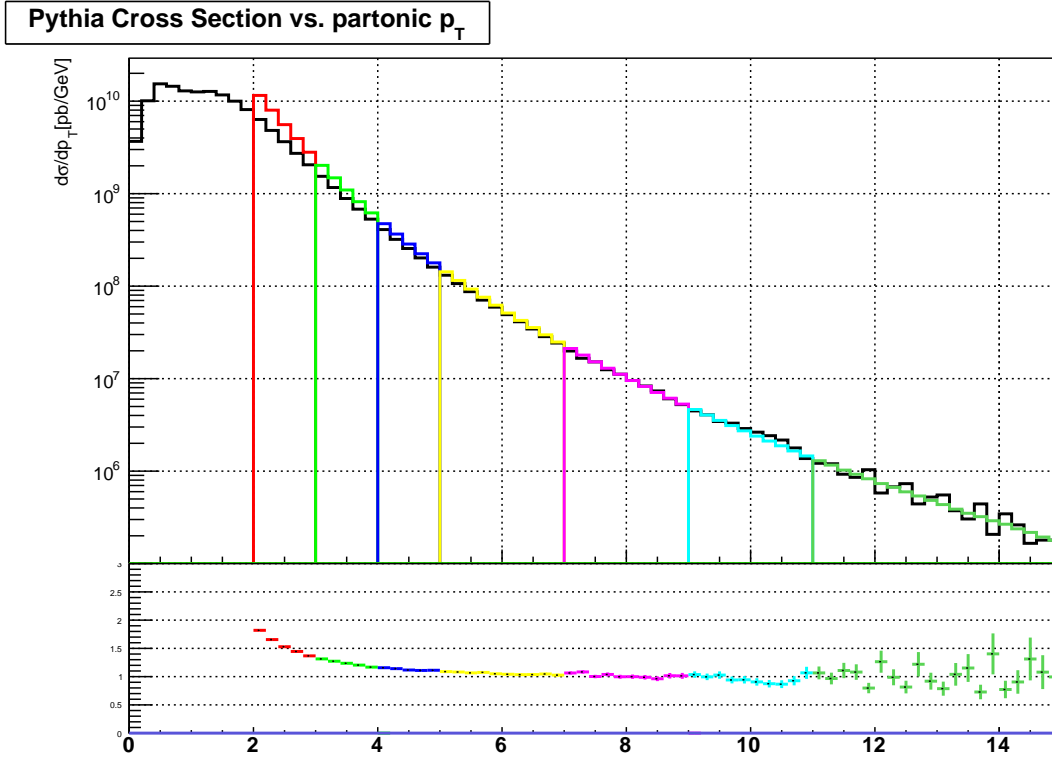
Figure 3.17: Pythia partonic p_T distributions: the black line is generated using the bin range from 0 to ∞; the other colors are from separate bins.

To compensate for this effect, a fudge factor reweighting was calculated by estimating the ratio of the cross section from the integrated bins (0 to ∞) to separated bins, as a function of the partonic $\hat{p}_T$ values. We then fit this curve with the function $w = \frac{1}{1+(p_0+p_1(x-2)+p_2(x-2)^2)e^{p_3(x-2)}}$, as shown in Fig. 3.18.

In Fig. 3.19 and 3.20 we show the jet p_T and dijet invariant mass spectra, respectively, after we applied the fudge factor reweighting (value extracted from the fitting function w). There is only about a 2% yield change to the simulation, so the overall effect is very small and was neglected.

χ^2 / ndf	51.18 / 56
p0	0.9201 ± 0.0047
p1	-0.147 ± 0.034
p2	0.1684 ± 0.0234
p3	-1.02 ± 0.06

Fri Sep 29 08:26:31 2017
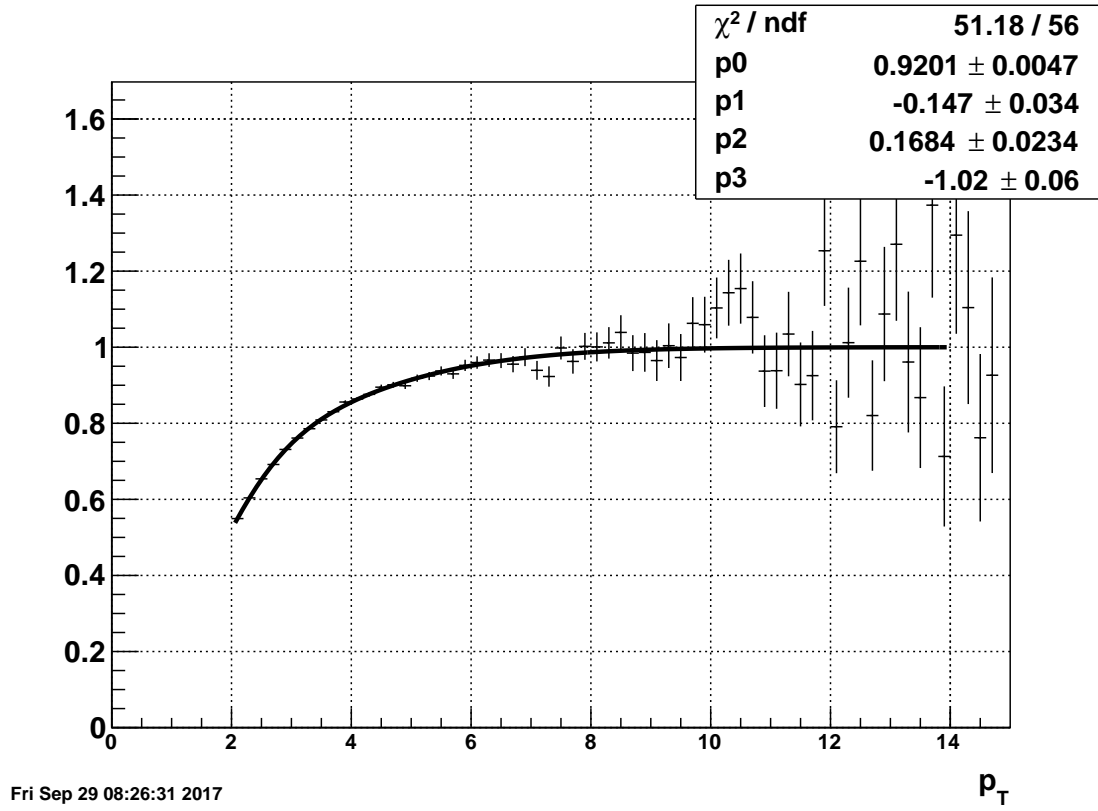
Figure 3.18: Pythia partonic p_T cross section ratio: integrated bins over the separate bins.
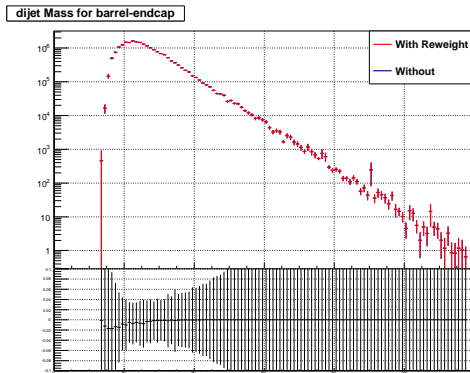
Figure 3.19: Simulation: dijet invariant mass distribution with and without reweighting.
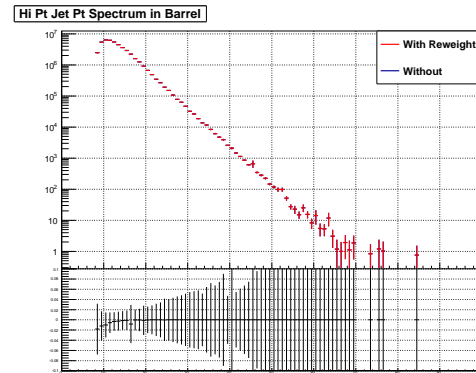
Figure 3.20: Simulation: jet p_T distribution with and without reweighting.

Chapter 4

Underlying Events

The hard parton-parton interactions in proton-proton collisions are often accompanied by other processes which collectively contribute additional particles to those from the hard scattering. In hadron-hadron scatterings, the underlying event (UE) is defined, in the presence of a hard parton-parton scattering with large transverse momentum transfer, as any hadronic activity beyond what can be attributed to the hadronization of partons involved in the hard scattering, and to related initial and final state QCD radiation. It is the sum of all the processes that build up the final hadronic state in a collision, excluding the hardest leading-order partonic interaction. The UE activity is thus attributed to the hadronization of partonic constituents that have undergone multiple parton interactions (MPI), as well as to beam-beam remnants, concentrated along the beam direction. We note that UE contributions are distinct from "pile-up" processes, including other p-p collisions that just happen to be close in time to the scattering of interest.

Events with hard jets are often accompanied by a more diffuse 'background' of relatively soft particles. In proton-proton collisions, the hardest parton scattering process is what we are interested in; but the other soft scatterings could be mixed into the hardest scattering and contribute to the signals that are finally measured. The background generated due to these multiple soft scatterings is classified as underlying events contributions. This background is different from detector pileup, because these collisions are coming from the same proton-proton collision as the hardest scattering.

4.1 Off-Axis Cone Method

For many physics applications, it is useful to estimate the characteristics of the background on an event-by-event basis, and then correct the hard jets for the soft contamination. The off-axis cone method is a method to study underlying events on the level of jet-by-jet, instead of on the level of an event. This method was developed by Zilong Chang for the STAR 2012 at 500 GeV inclusive jet analysis, which was adapted from the perpendicular cones method used in the ALICE experiment [2].

In this method, we draw two off-axis cones for each reconstructed jet, each of which is centered at the same η as the jet, but $90°$ away in ϕ from the jet ϕ, as shown in Fig. 4.1. We then collect particles falling inside the two cones. The particle candidate pool is the exact same input as is used for the jet finding algorithm. The off-axis cone radius was chosen to be the same as the jet parameter of the anti-k_T algorithm used in this analysis, R = 0.6. The p_T of the off-axis cone is defined as the scalar sum of all the particles inside the cone, denoted as $p_{T,ue}$ and the mass of the off-axis cone is the invariant mass of the vector sum of all the particles inside the cone. The energy density, $\rho_{ue,cone}$, is defined as the off-axis cone p_T divided by the cone area (πR^2) and the mass density, $\rho_{m,ue,cone}$, is the off-axis cone mass divided by the cone area. The multiplicity of the off-axis cone is the number of particles inside the cone. Finally the average density of the two cones is taken as the estimate to the underlying event density, $\rho_{ue} = \frac{1}{2}(\rho_{ue,1} + \rho_{ue,2})$.

Given that the physics of the underlying event is expected to be evenly distributed over $\eta - \phi$ space, the calculated underlying event energy density should be approximately uniform in $\eta - \phi$ space. However, detector acceptances and efficiencies are usually not uniform in $\eta - \phi$ space. For example, at STAR there is a gap between the BEMC and EEMC, and the TPC tracking efficiency degrades drastically over $1.0 < |\eta| < 1.5$. Fortunately the STAR detector has good symmetry in ϕ, and the two off-axis cones are centered at the same η as the jet, therefore it should be very applicable here.
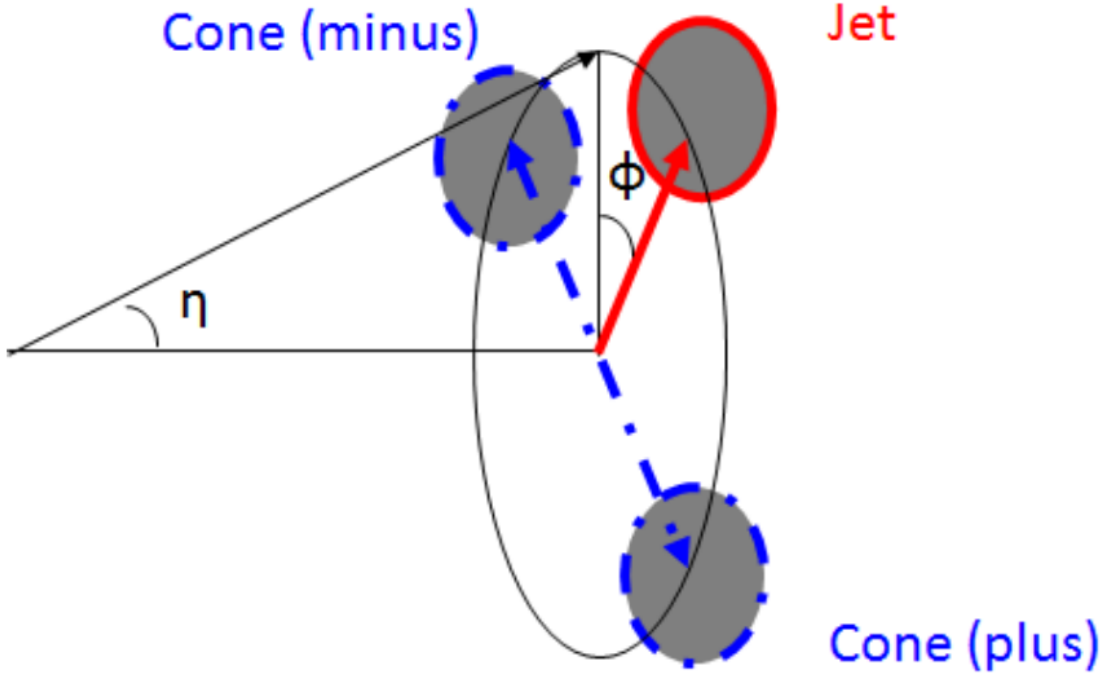
Figure 4.1: Geometry of the off-axis cone method.

4.2 Underlying Event Correction

Dijet measurements are sensitive to the jet's direction, and more generally to the jet's full 4-momentum (for example, for large jet radii, the contamination from the background can build up a significant invariant mass). For each jet in a dijet event, the underlying event 4-vector correction is calculated according to:

$$P_\mu^{corrected} = P_\mu - [\rho A_{jet}^x, \rho A_{jet}^y, (\rho + \rho_m) A_{jet}^z, (\rho + \rho_m) A_{jet}^E], \tag{4.1}$$

where P_μ is the jet's uncorrected 4-vector, ρ is the underlying event transverse momentum density and ρ_m is the underlying event mass density as determined using the Off-Axis cone method, and A_μ is the 4-vector area calculated in the fast-jet package [17] using the ghost particle technique [14].

The inclusive jet's main observable is the jet transverse momentum p_T. The correction method used is $p_T^{corrected} = p_T - \rho \times A_{jet}$, where A_{jet} is the jet scalar area. Fig. 4.2 shows the comparison

of the jet p_T spectrum after the underlying event subtraction, using the two subtraction methods presented before. They are almost identical, as expected.

When performing this jet 4-vector momentum subtraction, two other requirements were imposed here to avoid over-corrections due to local fluctuations in the underlying event density:

1. If the jet area $\times \rho_{ue} >$ jet p_T, the corrected jet's 4-vector is set to be a vector with zero transverse momentum, zero mass, and the pseudorapidity and azimuth of the original unsubtracted jet.

2. If the squared jet mass is negative (imaginary jet mass), we replace the corrected jet 4-momentum with the same transverse components, zero mass, and the pseudorapidity of the original unsubtracted jet.
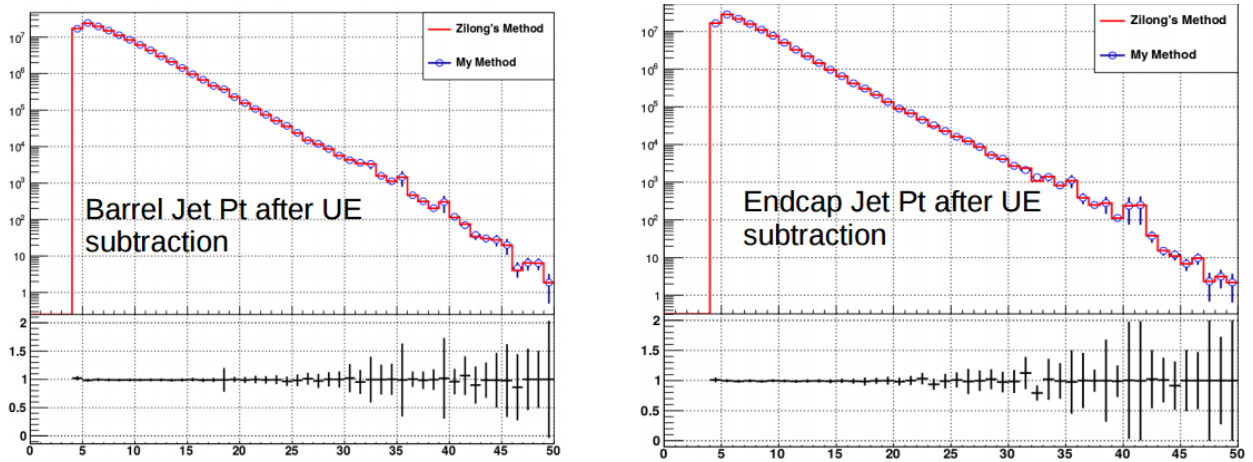
Figure 4.2: Jet P_T comparision after underlying event subtraction.

In Figs. 4.3, 4.4, and 4.5 we show the jet p_T, mass, and dijet invariant mass before and after making the underlying event subtraction. Overall, the spectra are shifted slightly toward lower values, as expected. We also note that the underlying event affects the jet invariant mass more significantly than either the transverse momentum or the dijet mass.

In the analysis that follows, the detector level and particle level jets used are those after the underlying event correction. More details about the 4-vector subtraction can be found in the fast-jet group's publications [17].
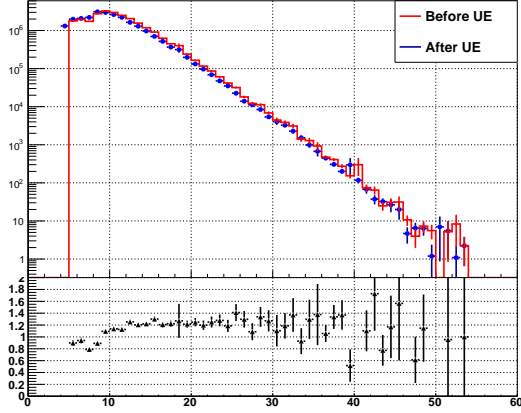
Figure 4.3: Jet p_T before and after underlying event subtraction.
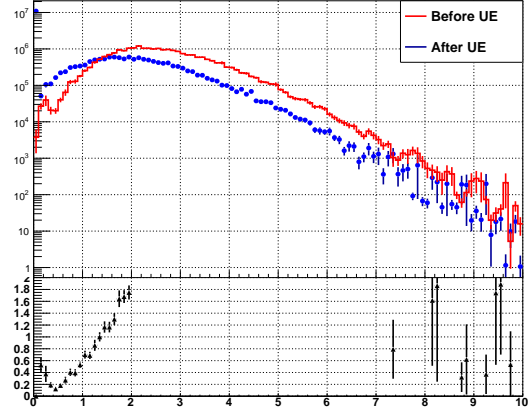
Figure 4.4: Jet mass before and after underlying event subtraction.
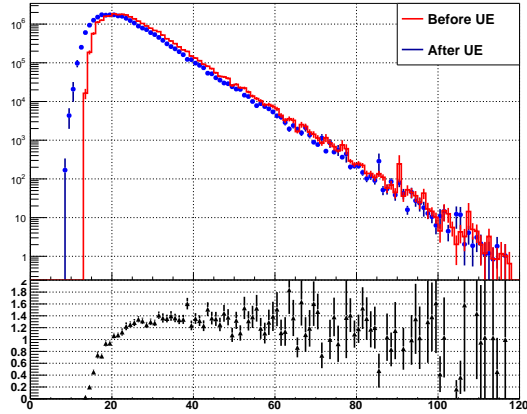
Figure 4.5: Di-jet mass before and after underlying event subtraction.

Chapter 5

Experimental methods

5.1 Challenges in the Forward (EEMC) Region

As noted before, the STAR TPC only covers the nominal range $|\eta| \leq 1.3$; the tracking efficiency decreases rapidly in more forward regions, where the Endcap Electromagnetic Calorimeter (EEMC) is located. Lower tracking efficiency means the reconstructed jets will have lower p_T on average, as will be shown later. This inaccurate p_T reconstruction skews the extraction of the initial state parton momenta. Jets with a high percentage of neutral energy are preferentially selected, both in triggering and reconstruction, leading to a biased sample.

The jet invariant mass is also skewed during the jet reconstruction. In the jet-finder algorithm (chapter 2), tracks are assigned the mass of charged pions, while for the electromagnetic calorimeter towers the particles are assumed to be massless, which makes the detector-level jet invariant mass deviate from its true value. The limited tracking capabilities in forward region also makes the particle identification not possible for these di-jet measurements. The reconstructed jet parameters need to be corrected in order to have the right energy, direction, and neutral fraction. This is of crucial importance in these dijet measurements.

5.2 Machine Learning Approaches

A machine-learning regression method was used to make the corrections for the jet measurements. Machine learning methods have been a hot topic in recent years, and there are plenty of essential problems in High Energy Physics that can be solved using Machine Learning methods. These vary from online data filtering and reconstruction to offline data analysis. Such supervised machine-learning regression algorithms make use of training events, for which the desired output is known, to determine an approximation of the underlying functional behavior defining the target value. This method is extremely helpful in making the corrections in this work.

Multilayer Perceptron (MLP from TMVA [22]) is the main algorithm applied in this analysis, with the parameters tuned properly. However, slightly changing the parameters, such as the number of layers and nodes, in the Multilayer Perceptron may impact the learning process. Different algorithms may emphasize slightly different behaviors, which would also have some influence. The systematic errors of this method are evaluated and added in quadrature from the outputs using different training sample sizes, changing the number of layers and nodes, and from using the Linear Discriminant algorithm (LD from TMVA) and K-Nearest Neighbors (KNN from TMVA) as alternate methods.

5.2.1 Artificial Neural Networks

An Artificial Neural Network (ANN) is a simulated collection of interconnected neurons, with each neuron producing a certain response to a given set of input signals. The network is put into a defined state that can be measured from the response of one or several (output) neurons after applying an external signal to the input neurons, or one can just simply view it as the mapping from the input space to multi-dimensional output space, which can be nonlinear if the response is nonlinear. The behavior of the neural network is determined by the layout of the neurons, the weights of the connections, and the response of the neurons to the input signals.

The multilayer perceptron method reduces the complexity of the mapping connections by

organising the neurons in layers, and only allowing direct connections from a given layer to the following layer, as suggested in Fig. 5.1. The first layer of a multilayer perceptron is the input layer that holds the input values (x_i), while the last is the output layer that holds the output variable (y_{ANN}, the neural net estimator). All others are hidden layers with hidden neurons (y_i^n). A weight (w_{ij}^l) is associated with each directional connection between the neutrons, and the output values of all the connected neurons are multiplied with the weights when calculating the input value to the response of the given neuron.
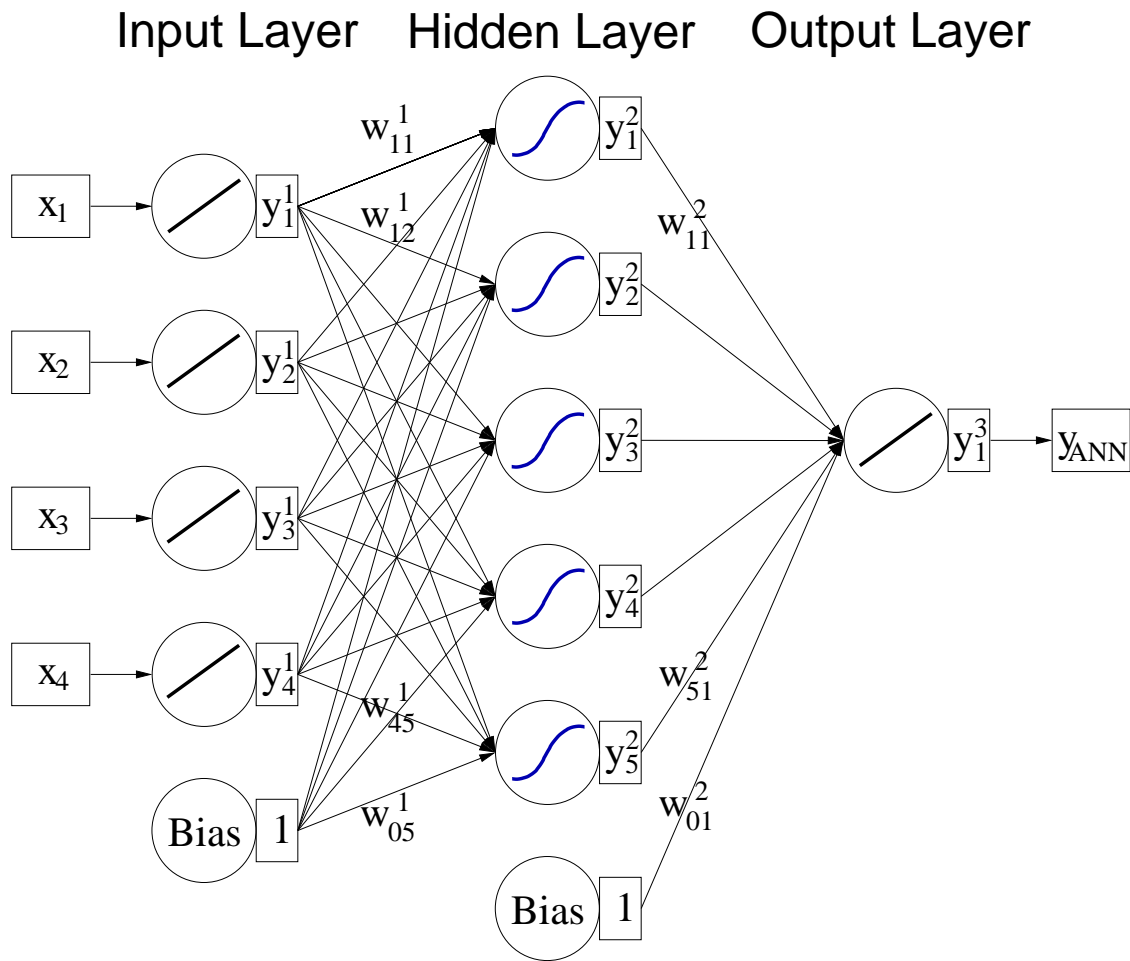
Figure 5.1: Multilayer perceptron with one hidden layer, from Ref. [22].

5.2.2 Other Machine Learning Methods

Linear Discriminant (LD)

The linear discriminant (LD) analysis is a method used to find the linear combination of features that characterize the events. The 'linear' feature refers to the discriminant function $y(x)$ being linear in the parameters β:

$$y(x) = x^\top \beta + \beta_0 \tag{5.1}$$

In regression problems, the discriminant function $y(x)$ is the best estimate for the data obtained by a least-squares regression.

k-Nearest Neighbors (k-NN)

The k-nearest neighbors algorithm (k-NN) is a non-parametric method that compares an observed event to reference events from a training data set. The input consists of the k closest training examples in the feature space, which are then used by the algorithm to find the neighbours. Each training event contains a regression value and the output is the weighted average of its k nearest neighbors' regression values. We did not use this method in our analysis, except to estimate systematic uncertainties.

5.3 Jet p_T Corrections

5.3.1 Variable Selection

For the jet p_T correction, the target value used in training is the jet's true p_T (particle level). The choice of inputs is important in machine learning approaches. Jet transverse momentum p_T and detector pseudorapidity $\eta_{detector}$ are the key input variables, because they are directly related to the failing tracking efficiency in the EEMC region. In Fig. 5.2, upper left plot, is the jet particle level over the detector level p_T ratio before the correction; if we only use these two variables (detector

p_T and $\eta_{detector}$) to train the network, the upper right plot is the jet particle level over the detector level after correction. We found that the output looks good after the regression method.
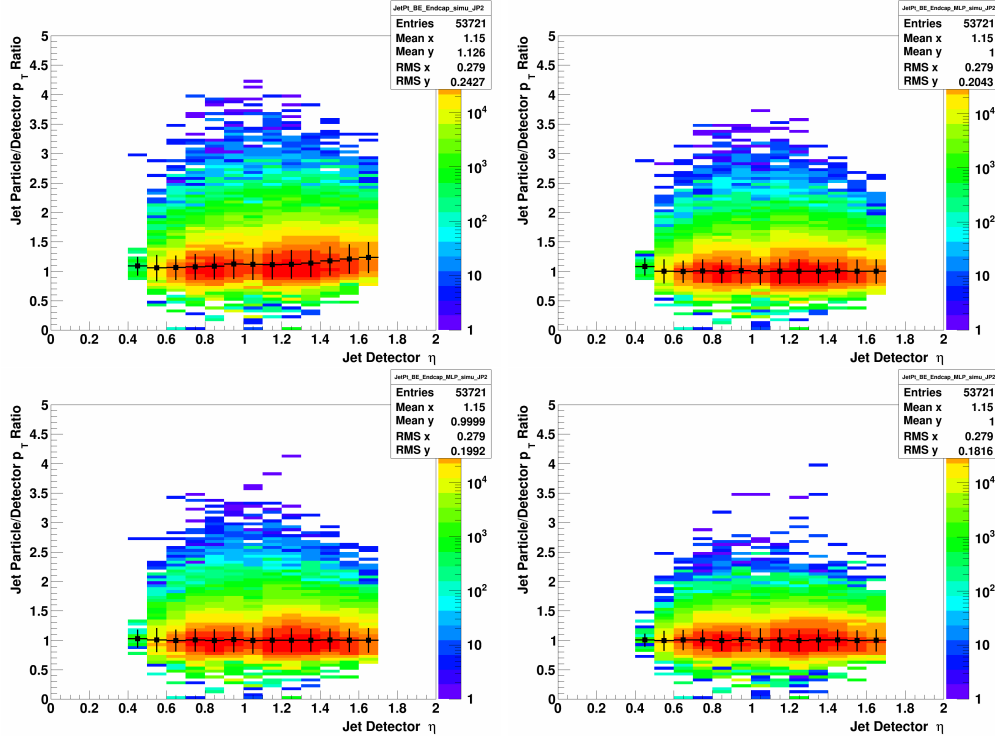
Figure 5.2: p_T shift: JP2 Endcap jet particle/detector p_T ratio vs. detector η; upper left: before shift; upper right - variable: $p_T, \eta_{detector}$; lower left: add R_t; lower right: add R_t and p_T^{Barrel}.

The jet neutral energy fraction R_t determines the relative energy of the charged and neutral particles inside the jet, and might help the regression learning process. As shown in Fig. 5.2 lower left plot, adding R_t as an additional variable improves the resolution by about $\sim 3\%$.

A di-jet is a correlation observable, and the energy of the jet in the Barrel Electromagnetic Calorimeter (BEMC) was measured much more precisely than the corresponding jet in the Endcap Electromagnetic Calorimeter (EEMC) due to the much higher efficiency of the TPC in the BEMC region. Adding the corresponding Barrel Jet p_T as another variable would also benefit the learning process for the Endcap jet for Barrel-Endcap di-jet topologies. Including this variable improves the resolution about 9%, as shown in the Fig. 5.2 lower right plot.

5.3.2 Corrections to the Jet Transverse Momentum

Jet p_T corrections are made for both the Barrel jet and Endcap jet. The Barrel jet's transverse momentum is more precisely measured than the Endcap jet, but it is still systematically lower than its true value due to the limits on detector resolution, such as the tracking efficiency limit (85% at $|\eta| \leq 1.0$) and the EMC tower size. For the Barrel Jet p_T correction, methods and variables were chosen as below:

- Methods: Multilayer Perceptron (MLP).

- Input Variables: jet detector level p_T, detector pseudorapidity $\eta_{detector}$, neutral fraction R_t.

- Target: particle level jet p_T.

As has been discussed in chapter 2, di-jet events have several different trigger combinations. As we only require at least one of the jets to be triggered, then the individual jets may fire a JP2, JP1 trigger or be untriggered (UnJP, not fire JP2 or JP1). Jets with different triggers may have slightly different characteristics, and to utilize this trigger separation, jets from the di-jet events are trained separately for each trigger. In Fig. 5.3 the ratio of Barrel jet particle level p_T over the uncorrected value for the different triggers is shown, while in Fig. 5.4 the ratio after the p_T correction is plotted. After we made the correction, the difference between the measured quantity and its true value is reduced, and the overall resolution is also improved.

For the Endcap Jet p_T, methods and variables were chosen as below (the Barrel jet transverse momentum p_T is used as input only for the Barrel-Endcap di-jet topology; it is not applicable for the Endcap-Endcap topology).

- Method: Multilayer Perceptron (MLP).

- Variables: Endcap jet detector level p_T, detector pseudorapidity $\eta_{detector}$, neutral fraction R_t; Barrel jet detector level p_T.

- Target: particle level jet p_T.
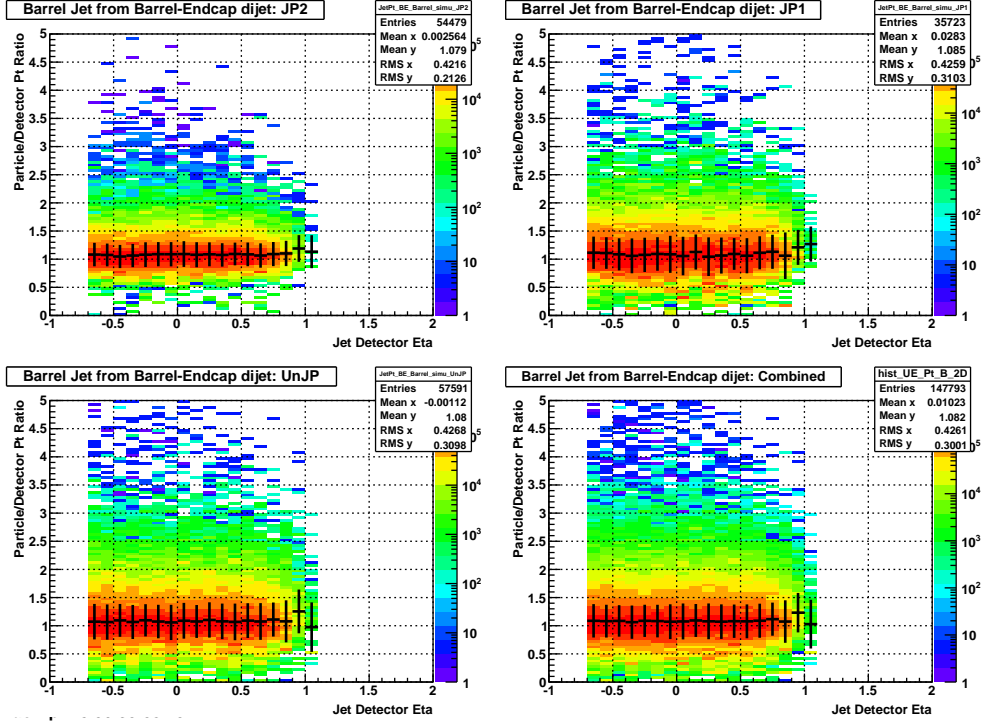
Figure 5.3: p_T shift: Barrel jet particle/detector p_T ratio vs. detector η for different triggers.

The Endcap jet JP2, JP1 and UnJP samples are also trained and tested separately. Fig. 5.5 shows the ratio of the Endcap jet particle level p_T over the uncorrected value before the p_T correction. In these figures, the effect of the falling tracking efficiency is directly indicated by the increase of the average ratio at forward pseudorapidity. For the JP2 trigger, this effect is not as significant as for others, because the JP2 trigger has a higher energy threshold, indicates that the trigger separation in training is a good choice. Fig. 5.6 is the same ratio after the p_T correction. The detector pseudorapidity dependence of the jet p_T decrease is corrected, and the overall difference is reduced due to better p_T resolution.

Figure 5.4: p_T shift: Barrel jet particle/output from the machine learning p_T ratio vs. detector η for different triggers.

Figure 5.5: p_T shift: Endcap jet particle/detector p_T ratio vs. detector η for different triggers.

Figure 5.6: p_T shift: Endcap jet particle/output from the machine learning p_T ratio vs. detector η for different triggers.

5.4 Regression Performance Evaluation

Ranking for regression is based on the correlation strength between the input variables (or MVA method response) and the regression target. Several correlation measurements are implemented in TMVA to capture and quantify the nonlinear dependencies. Their results are printed to standard output.

5.4.1 Variable Correlation

The correlation between two random variables X and Y is usually measured with the correlation coefficient $\rho = \frac{\text{cov(X,Y)}}{\sigma_X \sigma_Y}$. This coefficient is symmetric and lies in $[-1, 1]$, which quantifies by definition a linear relationship. If $\rho = 0$, then X and Y are independent variables, but higher order functional or non-functional relationships may not, or only marginally, be reflected in the value of ρ. The correlations among the four variables used in the Endcap jet p_T correction are shown in Fig. 5.7. The Endcap jet p_T and Barrel jet p_T are positively correlated, as they are from the same di-jet events; the Endcap jet p_T is negatively correlated with its neutral fraction and detector pseudorapidity, in agreement with our expection. We would be more likely to underestimate the jet's p_T due to the falling tracking efficiency in the Endcap region, and the jets we measured there are likely to have higher neutral energies.

5.4.2 Overtraining

Overtraining occurs when a machine learning problem has too few degrees of freedom, because too many model parameters of an algorithm were adjusted to fit too few data points. The sensitivity to overtraining therefore depends on the MVA method. For example, a linear discriminant (LD) can hardly ever be overtrained, whereas without the appropriate counter measures, boosted decision trees usually suffer from at least partial overtraining, owing to their large number of nodes. Overtraining leads to a seeming increase in the classification or regression performance over the objectively achievable one if measured on the training sample, and to an effective performance

47
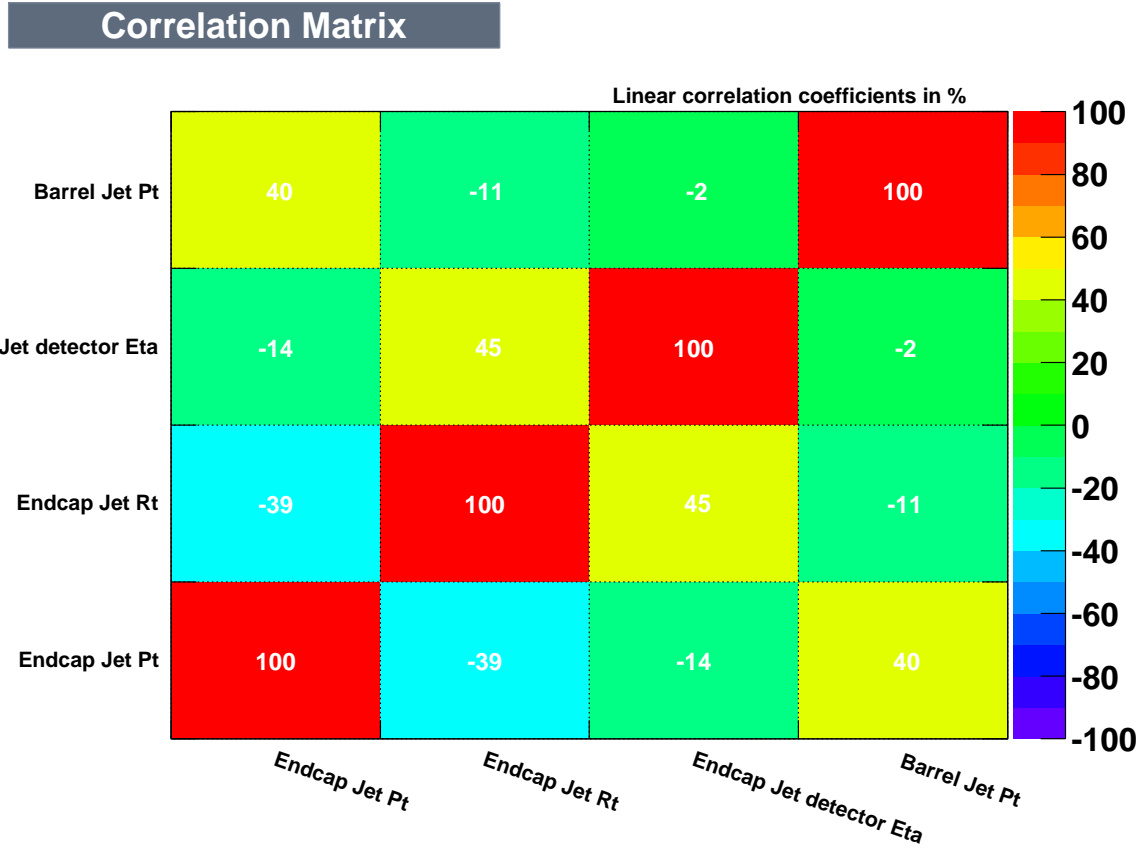
Figure 5.7: Correlation between different variables for Endcap jet p_T corrections.

decrease when measured with an independent test sample. A convenient way to detect overtraining and to measure its impact is therefore to compare the performance results between training and test samples. Such a test is performed by TMVA with the results printed to standard output.

There are various method-specific solutions to counteract overtraining. It is typically not known beforehand how many epochs (the number of iterations through the entire data set used to train the network) are necessary in order to achieve a sufficiently good training of the neural network. The neural networks steadily monitor the convergence of the error estimator between training and test samples, suspending the training when the test sample has passed its minimum. The convergence test for MLP is shown in Fig. 5.8. The agreement seen between the training and testing samples means that the MLP method is well suited for this problem.

Fig. 5.9 shows the average quadratic deviation of the learning output from its true values for three different machine learning methods. In each case, we find good agreement between the

MLP Convergence Test
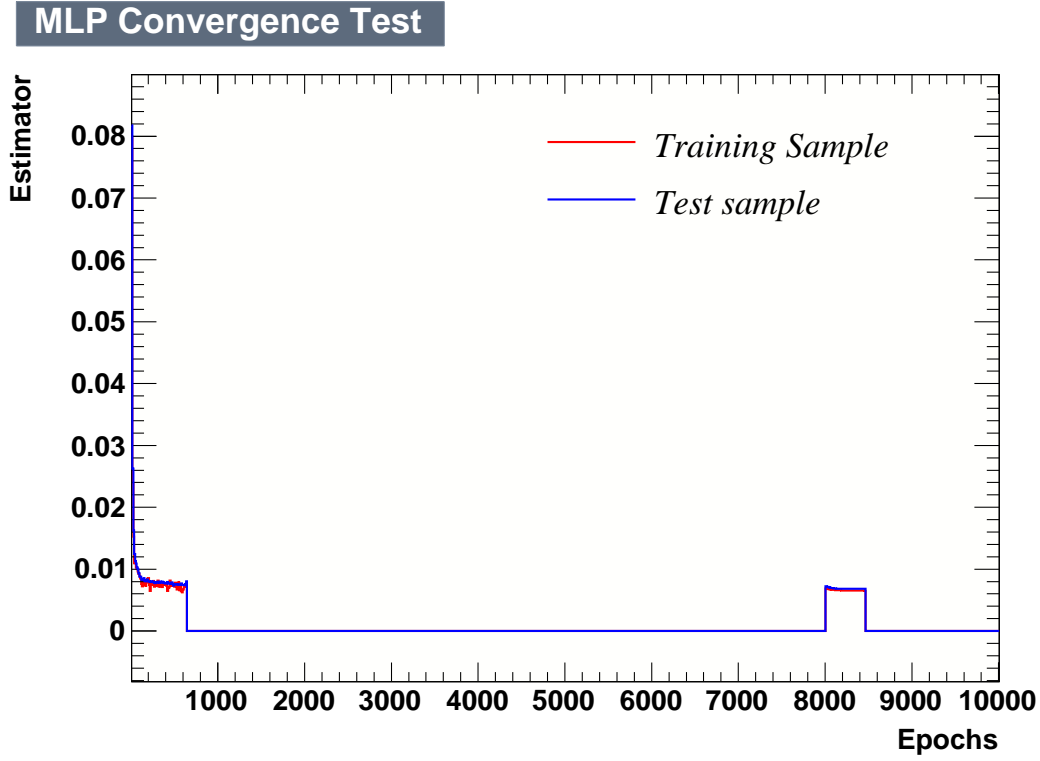
Figure 5.8: Convergence test for the MLP method.

training and testing samples.

5.4.3 Di-Jet p_T Imbalance

After we made the p_T correction for each jet, a di-jet transverse momentum imbalance distribution can be calculated. These distributions are shown in Fig. 5.10 before the correction, and in Fig. 5.11 after the correction. This distribution is more balanced (the mean is closer to zero) after the correction, and the average size of the imbalance (RMS) is significantly reduced. This means that the corrections we made really do work as expected.
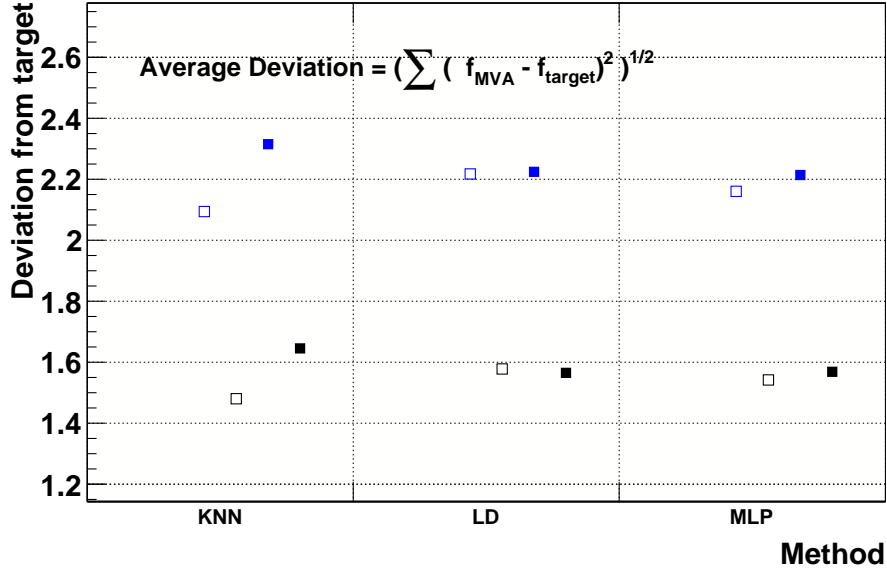
Figure 5.9: Average quadratic deviations for different machine learning methods.
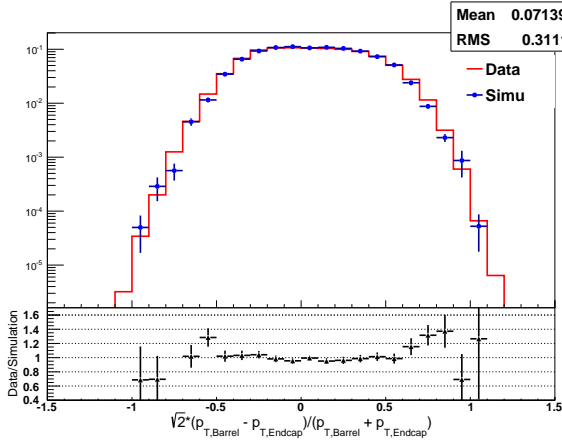
Figure 5.10: Uncorrected relative difference in p_T for back-to-back Barrel-Endcap di-jets.
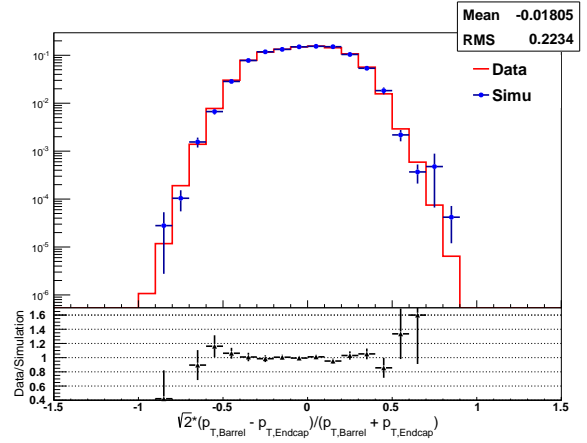
Figure 5.11: Corrected relative difference in p_T for back-to-back Barrel-Endcap di-jets.

5.5 Jet Mass Correction

Even though the jet invariant mass is small compared to the jet transverse momentum, and may not contribute much in a dijet invariant mass calculation, it is still an important jet property and is not negligible in calculating the dijet invariant mass. The detector-level jet invariant mass tends to be lower than its real value, as will be shown below. Hence, similar corrections are also made here to correct the jet invariant mass back to its true value (particle level).
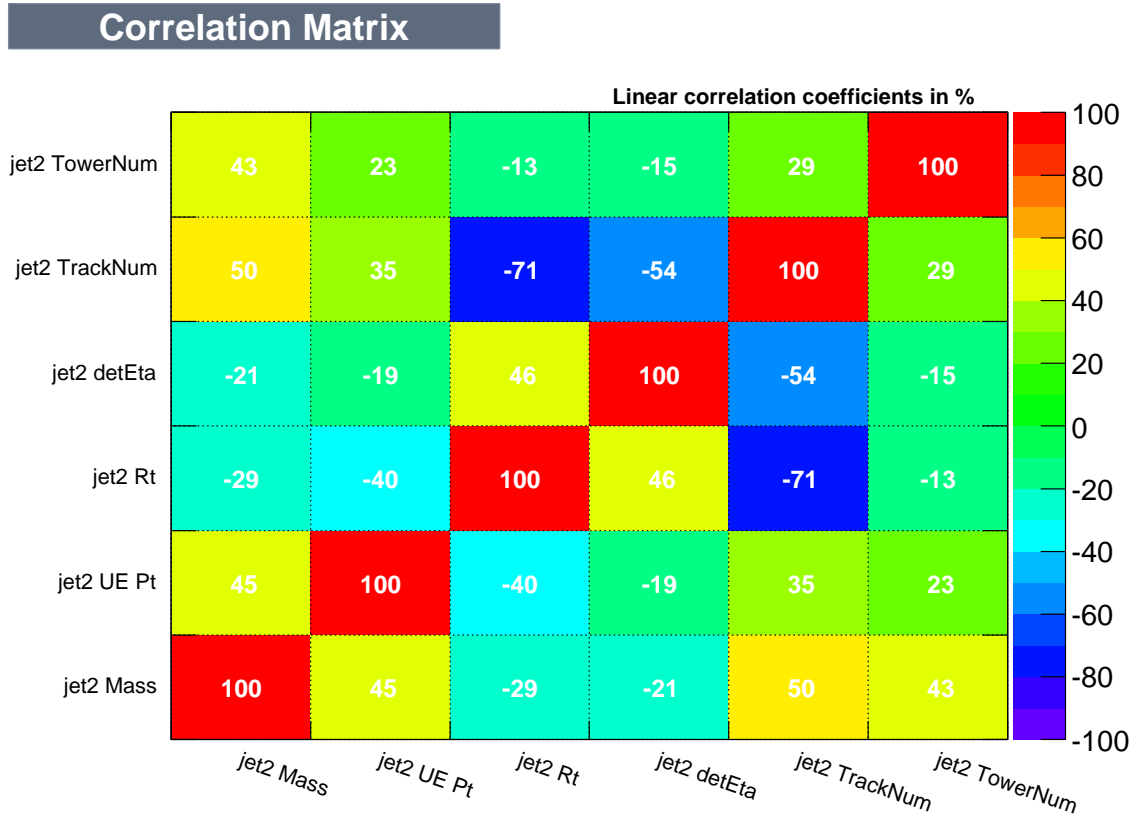
Figure 5.12: Correlation between different variables for Endcap jet mass corrections.

The invariant mass of the jet and detector pseudorapidity $\eta_{detector}$ are the two key inputs in this correction. The jet p_T, neutral fraction R_t, track multiplicity n_{track} and tower multiplicity n_{tower} relate to the jet's content, and serve as important extra inputs that should benefit the learning process. Fig. 5.12 shows the correlations among different variables. The variables are generally correlated in ways that are expected. Jet tower and track multiplicities are positively correlated

with the jet transverse momentum and its invariant mass. Jet invariant mass is also negatively correlated with the detector pseudorapidity, which means the falling tracking efficiency at higher pseudorapidity also affects the jet invariant mass measurement. Hence the choice of variables used here is reasonable.

After making the Underlying Event subtraction, a lot of jets have a mass close to zero, as shown in Fig. 4.4, which means these jets are almost massless. The large number of zero-mass samples would effect the training process, and may lead to biased results. To solve this problem, the correction was only applied if the jet mass was larger than 0.2 GeV. For the jet invariant mass (for both Barrel and Endcap jets), the method and variables are chosen as below:

- Method: Multilayer Perceptron (MLP).

- Variables: detector level jet mass m_{jet}, detector level p_T, detector pseudorapidity $\eta_{detector}$, neutral fraction R_t, track multiplicity n_{track}, tower multiplicity n_{tower}.

- Target: particle level jet invariant mass.

The JP2, JP1 and UnJP samples are trained separately, same as before. In Figs. 5.13 and 5.15, we show the Barrel and Endcap jet particle level invariant mass over its uncorrected values before the mass correction. The overall spread and differences are large. In Figs. 5.14 and 5.16 are shown the same plots after mass correction, demonstrating large improvements due to this correction.
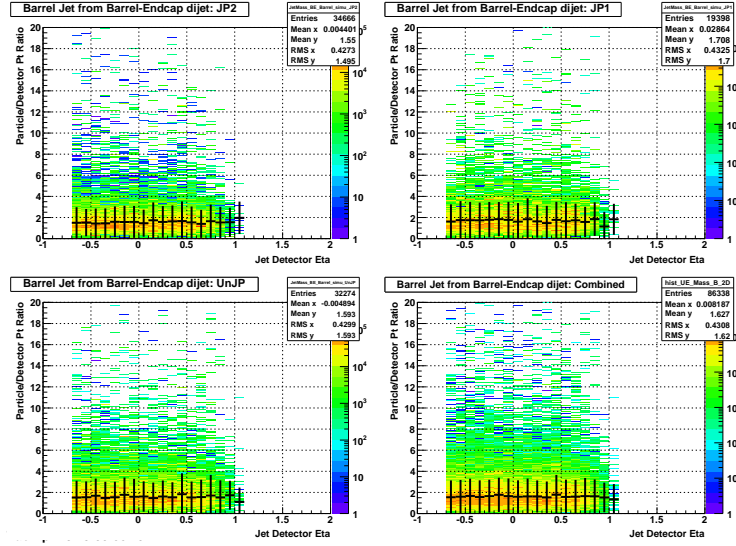
Figure 5.13: Mass shift: Barrel jet particle/detector mass ratio vs. detector η for different triggers.
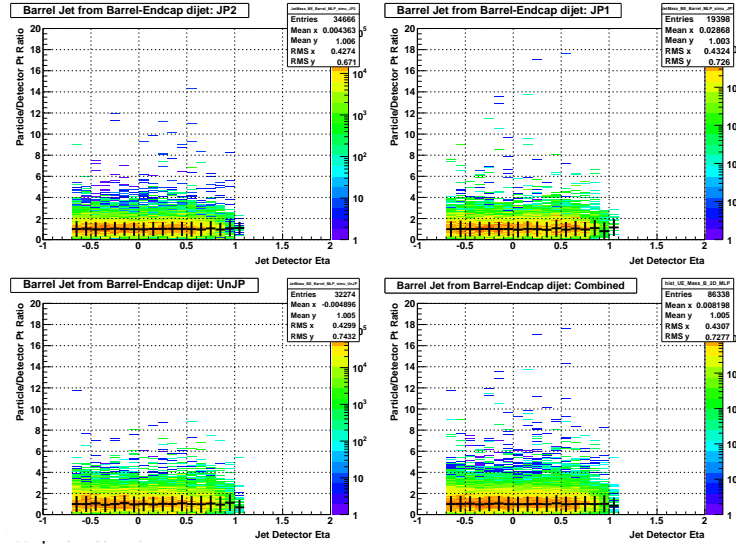
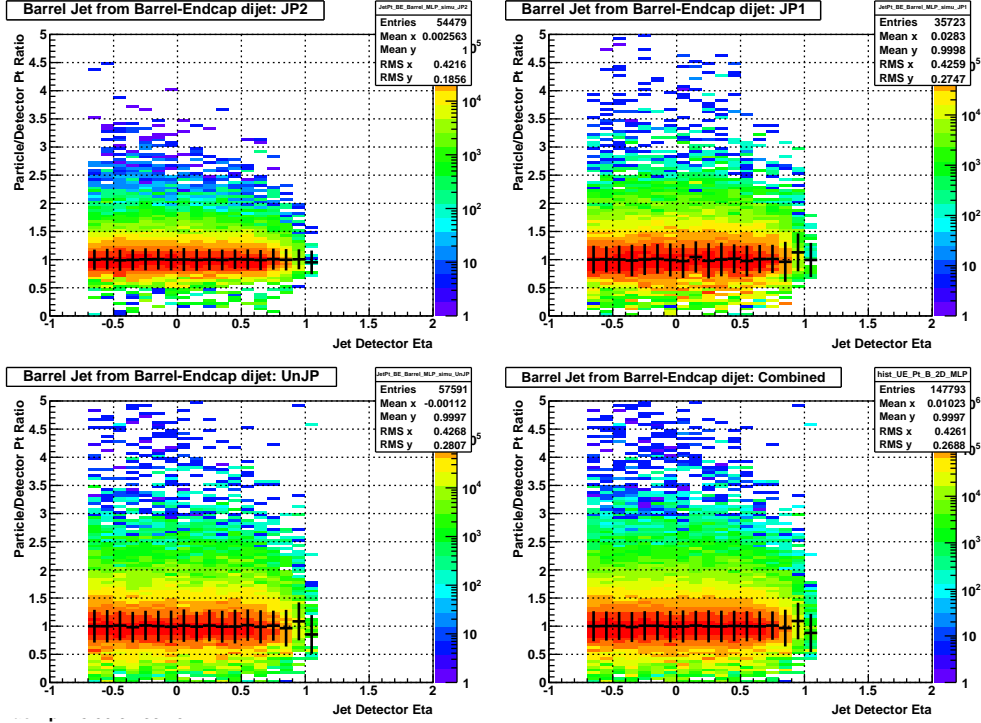
Figure 5.14: Mass shift: Barrel jet particle/output from the machine learning mass ratio vs. detector η for different triggers.
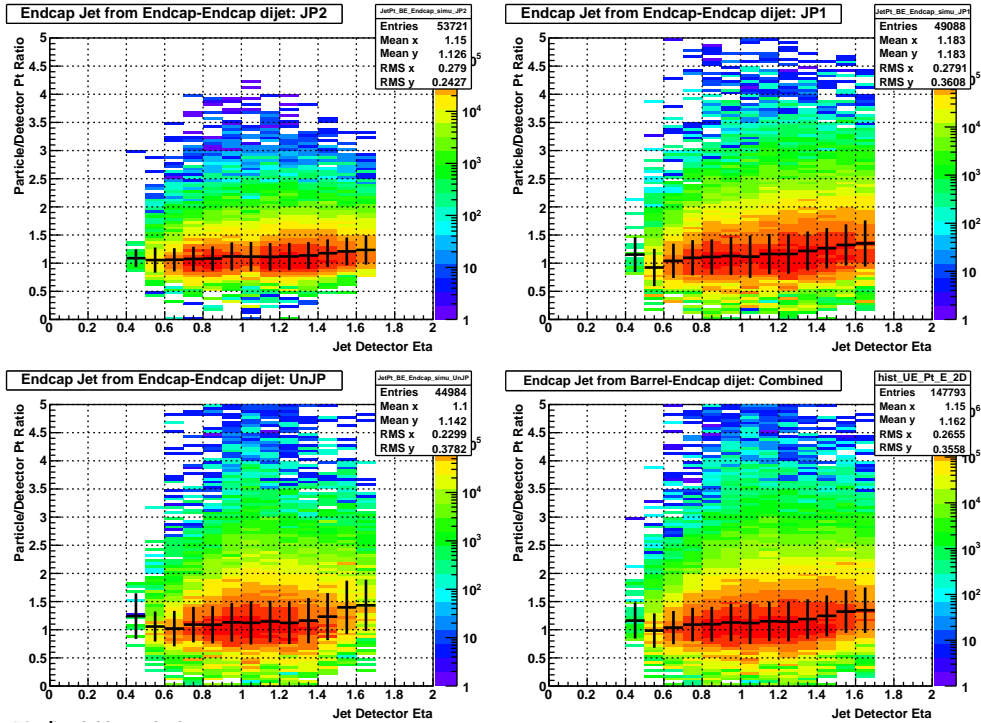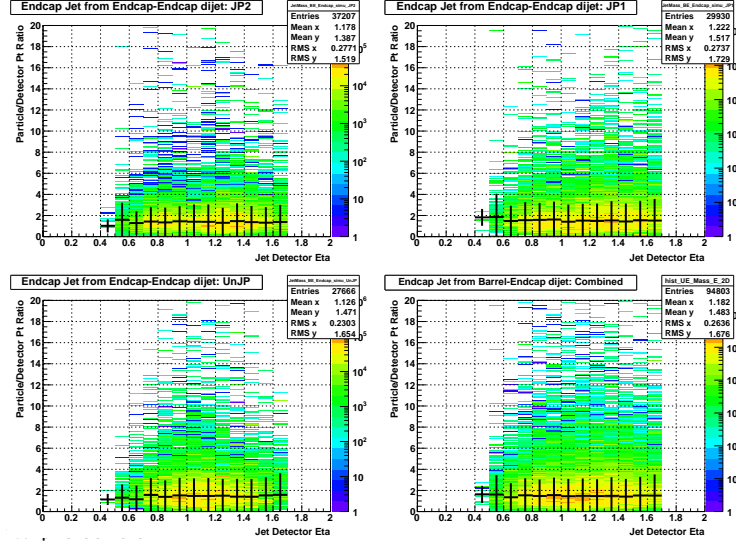
Figure 5.15: Mass shift: Endcap jet particle/detector mass ratio vs. detector η for different triggers.
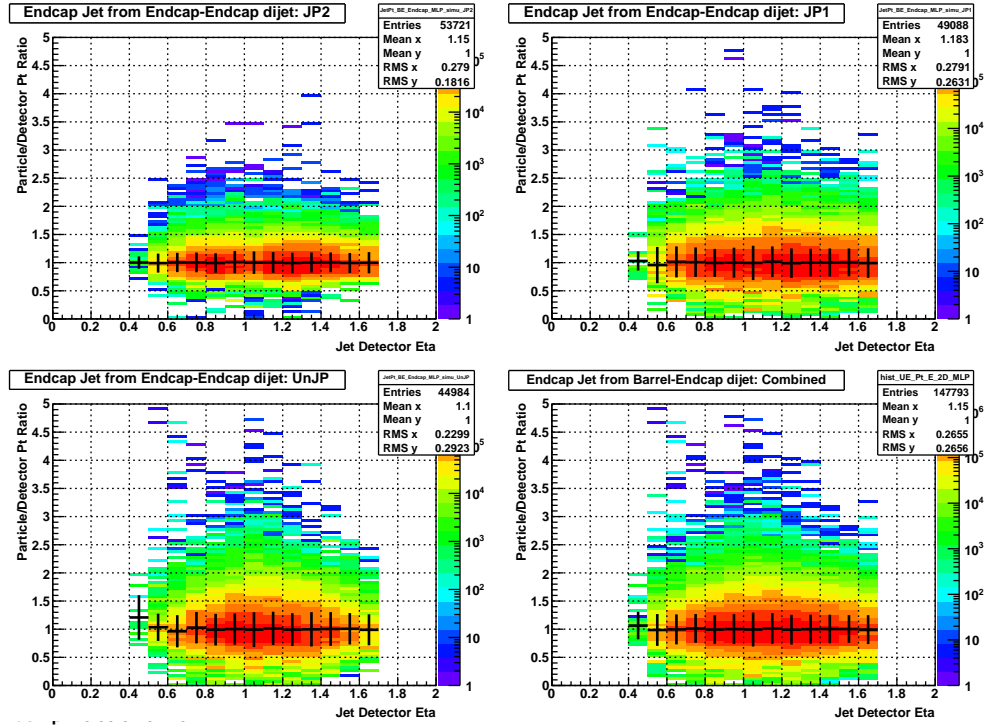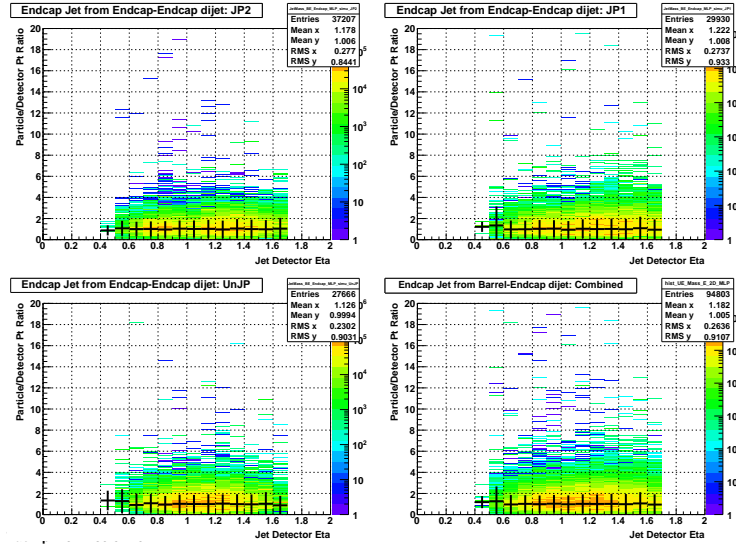

Figure 5.16: Mass shift: Endcap jet particle/output from the machine learning mass ratio vs. detector η for different triggers.

5.6 Other Jet Corrections

As discussed previously, Barrel and Endcap jets are separately corrected in p_T and mass. The corrected jet's 4-vector momentum then has the same direction, but improved values for p_T and mass after the corrections, as we describe below.

The jet pseudorapidity (η) and azimuthal angle (ϕ) are measured with very good precision. Figs. 5.17 and 5.18 show the jet η difference between particle level and detector level ($\eta_{true} - \eta_{measured}$) as a function of the jet detector pseudorapidity for Barrel and Endcap jets, respectively. The differences are small and no obvious bias is found in the spectra. Figs. 5.19 and 5.20 show the jet ϕ difference between particle level and detector level ($\phi_{true} - \phi_{measured}$) as a function of the jet detector pseudorapidity for Barrel and Endcap jets, respectively, which also look good. Hence we decided not to correct the jet direction (η, ϕ) in this analysis.

Event-by-event di-jet invariant mass comparisons are shown in Fig. 5.21. The left two plots are before we made the p_T and mass corrections and the right two plots are after we made the corrections. The upper two plots are distributions of the ratio of particle level di-jet mass over the detector level di-jet mass; the lower two plots are the difference of the two di-jet masses over their sum. The average ratio changes from 1.13 to 1.01, and the spread is narrower with about 15% improvement in the resolution. The difference ratio is also reduced from 0.048 to -0.008, and the distribution is also narrower. In general, the discrepancies between particle level and the detector level di-jet invariant mass are reduced, which is what we expected after making the corrections.
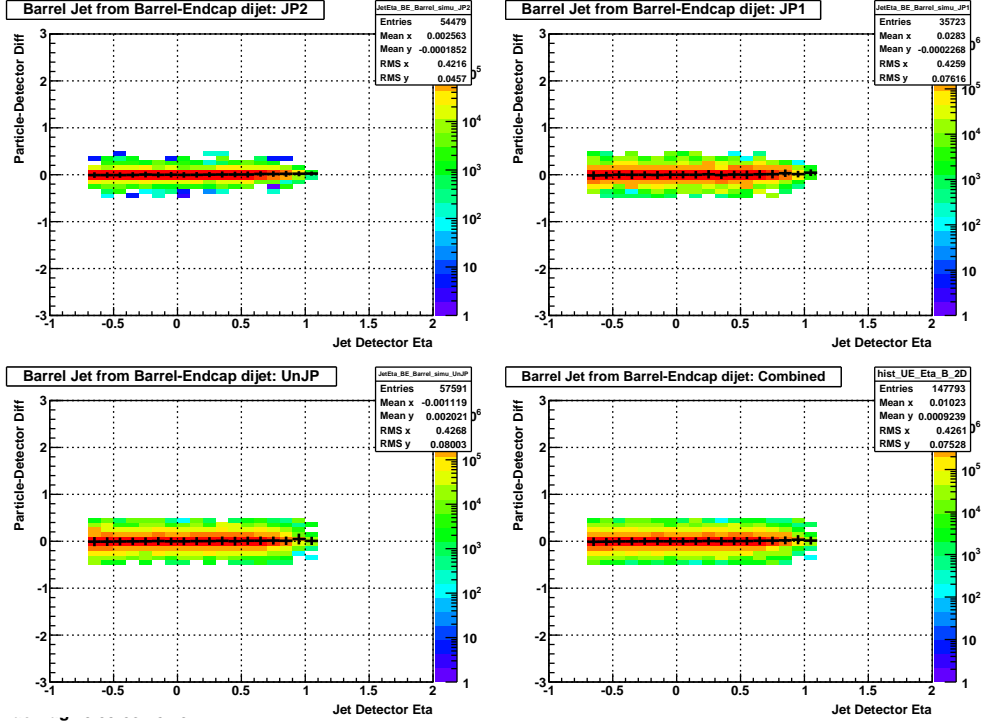
Figure 5.17: Barrel jet particle - detector η difference vs. detector η for different triggers.
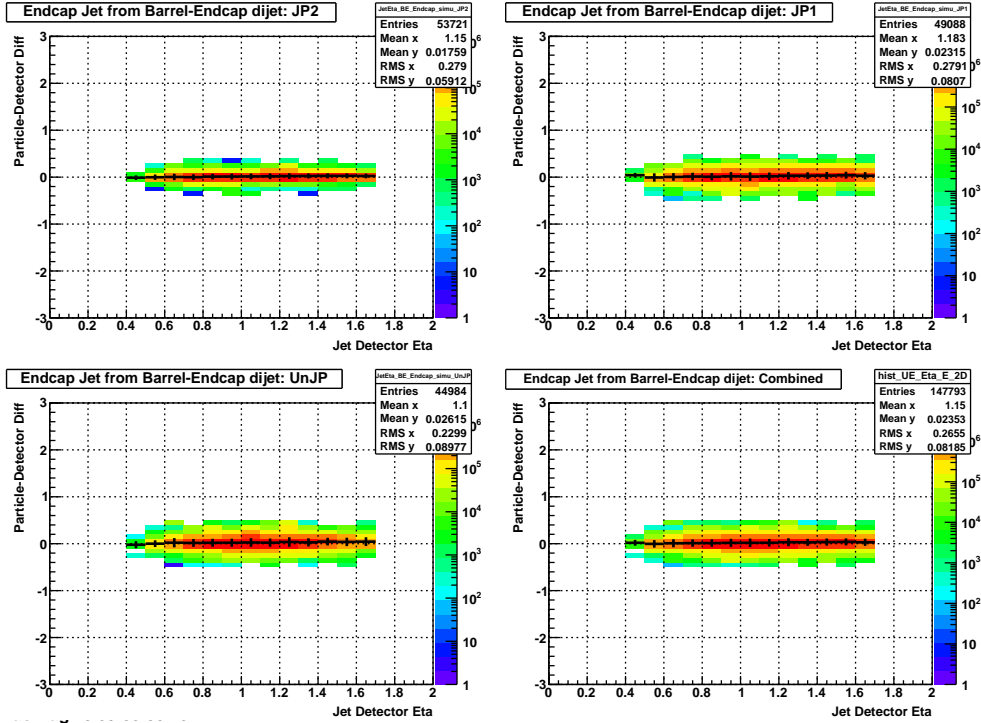
Figure 5.18: Endcap jet particle - detector η difference vs. detector η for different triggers.
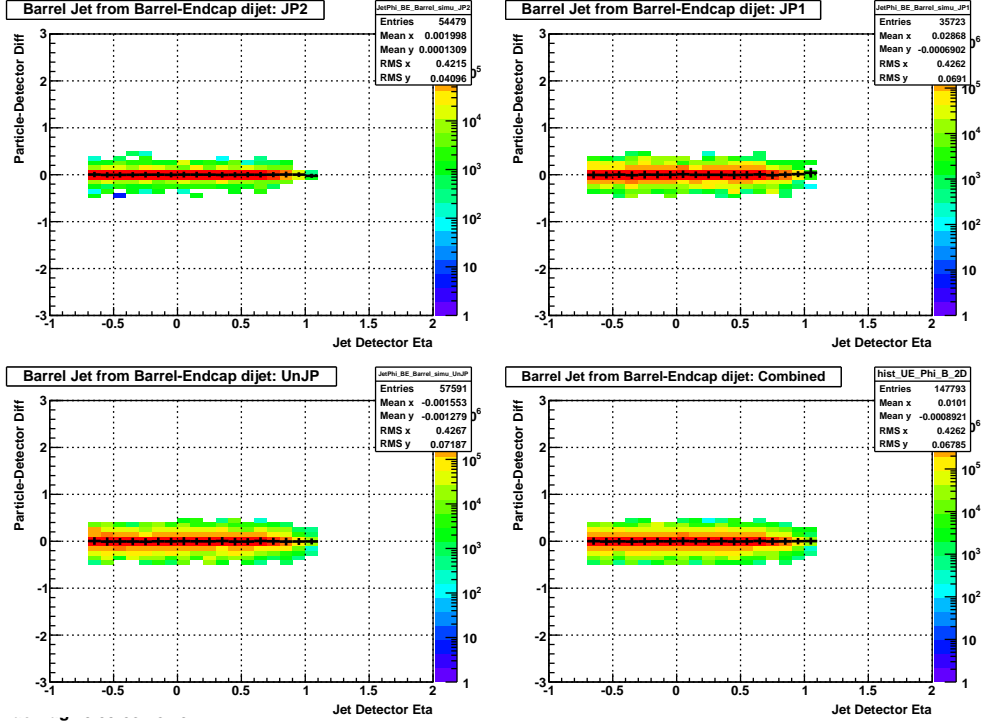
Figure 5.19: Barrel jet particle - detector ϕ difference vs. detector η for different triggers.
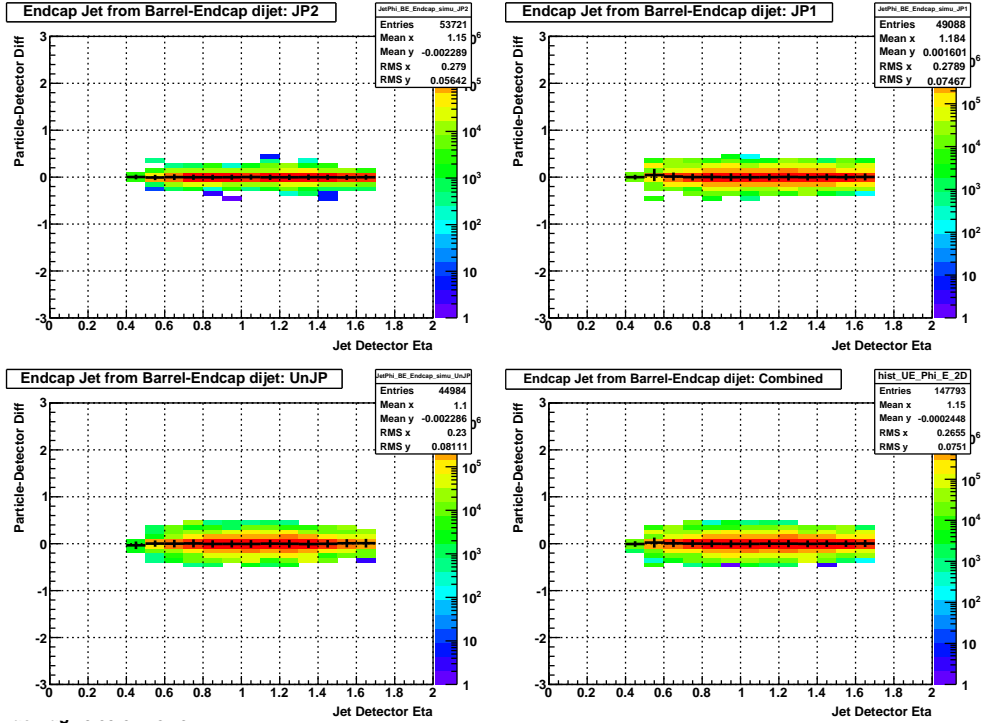
Figure 5.20: Endcap jet particle - detector ϕ difference vs. detector η for different triggers.
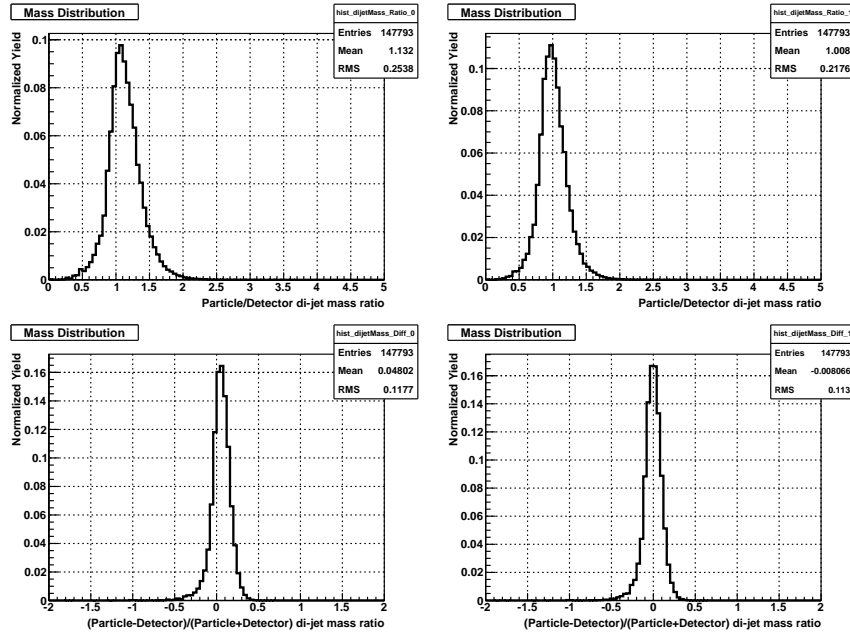
Figure 5.21: Di-jet mass comparision between the particle level and detector level: particle level over detector level ratio before the corrections are made (upper left); particle level over detector level after the corrections (upper right); difference ratio before corrections (lower left); difference ratio after corrections (lower right).

Chapter 6

Double spin asymmetries

As has been discussed in the first chapter, the main observable used to study the gluon polarization ΔG at RHIC is the longitudinal double-spin asymmetry, A_{LL}. STAR has presented A_{LL} measurements for inclusive jets [3], [7], dijet production at middle rapidity [8], and intermediate π^0 production [6]. These results have placed strong constraints on the gluon helicity distribution in the proton.

The longitudinal double-spin asymmetry, A_{LL}, is defined as:

$$A_{LL} \equiv \frac{\sigma_{++} - \sigma_{+-}}{\sigma_{++} + \sigma_{+-}}, \tag{6.1}$$

where σ_{++} and σ_{+-} are the differential production cross sections when the beam protons have equal and opposite helicities, respectively. Experimentally, sorting the yields by beam spin state enables a determination of the longitudinal double-spin asymmetry A_{LL} at STAR to be evaluated as:

$$A_{LL} = \frac{\sum (P_Y P_B)[(N^{++} + N^{--}) - R_3(N^{+-} + N^{-+})]}{\sum (P_Y P_B)^2[(N^{++} + N^{--}) + R_3(N^{+-} + N^{-+})]}, \tag{6.2}$$

where $P_{Y,B}$ are the polarizations of the yellow and blue beams, and N^{++}, N^{--}, N^{+-} and N^{-+} are the dijet yields from beam bunches with the same (first two) and opposite (latter two) helicity configurations, respectively. The first index denotes the helicity of the yellow beam, while the

second index shows the helicity of the blue beam bunches. R_3 is the ratio of the integrated luminosities for these configurations. The sum is over individual data runs, which generally ranged from 10 to 60 minutes in length, which is short compared to the nominal time required for changes in beam conditions. These will be discussed in the following sections.

The statistical error on A_{LL} is calculated using the usual error propagation techniques:

$$\delta A_{LL} = \frac{\sqrt{\sum (P_Y^2 P_B^2)[(N^{++} + N^{--}) + R_3^2 (N^{+-} + N^{-+})]}}{\sum (P_Y P_B)^2 [(N^{++} + N^{--}) + R_3 (N^{+-} + N^{-+})]}. \tag{6.3}$$

A detailed derivation is presented in appendix B.

6.1 Beam Polarization

As has been discussed in chapter 1, the beam polarizations are measured by the proton-Carbon (pC) polarimeters and a polarized hydrogen gas jet (H-Jet). The first is used to measure relative polarizations, and the gas jet is for absolute measurements. The beams are not 100% polarized, so the measured A_{LL} needs to be scaled by the polarizations. For the 2009 pp 200 GeV data, the average polarization was about 56% for the blue beam and 57% for the yellow beam.

In order to account for polarization loss over time, an initial polarization P_0, a slope $\frac{dp}{dt}$ (polarization change over time), and an initial time t_0 were also provided for each fill. During the data analysis, the value of the polarization was determined from the Unix timestamp t of each event using the equation:

$$P(t) = P_0 + \frac{dp}{dt}(t - t_0). \tag{6.4}$$

The average polarization value reported by the polarimetry group for each fill was weighted by the luminosity over the course of that fill. This means that as long as the number of events sampled scales proportionally with the luminosity, the average polarization would be the correct value to use. This proportionality roughly holds for the JP2 events, as that trigger was take-all throughout the run, so its event rate should scale with the instantaneous luminosity. The JP1 trigger, however,

was prescaled, and the prescale value was chosen in proportion to the instantaneous luminosity at the beginning of each run. This means that JP1 events are taken at a higher rate at the end of fills, when the luminosity is lower. Thus, using the average polarization value for the JP1 sample would tend to overestimate the beam polarizations appropriate for this sample. Calculating A_{LL} using the beam polarizations found as a function of event time alleviates this problem.

6.2 Spin Patterns

The collider assigns a spin pattern for each bunch crossing, which encodes the helicity of each beam in the collision. There are four spin patterns used for typical fills, and the polarization direction of each bunch in the two beams will match one of the patterns shown in Table 6.1. These four spin patterns were cycled through fill-by-fill over the course of Run 9. Only events with a valid spin pattern were retained.

Pattern	Yellow Beam	Blue Beam
P_1	+ + - - + + - -	+ - + - - + - +
P_2	+ + - - + + - -	- + - + + - + -
P_3	- - + + - - + +	+ - + - - + - +
P_4	- - + + - - + +	- + - + + - + -

Table 6.1: The four spin patterns used in 2009. The '+' indicates positive helicity and the '-' indicates negative helicity.

The colliding bunch helicity combination is encoded as a 'Spin-4' value at STAR, as indicated in Table 6.2. The information on the spin pattern for a specific event is stored in an offline database, so the Spin-4 value for any bunch crossing can be found easily. For a given spin pattern, each bunch crossing has a set Spin-4 value.

Spin-4	Yellow Beam	Blue Beam
5	+	+
6	-	+
9	+	-
10	-	-

Table 6.2: Spin pattern and polarization states.

Each bunch crossing is assigned a unique number (0-119). Those in the yellow abort gap (31-39) and the blue abort gap (111-119) were discarded, as these events arise from beam background only. The relative luminosity analysis found that bunch crossings 20, 60, 78, 79, and 80 were problematic in 2009, so all events from those bunch crossings were also dropped from the analysis.

6.3 Relative Luminosities

As shown in equation 6.2, the relative luminosities are needed between different spin patterns. The physics asymmetry defined in equation 6.1 measures the underlying physics process under the assumption that all spin state combinations are equally sampled. However, because there are only a limited number of bunch crossings available in the collider, and not all bunches have the same intensity, some spin state combinations may sample more luminosity than others. Therefore, each count must be normalized by the associated luminosity. The relative luminosity factors are ratios of helicity-combination luminosities, constructed in such a way to cancel out false asymmetries which would arise from the different combinations of the sampled luminosities. Getting the relative luminosities correct is an essential ingredient in the extraction of A_{LL} and other spin asymmetries.

For the 2009 $pp200$ data set, the relative luminosities were measured at STAR by the spin-sorted BBC coincidence yields, which have high rates and are independent of the detectors that are used to measure the dijet yields. Relative luminosities were also calculated using the ZDC system, and the difference between these two values (BBC and ZDC) was used in estimating systematic errors. More details can be found in [24].

There are six different relative luminosities for different spin pattern combinations:

$$R_1 = \frac{\mathcal{L}^{++} + \mathcal{L}^{-+}}{\mathcal{L}^{+-} + \mathcal{L}^{--}} \tag{6.5a}$$

$$R_2 = \frac{\mathcal{L}^{++} + \mathcal{L}^{+-}}{\mathcal{L}^{-+} + \mathcal{L}^{--}} \tag{6.5b}$$

$$R_3 = \frac{\mathcal{L}^{++} + \mathcal{L}^{--}}{\mathcal{L}^{+-} + \mathcal{L}^{-+}} \tag{6.5c}$$

$$R_4 = \frac{\mathcal{L}^{++}}{\mathcal{L}^{--}} \tag{6.5d}$$

$$R_5 = \frac{\mathcal{L}^{-+}}{\mathcal{L}^{--}} \tag{6.5e}$$

$$R_6 = \frac{\mathcal{L}^{+-}}{\mathcal{L}^{--}} \quad , \tag{6.5f}$$

where R_3 is the quantity needed to properly normalize the helicity-sorted yields in calculations of A_{LL}. The other luminosity ratios are useful in the calculation of the various false asymmetries.

6.4 False Asymmetries

In addition to the longitudinal double-spin asymmetry (equation 6.2), four other useful asymmetries can be calculated, as defined in equation 6.6. These four quantities provide checks on the analysis scheme, because they are expected to be zero in this data set:

$$A_L^{Y,B} = \frac{\sigma_+ - \sigma_-}{\sigma_+ + \sigma_-} \tag{6.6a}$$

$$A_{LL}^{ls} = \frac{\sigma_{--} - \sigma_{++}}{\sigma_{--} + \sigma_{++}} \tag{6.6b}$$

$$A_{LL}^{us} = \frac{\sigma_{-+} - \sigma_{+-}}{\sigma_{-+} + \sigma_{+-}} \quad . \tag{6.6c}$$

These false asymmetries can be expressed in terms of the measured spin yields, as shown in equation 6.7. A_L^Y and A_L^B measure the longitudinal single-spin asymmetries for the yellow and blue

beams. They arise from parity-violating effects due to the weak interactions, and are therefore expected to be negligible, relative to the statistical uncertainties. A_{LL}^{ls} and A_{LL}^{us} are the like and unlike sign double-spin asymmetries, and should be zero for the case of like helicities and opposite helicities in both beams. A_{LL}^{ls} is also sensitive only to parity-violating effects, while A_{LL}^{us} is expected to be null by rotational invariance, as collisions in which the yellow beam has positive helicity and the blue beam has negative helicity should be the same as the reverse case.

$$A_L^Y = \frac{\sum P_Y[(N^{--} + N^{-+}) - R_1(N^{++} + N^{+-})]}{\sum P_Y^2[(N^{--} + N^{-+}) + R_1(N^{++} + N^{+-})]} \tag{6.7a}$$

$$A_L^B = \frac{\sum P_B[(N^{--} + N^{-+}) - R_2(N^{++} + N^{+-})]}{\sum P_B^2[(N^{--} + N^{-+}) + R_2(N^{++} + N^{+-})]} \tag{6.7b}$$

$$A_{LL}^{ls} = \frac{\sum P_Y P_B(N^{--} - R_4 N^{++})}{\sum P_Y^2 P_B^2(N^{--} - R_4 N^{++})} \tag{6.7c}$$

$$A_{LL}^{us} = \frac{\sum P_Y P_B(R_6 N^{-+} - R_5 N^{+-})}{\sum P_Y^2 P_B^2(R_6 N^{-+} - R_5 N^{+-})} \quad . \tag{6.7d}$$

These four asymmetries provide important cross checks on the A_{LL} measurements, because the values for these asymmetries should be very small. Significant deviations from zero in any of these four asymmetries would indicate a problem with the calculation of relative luminosities or the asymmetry itself. Figs. 6.1, 6.2, 6.3 and 6.4 show these four additional asymmetries for the Barrel-Endcap dijet full sample ($-0.8 < \eta_1 < 0.8$ and $0.8 < \eta_2 < 1.8$), East Barrel-Endcap ($-0.8 < \eta_1 < 0.$ and $0.8 < \eta_2 < 1.8$), West Barrel-Endcap ($0. < \eta_1 < 0.8$ and $0.8 < \eta_2 < 1.8$) and Endcap-Endcap ($0.8 < \eta_{1,2} < 1.8$) dijet topologies, respectively. The 'false' asymmetries are found to have reasonable χ^2 values, and all the fits are consistent with zero.
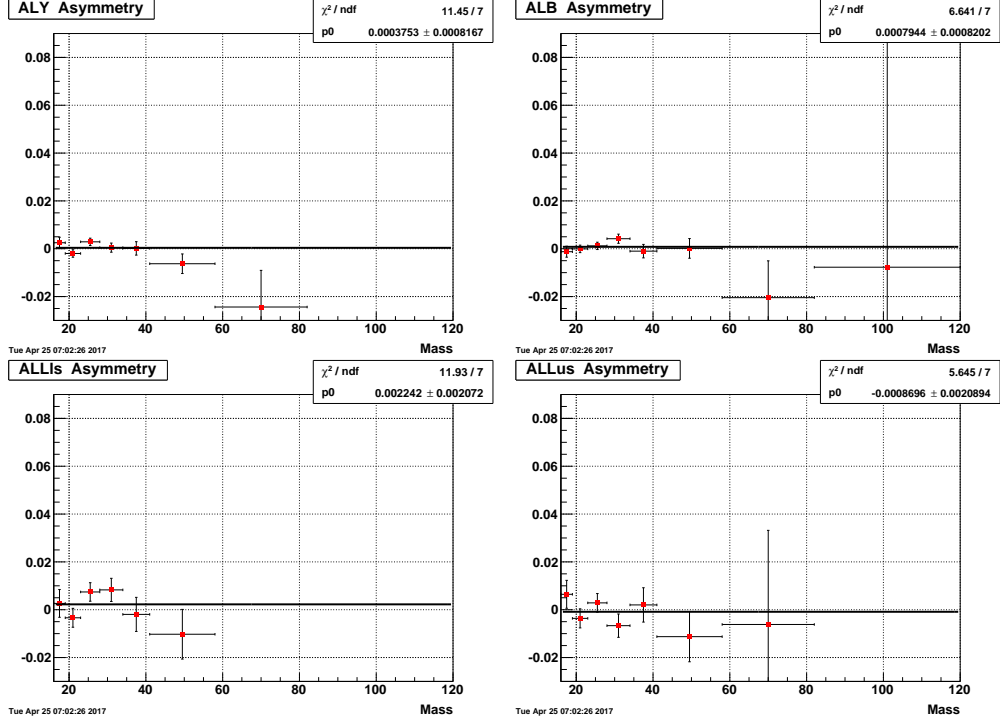
Figure 6.1: Dijet false asymmetries: Barrel-Endcap full topology.
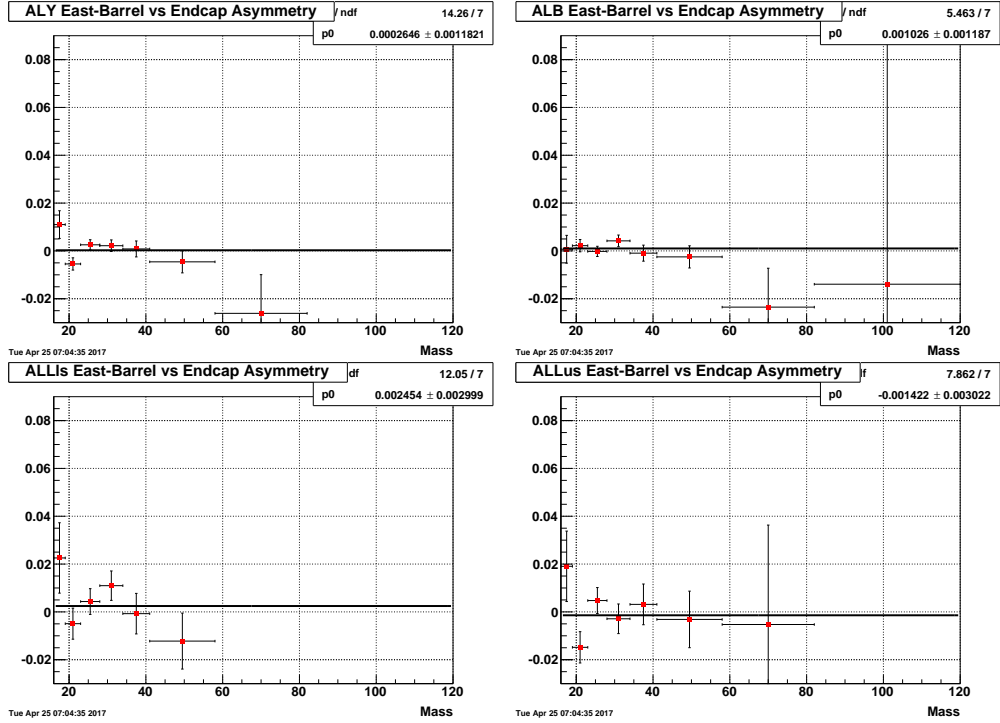
Figure 6.2: Dijet false asymmetries: EastBarrel-Endcap.

65
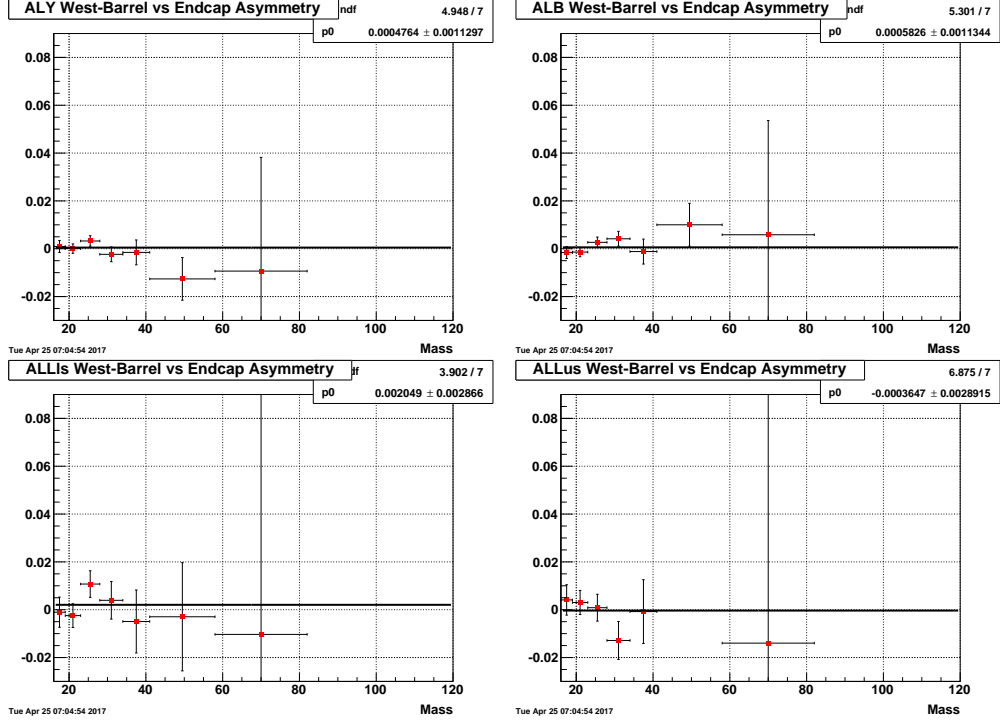
Figure 6.3: Dijet false asymmetries: WestBarrel-Endcap.
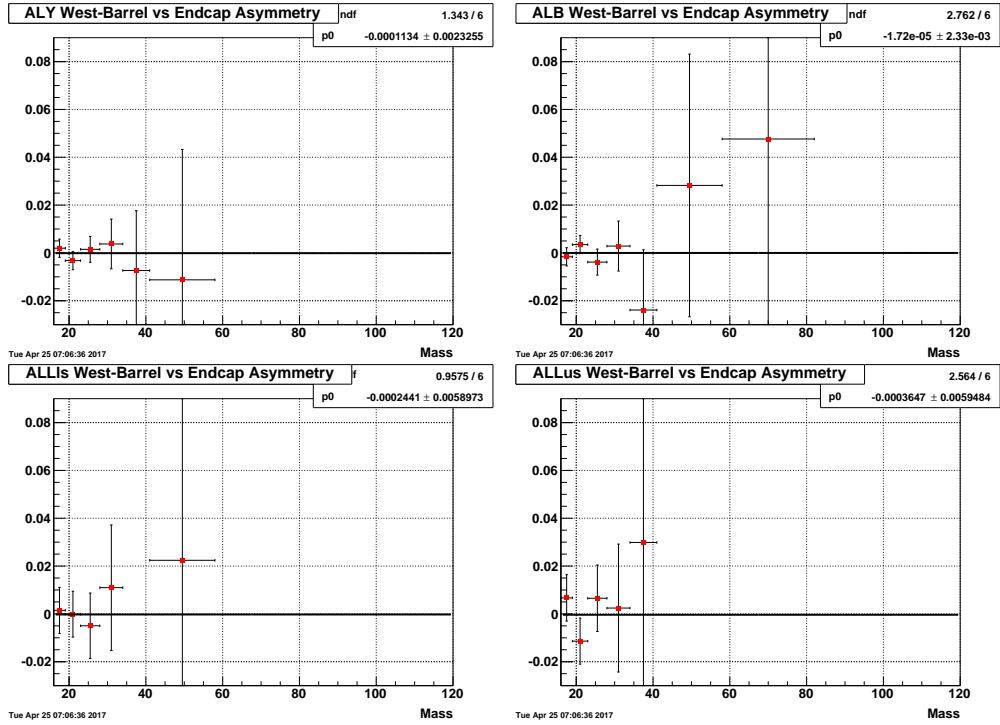
Figure 6.4: Dijet false asymmetries: Endcap-Endcap.

6.5 Data Corrections

Various corrections were applied for both the dijet invariant mass and the double-spin asymmetry. These corrections are summarized in tables 6.3 and 6.4, and discussed in more detail below.

6.5.1 Dijet Invariant Mass Shift

In order to compare our results with theoretical predictions, which are calculated at the parton level, a determination of the parton level dijet invariant mass of each data point was made by applying a simple mass shift to each point. This mass correction accounts for the difference in parton and particle level dijet invariant mass scales.

In previous jet-by-jet corrections, the jet energy had already been corrected back to particle level, so the mass shift is found by comparing the particle level dijet masses to the matching parton level dijet masses in simulation. For a given mass bin, the mass difference was calculated by finding the difference between the parton level dijet mass and the particle level dijet mass ($\Delta M = M_{parton} - M_{particle}$) event-by-event for all the dijets that fell into the given mass bin. The mass shift is the mean value of this calculation at each bin. The final data points are plotted at their average particle level mass + mass shift, which should be close to the average mass at the parton level. Fig. 6.5 shows the average mass shift for the four different dijet topologies.

6.5.2 Trigger and Reconstruction Bias

In parton-parton interactions, there are three different subprocesses that dominate: quark-quark (qq), quark-gluon (qg), and gluon-gluon (gg) elastic scattering. Values of A_{LL} extracted from the data represent an admixture of the asymmetries produced from these three dominant partonic scattering sub-processes. The mixture, however, can be altered in the measurement process. For example, the STAR jet-patch trigger may be more efficient for certain subprocesses. This would alter the sub-process fractions in the data set, compared to the underlying physical fractions, and

Barrel-Endcap Full Topology

Bin	Mass Bins (GeV)	Ave Mass(GeV)	Mass Shift(GeV)	A_{LL}	Trigger and Reco Shift
1	16 - 19	17.744	0.755 ± 0.112	-0.00511	0.00062 ± 0.00050
2	19 - 23	21.037	0.867 ± 0.079	0.01097	0.00079 ± 0.00039
3	23 - 28	25.315	0.995 ± 0.109	0.00439	0.00090 ± 0.00039
4	28 - 34	30.598	1.086 ± 0.286	0.00417	0.00102 ± 0.00063
5	34 - 41	36.893	1.346 ± 0.109	0.00156	0.00150 ± 0.00087
6	41 - 58	46.086	1.597 ± 0.119	0.01220	0.00234 ± 0.00107
7	58 - 82	63.704	1.755 ± 0.312	0.01933	0.00549 ± 0.00569

Endcap-Endcap

Bin	Mass Bins (GeV)	Ave Mass(GeV)	Mass Shift(GeV)	A_{LL}	Trigger and Reco Shift
1	16 - 19	17.535	0.965 ± 0.141	0.00172	-0.00017 ± 0.00077
2	19 - 23	20.786	0.915 ± 0.149	-0.00771	-0.00080 ± 0.00094
3	23 - 28	24.980	1.334 ± 0.151	0.02190	0.00071 ± 0.00145
4	28 - 34	30.167	1.569 ± 0.204	0.04309	0.00055 ± 0.00311
5	34 - 41	36.131	2.746 ± 0.390	0.08694	0.00907 ± 0.00519

Table 6.3: Dijet parton level corrections for Barrel-Endcap and Endcap-Endcap topologies.

East Barrel-Endcap

Bin	Mass Bins (GeV)	Ave Mass(GeV)	Mass Shift(GeV)	A_{LL}	Trigger and Reco Shift
1	16 - 19	18.070	0.370 ± 0.397	-0.01731	0.00052 ± 0.00062
2	19 - 23	21.215	0.895 ± 0.139	0.00638	0.00059 ± 0.00043
3	23 - 28	25.408	1.167 ± 0.168	0.00604	0.00119 ± 0.00038
4	28 - 34	30.677	1.538 ± 0.110	0.00264	0.00098 ± 0.00075
5	34 - 41	36.951	1.400 ± 0.144	-0.00622	0.00160 ± 0.00096
6	41 - 58	46.239	1.772 ± 0.145	0.01183	0.00192 ± 0.00104
7	58 - 82	63.835	1.892 ± 0.337	0.01883	0.00685 ± 0.00598

West Barrel-Endcap

Bin	Mass Bins (GeV)	Ave Mass(GeV)	Mass Shift(GeV)	A_{LL}	Trigger and Reco Shift
1	16 - 19	17.683	0.828 ± 0.109	-0.00285	0.00052 ± 0.00059
2	19 - 23	20.933	0.850 ± 0.093	0.01367	0.00060 ± 0.00048
3	23 - 28	25.217	0.805 ± 0.135	0.00263	-0.00010 ± 0.00045
4	28 - 34	30.469	0.323 ± 0.722	0.00667	0.00007 ± 0.00086
5	34 - 41	36.752	1.203 ± 0.118	0.02052	-0.00035 ± 0.00149
6	41 - 58	45.513	0.914 ± 0.162	0.01360	0.00227 ± 0.00260
7	58 - 82	62.568	0.256 ± 0.665	0.02360	-0.00776 ± 0.00556

Table 6.4: Dijet parton level corrections for the two Barrel-Endcap topologies.
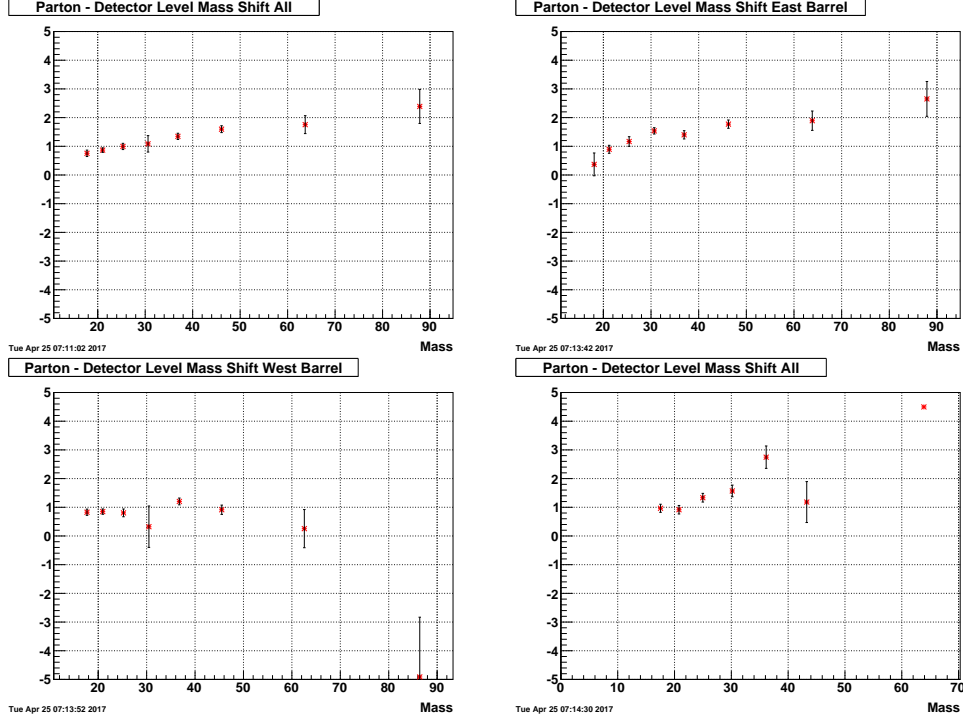
Figure 6.5: Dijet invariant mass shifts for Barrel-Endcap dijet full topology (upper left), East Barrel-Endcap (upper right), West Barrel-Endcap (lower left) and Endcap-Endcap topology.

thereby shift the measured A_{LL}. Further distortions can arise due to systematic shifts caused by the finite resolution of the detector coupled with a rapidly falling invariant mass distribution, which would thus change the subprocess fraction associated with a given mass. Jets with more neutral energy (high R_t) are preferentially selected in the Endcap due to the falling tracking efficiency, and R_t is also correlated with the sub-processes. To address these concerns, trigger and reconstruction bias corrections were applied to the raw A_{LL} values to compensate for these effects.

Determination of the biases introduced by the trigger and jet reconstruction depends on the details of the polarized parton distribution functions. These must necessarily be taken from theory, and so must account for the uncertainty in polarized gluon contributions. Parameterizations of the polarized parton distribution functions are combined with PYTHIA parton kinematic variables to generate predictions of A_{LL} vs. the dijet invariant mass for a particular model, at both the parton and detector levels. The NNPDFPol1.1 set [28] has 100 replicas and is therefore very applicable for this calculation.

69

The determination of the trigger and reconstruction bias correction follows the same procedure as has been used in the 2012 pp 200 GeV inclusive jet measurement analysis [18] using the 100 replica NNPDF sets:

1. For each event, find the parton level dijet from the full, unbiased PYTHIA sample. Apply only the $\Delta\phi$, jet η, and asymmetric p_T cuts. Plot A_{LL} from the polarized PDFs versus the parton level dijet mass. This is shown in the upper left plots of Figs. 6.6, 6.7, 6.8, and 6.9.

2. Fit the parton level theory curve with a 3rd order polynomial functions, extract the A_{LL} from the fitting functions (lower left plot in Figs. 6.6, 6.7, 6.8, and 6.9).

3. For each event, find the detector level dijet from the simulation sample which passed the trigger filter. Apply all detector level cuts, but do not require detector level to particle level matching. Plot A_{LL} of the polarized PDFs versus the detector level dijet mass (upper right plot in Figs. 6.6, 6.7, 6.8, and 6.9). Final A_{LL} is the trigger fraction weighted sum of the A_{LL} from the L2JetHigh and JP1 triggers. Place points at mass-weighted mean of the bin.

4. Calculate ΔA_{LL} for each mass bin at the shifted mass point. ΔA_{LL} is the difference between the parton and detector level A_{LL} evaluated at the shifted detector level mass. Values are shown in the lower right plots of Figs. 6.6, 6.7, 6.8, and 6.9.

The trigger and reconstruction bias correction in each mass bin was calculated by evaluating $\Delta A_{LL} = A_{LL}^{detector}(M_{detector}) - A_{LL}^{parton}(M_{detector} + \Delta M_{Shift})$ for the 100 replica NNPDF sets. The final correction is the average of the 100 ΔA_{LL}, which means the final data point is $A_{LL}^{final} = A_{LL}^{raw} - \Delta A_{LL}$.

The uncertainties of the detector level NNPDF values and the variation of the 100 ΔA_{LL} (RMS) were added in quadrature and were assigned as the systematic errors on the dijet A_{LL}:

$$\sqrt{UNC_{A_{LL}}^2 + RMS_{A_{LL,100}}} \tag{6.8}$$

The uncertainty for the parton level A_{LL} is very small compare to the statistical uncertainty of the detector level NNPDF vlaues, and is not taken into account here. In Fig. 6.6 are the plots used

for the correction estimation for the Barrel-Endcap full topology, Fig. 6.7 is the same for East Barrel-Endcap, Fig. 6.8 is for West Barrel-Endcap, and Fig. 6.9 is for Endcap-Endcap.
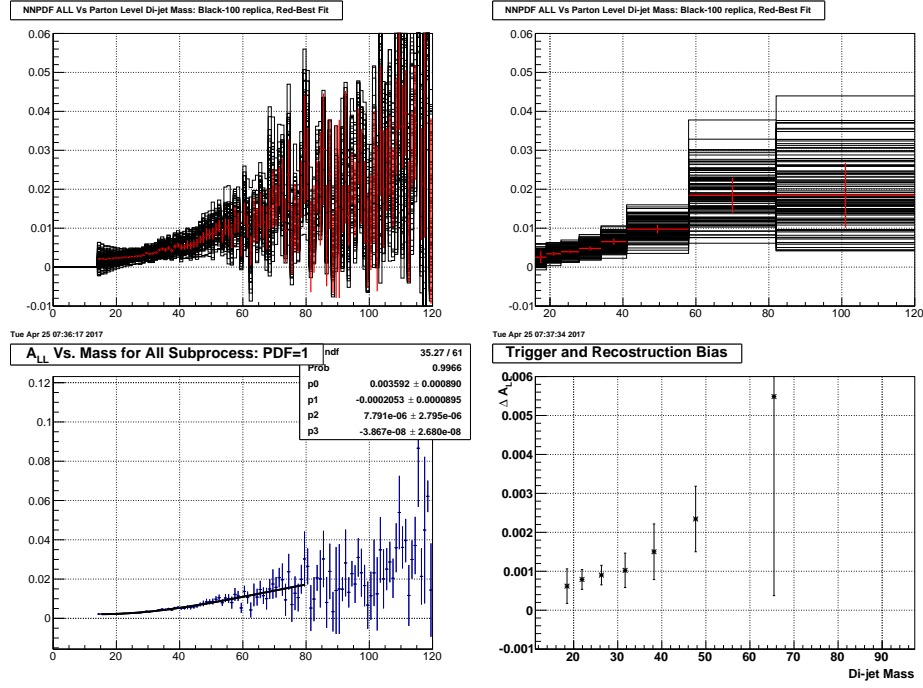
Figure 6.6: Dijet NNPDF 100 replica A_{LL} of the Barrel-Endcap full topology: parton level (upper left), detector level (upper right), parton level fit extractions (lower left) and final corrections (lower right).
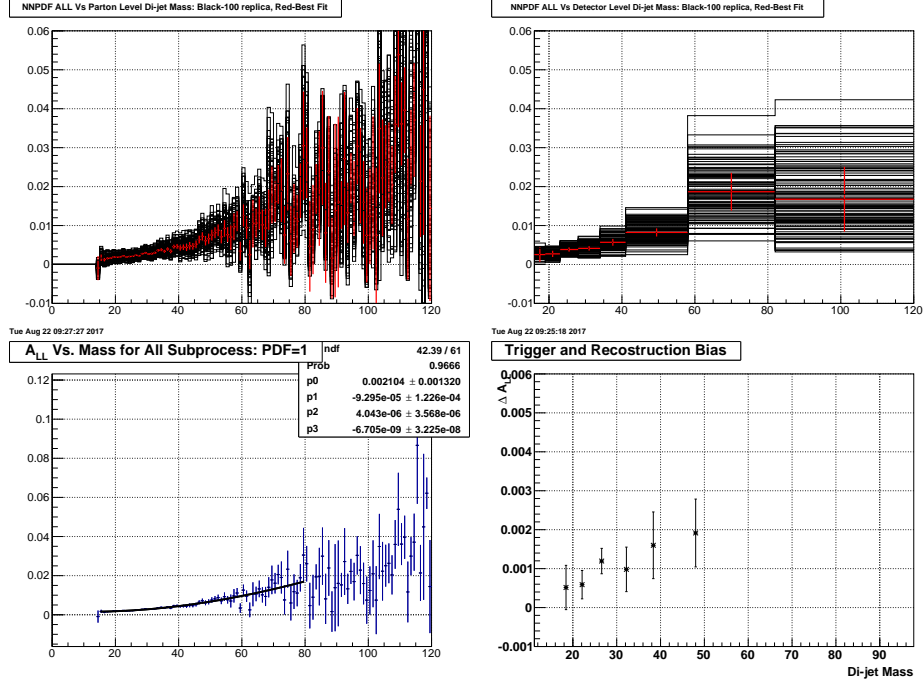
Figure 6.7: Dijet NNPDF 100 replica A_{LL} of the East Barrel-Endcap: parton level (upper left), detector level (upper right), parton level fit extractions (lower left) and final corrections (lower right).
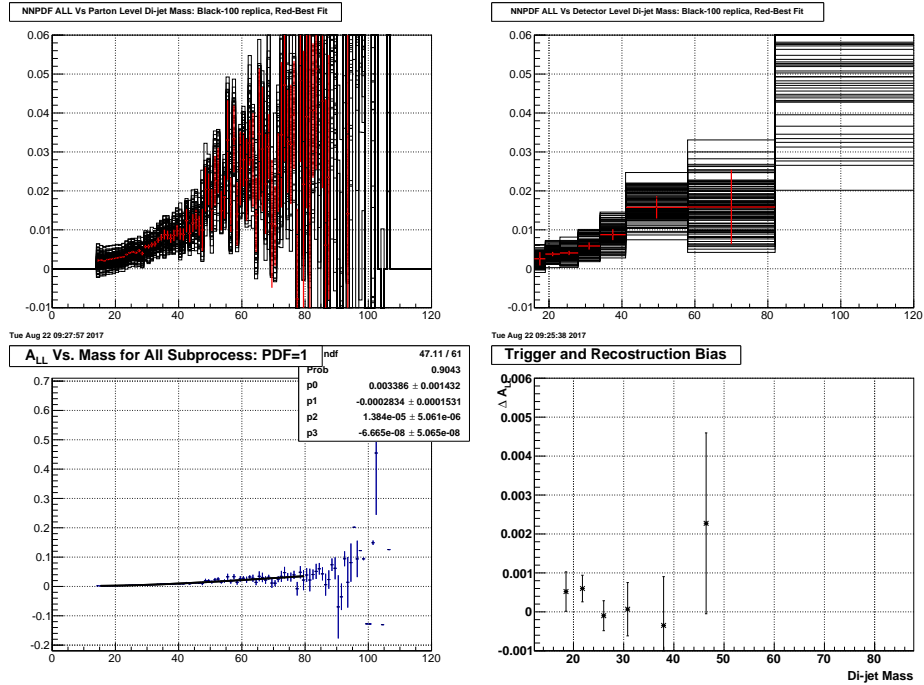
Figure 6.8: Dijet NNPDF 100 replica A_{LL} of the West Barrel-Endcap: parton level (upper left), detector level (upper right), parton level fit extractions (lower left) and final corrections (lower right).
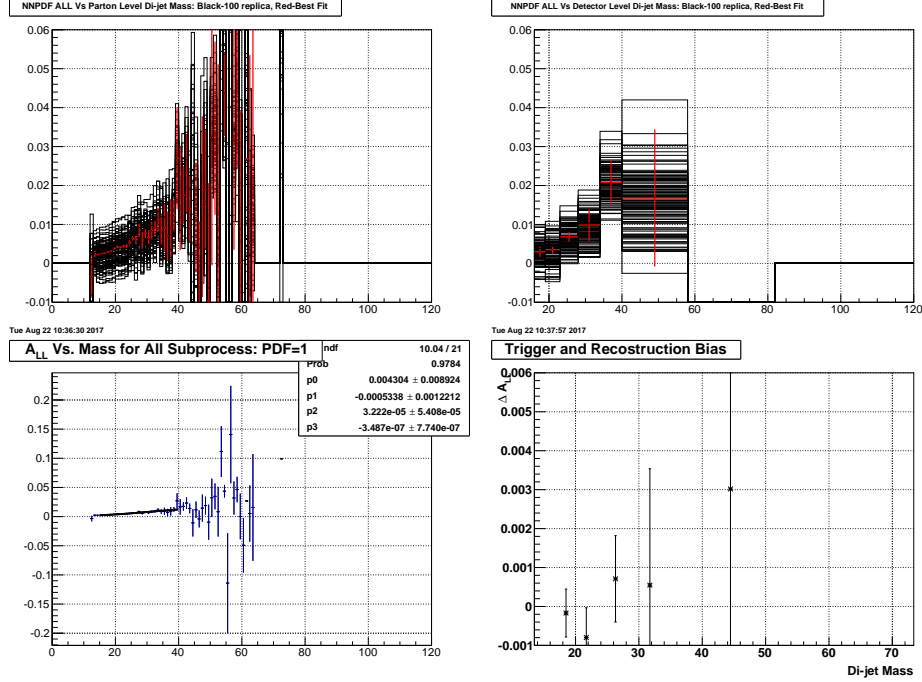
Figure 6.9: Dijet NNPDF 100 replica A_{LL} of the Endcap-Endcap: parton level (upper left), detector level (upper right), parton level fit extractions (lower left) and final corrections (lower right).

6.6 Systematic Errors

Most systematic errors were determined in the same way as used for the 2009 Barrel-Barrel dijet measurements [8]. The systematic uncertainties of the 2009 pp 200 GeV dijet A_{LL} were broken down into two categories: systematic errors on the dijet mass (x-axis uncertainties) and those on the A_{LL} values (y-axis uncertainties). The systematic errors on A_{LL} include the polarization uncertainty, the relative luminosity uncertainty, underlying event systematic uncertainty, trigger bias and reconstruction uncertainty, and the residual transverse double spin asymmetry uncertainty. The systematic errors on the dijet mass are due to the jet energy scale uncertainties, tracking efficiency uncertainties, jet p_T and mass shift uncertainties, dijet invariant mass shift uncertainties and PYTHIA tune uncertainties. Tables 6.10 and 6.11 summarize the errors on the dijet invariant mass, while Tables 6.12 and 6.13 are the errors on dijet A_{LL}.

The polarization uncertainty was determined by the RHIC polarimetry group and was found to be 6.5% [7]. The relative luminosity systematic is the same as from the inclusive jet analysis,

which evaluated BBC/ZDC differences and the false asymmetry magnitudes to arrive at a value of ±0.0005.

6.6.1 Residual Transverse Component

Due to imperfect tuning of the spin rotators in the collider, the polarization may acquire a residual transverse component. In conjunction with the C-AD group, the ratio of the transverse polarization over the total polarization $t = P_T/P$, and the azimuthal angles ϕ of the transverse polarization, were measured for both yellow and blue beams in the BBCs and ZDCs. Results are shown in Tables 6.5 and 6.6. Data taken before fill 10969 (run 10173048) has a large residual transverse polarization in the blue beam; then the spin rotators were adjusted to minimize that effect.

	ZDC	BBC
Yellow	$t = 0.16 \pm 0.02, \phi = -0.8 \pm 0.1$	$t = 0.15 \pm 0.02, \phi = -0.5 \pm 0.1$
Blue	$t = 0.27 \pm 0.01, \phi = -0.9 \pm 0.1$	$t = 0.25 \pm 0.02, \phi = -1.5 \pm 0.1$

Table 6.5: Transverse polarization factors before rotator adjustment.

	ZDC	BBC
Yellow	$t = 0.12 \pm 0.10, \phi = -1.4 \pm 0.8$	$t = 0.13 \pm 0.02, \phi = -0.5 \pm 0.1$
Blue	$t = 0.04 \pm 0.07, \phi = -2.2 \pm 1.9$	$t = 0.10 \pm 0.03, \phi = -1.4 \pm 0.1$

Table 6.6: Transverse polarization factors after rotator adjustment.

We assume that this systematic error would not change significantly in different detector regions, so we use exactly the same method as was used in the 2009 Barrel-Barrel dijet measurement, which was adopted from the 2009 inclusive jet paper [7]. The systematic is evaluated as:

$$\delta A_{LL} = |\tan \theta_Y \tan \theta_B \cos(\phi_Y - \phi_B) A_\Sigma|, \tag{6.9}$$

where θ and ϕ are the polar and azimuthal angles of the polarization vectors, and the $\tan \theta$ (equal to t = P_T/P) terms were calculated for the periods before and after the rotator tuning and then weighted by the fraction of the events collected during the respective periods. To simplify the

calculation, the $\cos(\phi_Y - \phi_B)$ term was set to 1. Because there was no transverse running during Run 9, the A_Σ values used were taken from Run 6. These values were all consistent with zero, so to be conservative, the statistical error on the A_Σ measurement was taken and used in the calculation of the systematic. The A_Σ were measured as a function of jet p_T. For a given dijet mass point, a linear extrapolation as used to get the δA_Σ at the p_T which is half of that mass, as shown in Fig. 6.10. δA_Σ was then scaled down by the product of the yellow and blue transverse components of the polarization, $\tan\theta_Y \tan\theta_B$, which were calculated separately from the BBC measurements. The $\tan\theta_Y$ and $\tan\theta_B$ were also weighted by the relative fraction of events before (91%) and after (9%) the rotator adjustments. The residual transverse double spin asymmetry uncertainty is of the same order of magnitude as the relative luminosity uncertainty. Final values are shown in Tables 6.12 and 6.13.
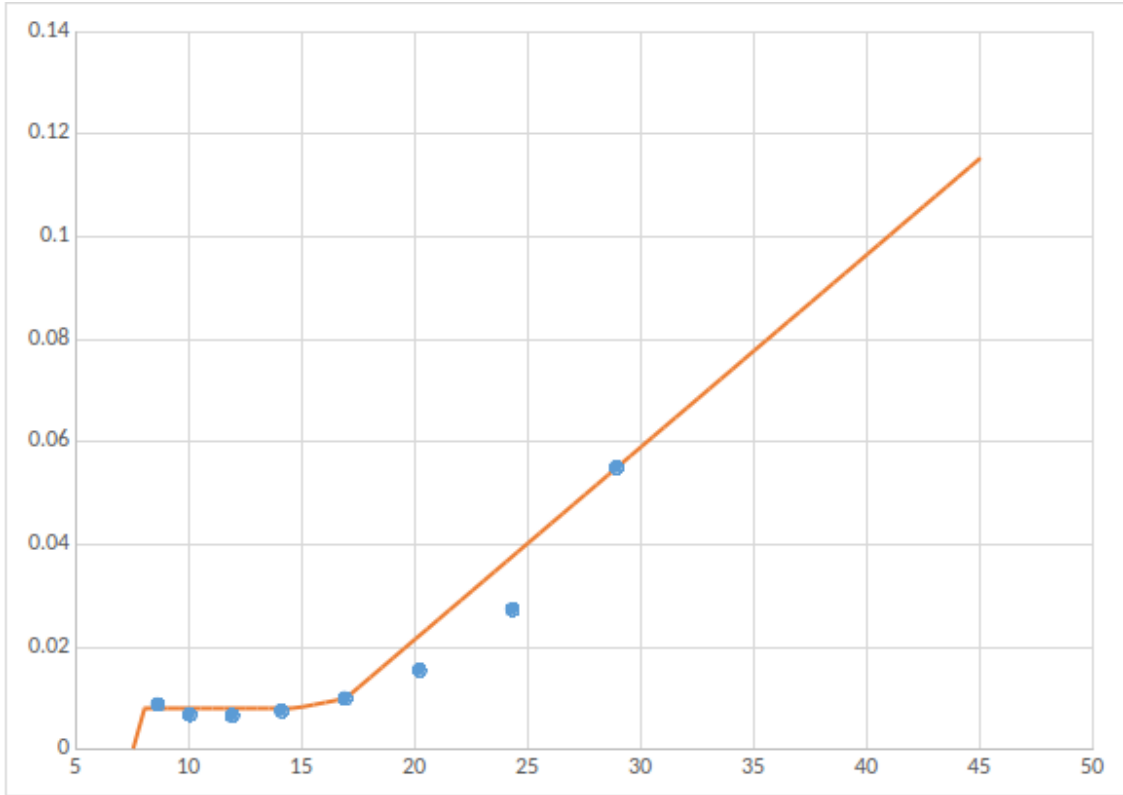
Figure 6.10: 2006 inclusive jet δA_Σ as function of the jet transverse momentum p_T.

6.6.2 Underlying Events Asymmetry
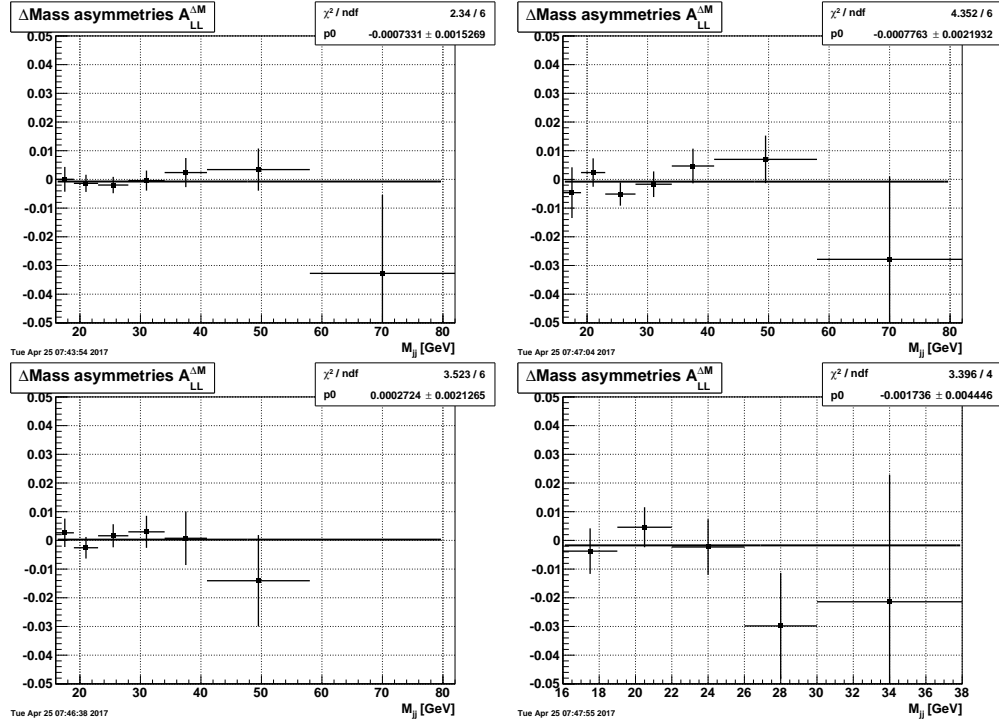
Figure 6.11: Dijet underlying events systematic: δA_{LL}, Barrel-Endcap full topology (upper left), East Barrel-Endcap (upper right), West Barrel-Endcap (lower left) and Endcap-Endcap(lower right).

The underlying event contribution to A_{LL} was determined by measuring the average underlying event correction ΔM and the $A_{LL}^{\Delta M}$ in the data:

$$A_{LL}^{\Delta M} = \frac{1}{P_Y P_B} \frac{(\langle \Delta M \rangle^{++} + \langle \Delta M \rangle^{--}) - (\langle \Delta M \rangle^{+-} + \langle \Delta M \rangle^{-+})}{(\langle \Delta M \rangle^{++} + \langle \Delta M \rangle^{--}) + (\langle \Delta M \rangle^{+-} + \langle \Delta M \rangle^{-+})} \quad , \tag{6.10}$$

where $\Delta M = M_{dijet} - M_{dijet,UE}$. $M_{dijet,UE}$ is the dijet invariant mass after the underlying event correction. Since the beams are not 100% polarized, beam polarizations are included in this calculation. The final $A_{LL}^{\Delta M}$ is the weighted average of values from each fill.

Fig. 6.11 shows the final measured $A_{LL}^{\Delta M}$ values for all the dijet bins, and the results from a zero-th order polynomial fit. The measured $A_{LL}^{\Delta M}$ comes directly from the data, and has not been corrected for effects due to finite detector efficiencies, etc. The fitted results show the value is consistent with zero across all bins.

To estimate the underlying event contribution, it is assumed that the underlying event adds extra energy to the jet, which effectively shifts the dijet spectrum in the positive direction. Adopting the equation from the 2012 pp 500 GeV inclusive jet analysis [18]:

$$\delta A_{LL}^{\Delta M} = \frac{\int_{M_{min}-\langle\Delta M\rangle\times A_{LL}^{\Delta M}}^{M_{max}-\langle\Delta M\rangle\times A_{LL}^{\Delta M}} \frac{d\sigma}{dm}dm - \int_{M_{min}+\langle\Delta M\rangle\times A_{LL}^{\Delta M}}^{M_{max}+\langle\Delta M\rangle\times A_{LL}^{\Delta M}} \frac{d\sigma}{dm}dm}{\int_{M_{min}-\langle\Delta M\rangle\times A_{LL}^{\Delta M}}^{M_{max}-\langle\Delta M\rangle\times A_{LL}^{\Delta M}} \frac{d\sigma}{dm}dm + \int_{M_{min}+\langle\Delta M\rangle\times A_{LL}^{\Delta M}}^{M_{max}+\langle\Delta M\rangle\times A_{LL}^{\Delta M}} \frac{d\sigma}{dm}dm} \quad , \tag{6.11}$$

where $\frac{d\sigma}{dm}$ is the unpolarized dijet cross section, and $\langle\Delta M\rangle$ is the mean spin-independent underlying event correction. Here the dijet cross section is taken from Ct10nlo [29].

6.6.3 Jet Energy Scale

The systematic error on the reconstructed dijet mass comes predominantly from the jet energy scale uncertainty. Contributions from the $\eta - \phi$ position uncertainties for individual jets are not considered. The energy deposited in the BEMC/EEMC has its uncertainty, which will contribute to the jet energy measured in this analysis. Both charged tracks and neutral particles deposit energy in the towers; thus the systematic uncertainty on the jet energy comes from both the neutral energy uncertainty and the track uncertainty. The jet energy scale uncertainties had contributions from two parts: one from the scale and status uncertainties of the EMC towers, and the other from the TPC track transverse momentum uncertainty and the tower track response uncertainty.

The tower scale uncertainties are scaled by the average neutral fraction of all jets in the dijet mass bin. The relative uncertainties for the EMC towers are below:

- For BEMC, tower status: 1.0%; scale uncertainty 4.6%; (from the 2009 pp 200 GeV BEMC calibration [8]).

- For EEMC, tower status: 1.0%; scale uncertainty 4.5%(from the 2009 pp 200 GeV π_0 anslysis [26]).

The hadron response uncertainty for the calorimeters is 0.025, from the 2009 pp 200 GeV Barrel-Barrel dijet measurement. The average EMC response to hadrons was taken to be 30%, and

Barrel-Endcap Full Topology		
Bin	$Jet_{Barrel}\ R_t$	$Jet_{Endcap}\ R_t$
1	0.467	0.521
2	0.468	0.540
3	0.460	0.559
4	0.440	0.570
5	0.416	0.574
6	0.397	0.572
7	0.388	0.557

Endcap-Endcap Full Topology		
Bin	$Jet_1\ R_t$	$Jet_2\ R_t$
1	0.551	0.509
2	0.536	0.535
3	0.479	0.547
4	0.435	0.513
5	0.413	0.480

Table 6.7: Average R_t for each jet in dijet mass bins.

the track response uncertainty was taken to be 9% (both taken from Ref. [21]). The tracking efficiency was estimated to be 81% [23] and the fraction of the EMC response in the projected tower was estimated as 50%. Finally, a scale factor from charged to total hadrons of 1/0.86 (from Ref. [21]) was used. The EMC tower hadron response uncertainty was then calculated as $(1/0.86 - 0.5 \times 0.81)/0.81 \times 0.30 \times 0.09 = 0.025$. So the calorimeter hadron response uncertainty is taken to be 2.5% for jet in Barrel.

The total jet energy scale systematic for Barrel jet is then taken as the quadrature sum of the BEMC scale uncertainty (which has been scaled by the neutral fraction), the track p_T uncertainty, and the hadron response uncertainty, both of which have been scaled by the average charged fraction.

Due to the tracking efficiency limit, jets in Endcap is different from that in Barrel. The average R_t for matched particle level jet in Endcap is about 0.5, and is about 0.7 for detector level jet at pseudorapidity around 1.3. Tracking efficiency is about 10%. So a scale factor is conservatively estimated as $1/(0.5 \times 0.3 \times 0.5) = 1/0.65$, and the uncertainty is then taken as $0.5 \times 0.3 \times 0.1 \times (1/0.65) = 0.023$. The jet energy scale systematic uncertainty is $\sqrt{0.045^2 + 0.01^2 + 0.023^2} = 0.0515$, and this value would not scale by the neutral energy fraction. The final used values are shown in the second column of table 6.10.

East Barrel-Endcap

Bin	Jet_{Barrel} R_t	Jet_{Endcap} R_t
1	0.471	0.487
2	0.473	0.519
3	0.466	0.557
4	0.448	0.577
5	0.421	0.585
6	0.398	0.584
7	0.383	0.565

West Barrel-Endcap

Bin	Jet_{Barrel} R_t	Jet_{Endcap} R_t
1	0.466	0.527
2	0.465	0.553
3	0.454	0.562
4	0.426	0.559
5	0.404	0.547
6	0.396	0.529
7	0.432	0.488

Table 6.8: Average R_t for each jet in dijet mass bins.

6.6.4 Tracking Efficiency Uncertainty

The uncertainty on the dijet mass due to tracking efficiencies in the TPC is also considered in this analysis. It is estimated by taking the difference of the average dijet invariant mass shift from detector level to parton level between (1) using the full set of reconstructed tracks from the TPC, and (2) by using a partial set of reconstructed tracks from the TPC. The partial set of reconstructed tracks from the TPC is usually chosen by randomly rejecting a certain percent of tracks from the full set before jet reconstruction. In this analysis, the rejection fraction was chosen to be 7%, which means rejecting seven tracks in every 100 tracks. The final results are shown in Fig. 6.12.

6.6.5 Dijet Mass Shift Systematic

The dijet invariant mass shift from particle to parton level has been presented in a previous section. The systematic error on the dijet mass shift was determined by adding in quadrature the errors from the two trigger samples, weighted by the trigger fractions. This error was dominated by the limited statistics of the simulation sample.
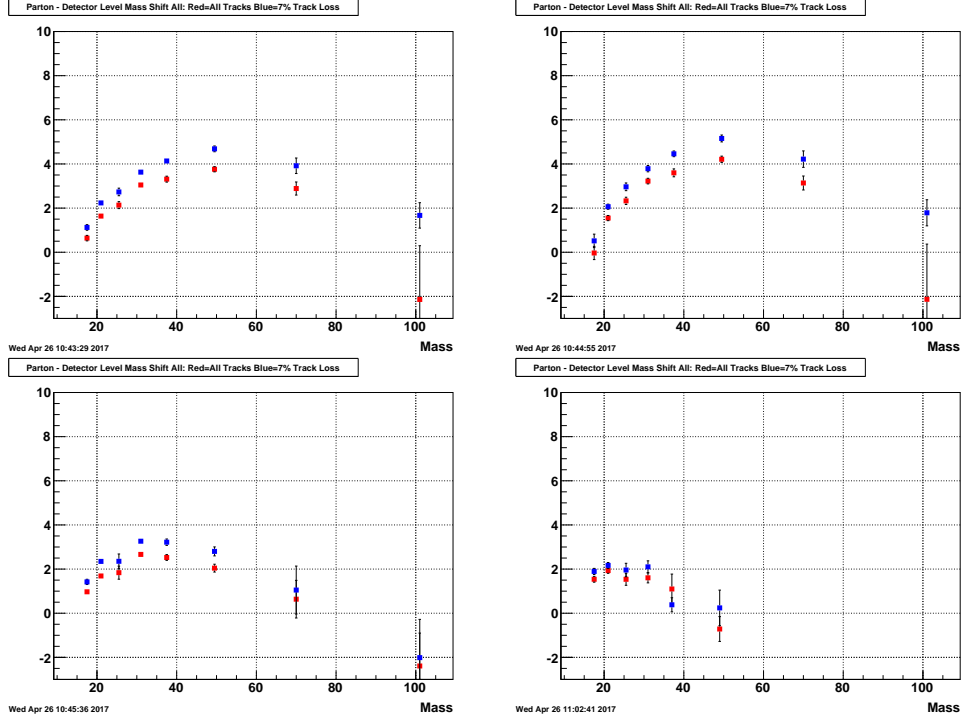
Figure 6.12: Dijet mass shift due to tracking inefficiency: 7% track loss (blue) and no track loss (red); Barrel Endcap Full topology (upper left); EastBarrel Endcap (upper right); WestBarrel Endcap (lower left); Lower right-Endcap Endcap (lower right).

6.6.6 Underlying Events Systematic Errors on Dijet Mass

The underlying event systematic uncertainty on jet energy was taken as the difference of the underlying event contribution to the dijet invariant mass between the data and simulation. Results are shown in Fig. 6.13.

6.6.7 PYTHIA Tune Uncertainties

Technically, PYTHIA parameters can be varied independently to fit various data sets. There are several tune sets available in PYTHIA. The dijet invariant mass shift uncertainties due to choice of the PYTHIA tune are estimated in the analysis by utilizing the possible variants provided for Perugia0 in the PYTHIA version of 6.4.26 and Perugia2012 in PYTHIA6.4.28. Table 6.9 lists some descriptions for specific PYTHIA tunes (see the PYTHIA tune manual [31] for more details).
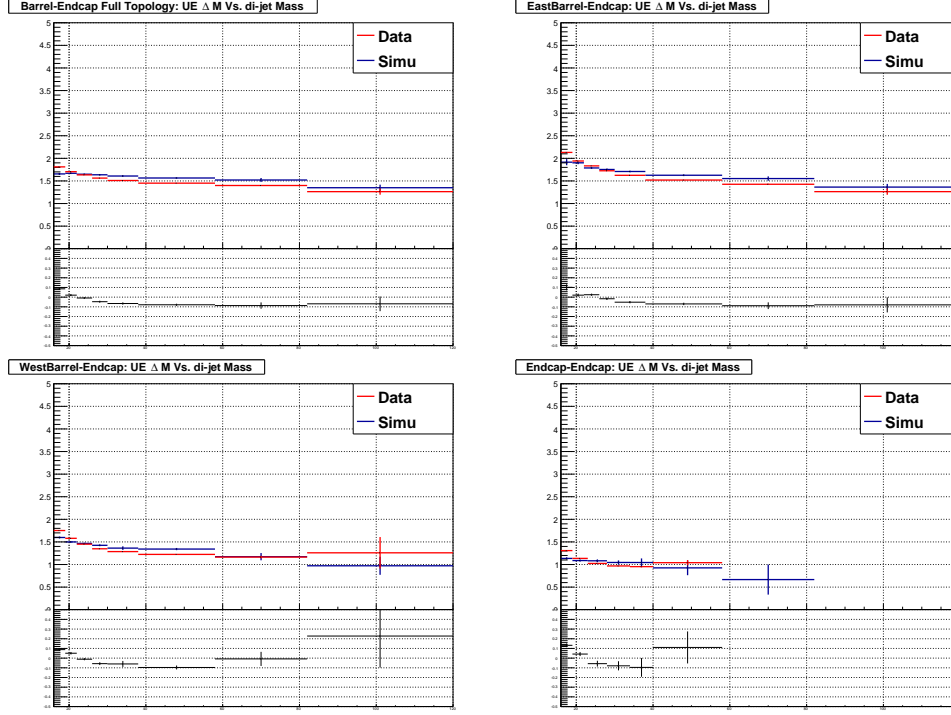
Figure 6.13: Dijet underlying event delta mass comparison for different topologies.

The mass shifts due to choice of PYTHIA tune were calculated using:

$$\Delta M = M_{parton} - M_{particle,UE} \tag{6.12a}$$

$$\delta M_{tune_i} = \Delta M_{tune_i} - \Delta M_{tune_{320}} \tag{6.12b}$$

$$\delta M_{tune} = (\Delta M_{tune_{321}} - \Delta M_{tune_{322}})/2 \tag{6.12c}$$

$$Systematic\ Errors = \sqrt{\Sigma_i \delta M_{tune_i}^2}, \tag{6.12d}$$

where $M_{particle,UE}$ is the dijet invariant mass after underlying event subtraction. We compare the mass shifts between the PYTHIA6.4.26 Perugia0 (Official 2009 pp 200 GeV embedding usage), Tune 321 to Tune 328 (Perugia0 related sets), and PYTHIA6.4.28(Official 2012 pp 500 GeV embedding usage). The differences among these shifts are the PYTHIA tune systematics, see Fig. 6.14. Tune 328 is related to underlying events, but the underlying event systematic on the dijet invariant mass was estimated by the disagreement in underlying event ΔM between the data and embedding sample, so tune 328 was not used. In addition, tunes 321 and 322 focus on the same

PYTHIA6.4.26 Perugia0	
Tune ID	Description
320	Default
321	HARD - higher amount activity from perturbative physics
322	SOFT - lower amount activity from perturbative physics
323	Different balance between MPI and ISR and a different energy scaling
324	NOCR - An update of NOCR-Pro
325	Uses the MRST LO* PDF set
326	Uses the CTEQ6L1 PDF set
327	FSR outside resonance decays increased to agree with the level inside
328	'K' factor on the QCD scattering cross sections used in the MPI
PYTHIA6.4.28 Perugia2012	
370	Default

Table 6.9: PYTHIA tune and its variants.

particular uncertainty test, so half of the absolute difference between the pair was used. The final values we used are the quadratic sum of the difference between those shifts from different tune sets.
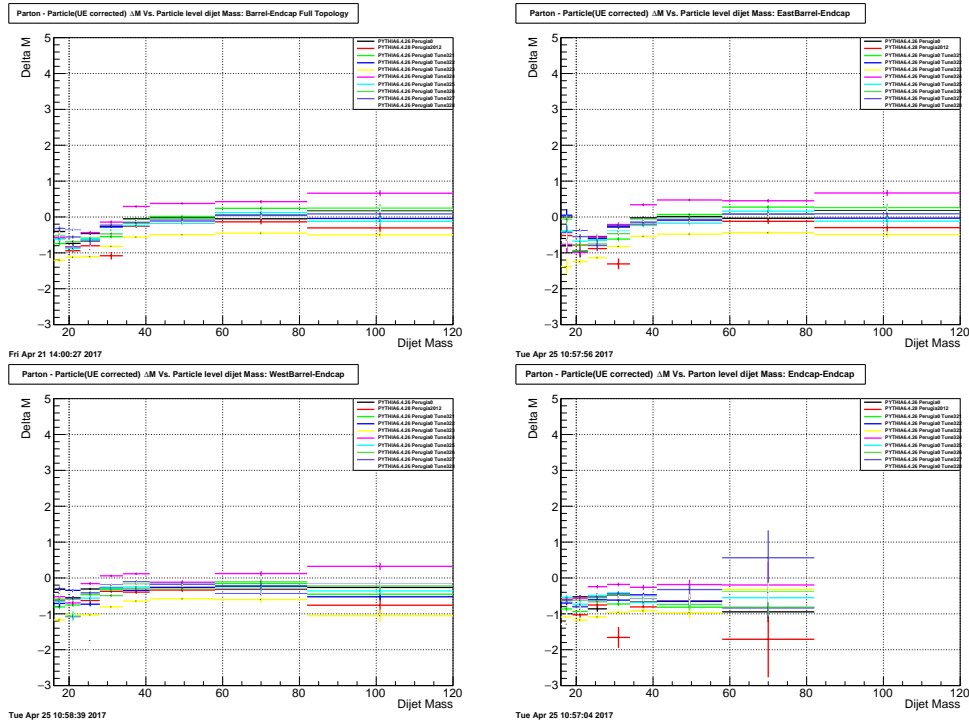
Figure 6.14: Dijet PYTHIA tune systematic: Barrel-Endcap full topology (upper left), East Barrel-Endcap (upper right), West Barrel-Endcap (lower left) and Endcap-Endcap (lower right).

6.6.8 Jet p_T and Mass Correction Systematic Uncertainties

The jet transverse momentum p_T and invariant mass M corrections were made using the machine learning method, as has been discussed in chapter 5. The Multilayer Perceptron is the main algorithm used in the correction. As noted before, for the MLP, a slight change of the parameters, such as the number of layers and nodes, may impact the learning process. Different algorithms may emphasize slightly different behaviors, which would also have some influence. So the systematic errors due to choice of machine learning algorithm were calculated in three different situations.

1. Different sample size used for training:

   - Systematic test 1: change the size of the data set used for training.

2. Different parameters for MLP:

   - Systematic test 2: change the number of layers.

   - Systematic test 3: change the number of neuron nodes.

3. Different machine learning methods:

   - Systematic test 4: use the linear discriminant (LD) method.

   - Systematic test 5: use the k-Nearest Neighbour (k-NN) method.

For each event, we can perform the jet p_T and mass corrections using the different settings and methods listed above. We then calculate the dijet invariant mass differences between these samples relative to the default standard setting (MLP). The results from different machine learning methods (LD and k-NN) and the different MLP settings (test 1, test 2, test 3) were added in quadrature. The square root of the quadrature sum is the final systematic error.

Barrel-Endcap Full Topology

Bin	Ave Mass	Energy	Tracking	Mass Shift	M.L.	UE Syst.	Tune Syst.	Total
1	18.499	0.533	0.242	0.112	0.122	0.156	0.875	1.077
2	21.904	0.631	0.298	0.079	0.089	0.035	0.557	0.901
3	26.310	0.756	0.298	0.109	0.073	0.015	0.803	1.150
4	31.683	0.907	0.291	0.286	0.078	0.073	1.018	1.427
5	38.239	1.090	0.411	0.109	0.159	0.099	0.696	1.374
6	47.683	1.355	0.462	0.119	0.317	0.114	0.659	1.616
7	65.459	1.858	0.515	0.312	0.623	0.122	0.679	2.163

Endcap-Endcap Full Topology

Bin	Ave Mass	Energy	Tracking	Mass Shift	M.L.	UE Syst.	Tune Syst.	Total
1	18.500	0.641	0.178	0.141	0.161	0.173	0.500	0.877
2	21.700	0.757	0.117	0.149	0.128	0.048	0.897	1.197
3	26.314	0.909	0.210	0.151	0.107	0.058	0.860	1.284
4	31.736	1.096	0.248	0.204	0.084	0.077	1.307	1.739
5	38.878	1.314	0.358	0.390	0.091	0.091	0.519	1.514

Table 6.10: Dijet invariant mass systematics.

East Barrel-Endcap

Bin	Ave Mass	Energy	Tracking	Mass Shift	M.L.	UE Syst.	Tune Syst.	Total
1	18.440	0.531	0.275	0.397	0.159	0.216	1.150	1.382
2	22.110	0.637	0.258	0.139	0.140	0.040	0.683	0.990
3	26.575	0.765	0.318	0.168	0.098	0.046	0.785	1.159
4	32.214	0.924	0.282	0.110	0.081	0.029	1.203	1.549
5	38.351	1.094	0.431	0.144	0.144	0.085	0.720	1.396
6	48.012	1.365	0.471	0.145	0.262	0.106	0.723	1.646
7	65.727	1.864	0.541	0.337	0.509	0.126	0.694	2.153

West Barrel-Endcap

Bin	Ave Mass	Energy	Tracking	Mass Shift	M.L.	UE Syst.	Tune Syst.	Total
1	18.511	0.533	0.225	0.109	0.116	0.154	1.025	1.198
2	21.782	0.627	0.330	0.093	0.078	0.080	0.908	1.161
3	26.022	0.747	0.258	0.135	0.083	0.016	0.874	1.189
4	30.793	0.879	0.299	0.722	0.097	0.077	0.684	1.366
5	37.955	1.080	0.347	0.118	0.207	0.077	0.642	1.327
6	46.427	1.318	0.379	0.162	0.553	0.118	0.407	1.547
7	62.824	1.795	0.207	0.665	2.520	0.009	0.556	3.220

Table 6.11: Dijet invariant mass systematic.

Barrel-Endcap Full Topology

Bin	Ave Mass	Trans Residual	UE	Trigger and Reco.	Total
1	18.499	0.00028	0.00025	0.00050	0.00063
2	21.904	0.00028	0.00054	0.00039	0.00072
3	26.310	0.00028	0.00089	0.00039	0.00101
4	31.683	0.00032	0.00034	0.00063	0.00078
5	38.239	0.00064	0.00059	0.00087	0.00123
6	47.683	0.00126	0.00127	0.00107	0.00208
7	65.459	0.00243	0.00153	0.00569	0.00637

Endcap-Endcap Full Topology

Bin	Ave Mass	Trans Residual	UE	Trigger and Reco.	Total
1	18.500	0.00028	0.00186	0.00077	0.00203
2	21.700	0.00028	0.00221	0.00094	0.00242
3	26.314	0.00028	0.00061	0.00145	0.00160
4	31.736	0.00028	0.00444	0.00311	0.00543
5	38.878	0.00042	0.00444	0.00519	0.00684

Table 6.12: Dijet A_{LL} systematics.

East Barrel-Endcap

Bin	Ave Mass	Trans Residual	UE	Trigger and Reco.	Total
1	18.440	0.00028	0.00068	0.00062	0.00096
2	22.110	0.00028	0.00141	0.00043	0.00150
3	26.575	0.00028	0.00157	0.00038	0.00164
4	32.214	0.00033	0.00103	0.00075	0.00132
5	38.351	0.00065	0.00131	0.00096	0.00175
6	48.012	0.00128	0.00219	0.00104	0.00274
7	65.727	0.00244	0.00219	0.00598	0.00682

West Barrel-Endcap

Bin	Ave Mass	Trans Residual	UE	Trigger and Reco.	Total
1	18.511	0.00028	0.00101	0.00059	0.00120
2	21.782	0.00028	0.00138	0.00048	0.00149
3	26.022	0.00028	0.00049	0.00045	0.00072
4	30.793	0.00031	0.00113	0.00086	0.00145
5	37.955	0.00062	0.00094	0.00149	0.00187
6	46.427	0.00118	0.00213	0.00260	0.00356
7	62.824	0.00225	0.00213	0.00556	0.00636

Table 6.13: Dijet A_{LL} systematics.

6.7 Final Results

The advantage of a correlation observable at forward pseudorapidity range is its ability to constrain and probe lower initial state kinematics. A_{LL} is presented for several different topologies: Barrel-Endcap dijets, which have one of the jets in the BEMC and the other in the EEMC; East Barrel-Endcap dijets, with the Barrel jet at negative pseudorapidity while the West Barrel-Endcap dijets involve a Barrel jet at positive pseudorapidity; and Endcap-Endcap dijets, in which both jets are emitted at forward rapidity. Events from the specific topologies arise from asymmetric partonic collisions, and are preferentially between a high momentum (high x and therefore highly polarized) quark and a low momentum gluon. The control over initial kinematics achievable with dijets can be seen in Fig. 6.15, which presents the partonic momentum fraction distributions (weighted by partonic $\hat{a}_{LL}$) of the gluons as obtained from PYTHIA for a sample of detector level dijets with $16.0 < M < 19.0 \text{ GeV/c}^2$. The asymmetric nature of the collisions can be seen in the separation of the high- and low-x distributions, and the increased reach to lower x shows the advantage of this measurement.

Values of A_{LL} extracted from the data represent an admixture of the asymmetries produced from the three dominant partonic scattering sub-processes: qq, qg, and gg. The STAR trigger is more efficient for certain sub-processes, altering the sub-process fractions in the data set and thereby shifting the measured A_{LL}. Further distortions can arise due to systematic shifts caused by the finite resolution of the detector coupled with a rapidly falling invariant mass distribution. Corrections were applied to the raw A_{LL} values to compensate for these effects, as discussed in detail in the previous chapter.

Tables 6.14 and 6.15 show the final values measured for A_{LL} in this work for Barrel-Endcap, East Barrel-Endcap, West Barrel-Endcap, and Endcap-Endcap dijet topologies. Total error estimates for both M and A_{LL} are also listed. Figs. 6.16 show the forward dijet A_{LL} values as a function of dijet invariant mass, which has been corrected back to the parton level. The heights of the uncertainty boxes represent the total systematic error due to trigger and reconstruction bias, combined with the error due to residual transverse polarization components in the beams as well as the systematic

Barrel-Endcap Full Topology

Bin	Mass	A_{LL}
1	18.499 ± 1.077	-0.00573 ± 0.00418 ± 0.00063
2	21.904 ± 0.901	0.01018 ± 0.00285 ± 0.00072
3	26.310 ± 1.150	0.00349 ± 0.00279 ± 0.00101
4	31.683 ± 1.427	0.00315 ± 0.00349 ± 0.00078
5	38.239 ± 1.374	0.00006 ± 0.00513 ± 0.00123
6	47.683 ± 1.616	0.00986 ± 0.00750 ± 0.00208
7	65.459 ± 2.163	0.01384 ± 0.02805 ± 0.00637

Endcap-Endcap

Bin	Mass	A_{LL}
1	18.500 ± 0.877	0.00189 ± 0.00694 ± 0.00203
2	21.700 ± 1.197	-0.00691 ± 0.00690 ± 0.00242
3	26.314 ± 1.284	0.02119 ± 0.00990 ± 0.00160
4	31.736 ± 1.739	0.04254 ± 0.01901 ± 0.00543
5	38.878 ± 1.514	0.07787 ± 0.04583 ± 0.00684

Table 6.14: Dijet A_{LL}: full topology.

EastBarrel-Endcap

Bin	Mass	A_{LL}
1	18.440 ± 1.382	-0.01783 ± 0.01058 ± 0.00096
2	22.110 ± 0.990	0.00579 ± 0.00468 ± 0.00150
3	26.575 ± 1.159	0.00485 ± 0.00388 ± 0.00164
4	32.214 ± 1.549	0.00166 ± 0.00443 ± 0.00132
5	38.351 ± 1.396	-0.00782 ± 0.00609 ± 0.00175
6	48.012 ± 1.646	0.00991 ± 0.00844 ± 0.00274
7	65.727 ± 2.153	0.01198 ± 0.02963 ± 0.00682

WestBarrel-Endcap

Bin	Mass	A_{LL}
1	18.511 ± 1.198	-0.00337 ± 0.00455 ± 0.00120
2	21.782 ± 1.161	0.01307 ± 0.00359 ± 0.00149
3	26.022 ± 1.189	0.00273 ± 0.00401 ± 0.00072
4	30.793 ± 1.366	0.00660 ± 0.00566 ± 0.00145
5	37.955 ± 1.327	0.02087 ± 0.00951 ± 0.00187
6	46.427 ± 1.547	0.01133 ± 0.01632 ± 0.00356
7	62.824 ± 3.220	0.03136 ± 0.08705 ± 0.00636

Table 6.15: Dijet A_{LL}: Barrel-Endcap different topologies.
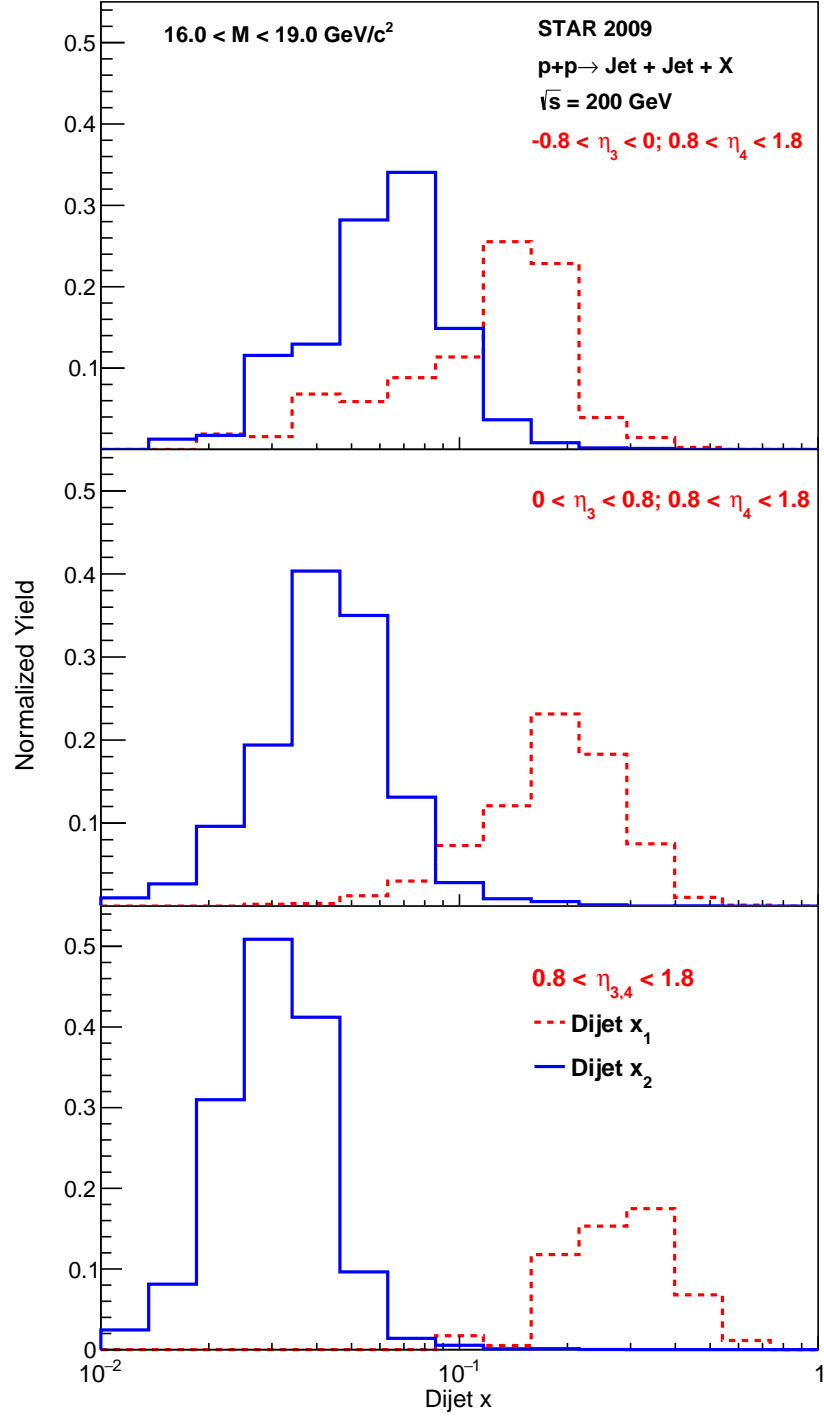
Figure 6.15: *pp* 200 GeV Dijet kinematics for different dijet topologies with the lowest dijet invariant mass bin $16.0 - 19.0$ GeV/c^2. x_1 is always associated with the parton moving initially toward the Endcap.

errors from underlying events. The relative luminosity uncertainty results in a scaling uncertainty that is common to all points, and is represented by the gray band on the horizontal axis. The widths of the uncertainty boxes represent the systematic error associated with the corrected dijet mass values and, in addition to contributions from the uncertainty on the correction to the parton level, include the uncertainties on calorimeter tower gains and efficiencies, as well as TPC momentum resolution and tracking efficiencies. Further uncertainties were added in quadrature to account for the PYTHIA tune variations and underlying events contributions.

The dijet x_1 and x_2 kinematic distributions shown in Fig. 6.15 are matched with the four dijet double-spin asymmetry A_{LL} distributions in Fig. 6.16. Compared to the kinematic distributions for the dijet measurement at Barrel-Barrel mid-rapidity [8], it is clear that extending the measurement into the Endcap region probes lower x values, and results in a much cleaner separation between x_1 and x_2, especially for the Endcap-Endcap topology.
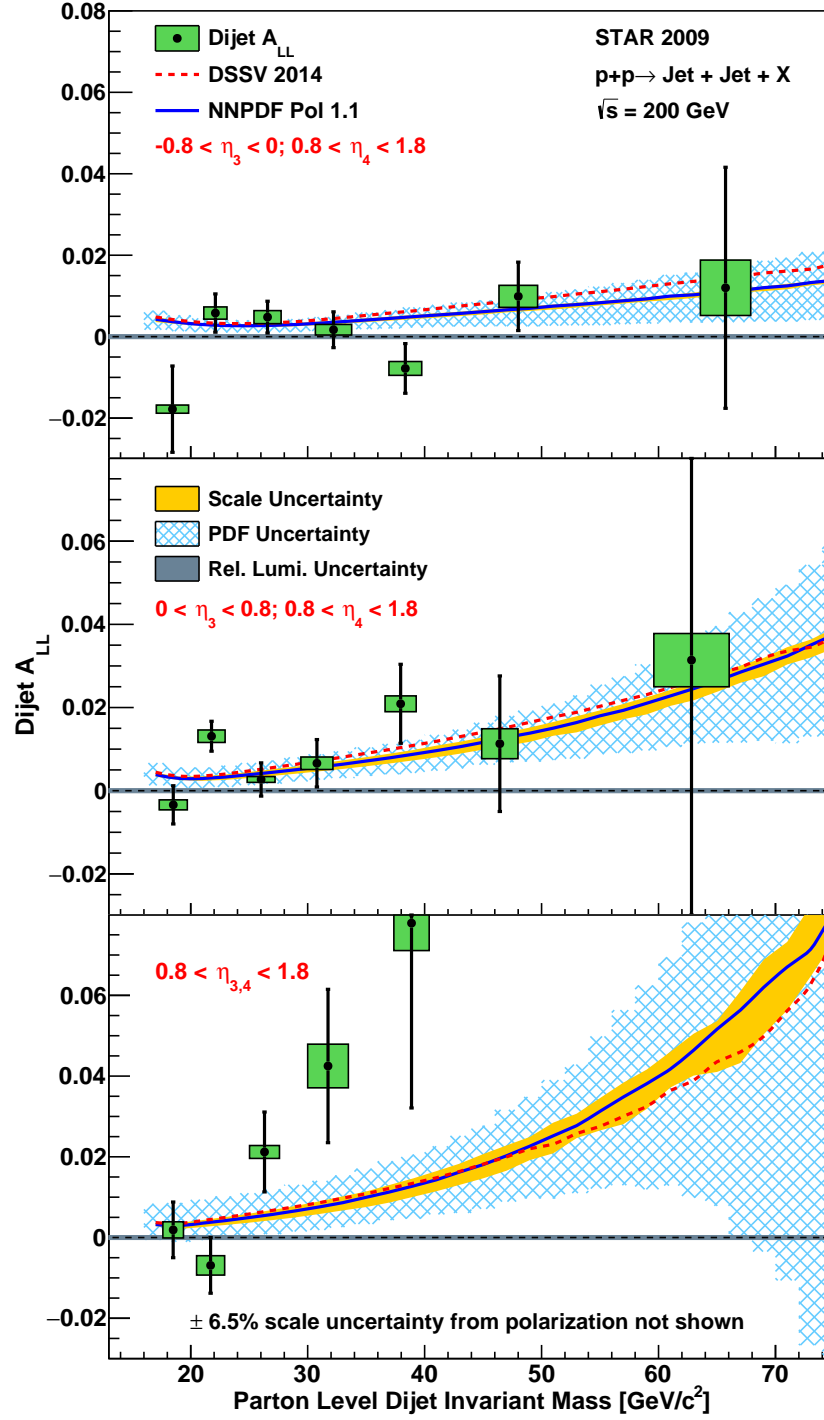
Figure 6.16: Dijet A_{LL} vs. parton-level invariant mass for different topologies.

6.8 Comparison to Theory

The asymmetry results extracted from data in this work are compared to two different theoretical predictions, both derived from global fits to previous polarized DIS and RHIC data. Theoretical A_{LL} values were obtained from the dijet production code of deFlorian *et al.* [19], using the DSSV2014 [20] and NNPDFpol1.1 [28] polarized PDF sets as input. The unpolarized PDF sets used in the denominator of the asymmetry were MRST2008 [27] and NNPDF2.3 [11], respectively. Uncertainty bands representing the sensitivity to factorization and renormalization scale (solid, yellow) and polarized PDF uncertainty (hatched, blue) were generated for the NNPDF results.

In order to get a quantitative comparison to the theoretical prediction, a χ^2 test between the data and theory was calculated based on the discussion in [32]. The expression for the χ^2 is:

$$\chi^2 = \sum_{i=1}^{N} \left(\frac{m_i - t_i - \beta_{1i}r_1 - \beta_{2i}r_2}{\sigma_i}\right)^2 + r_1^2 + r_2^2, \tag{6.13}$$

where $\{m_i\}$ is a set of measurements from data (measured A_{LL}), t_i is the true value (theoretical A_{LL} value of the ith measured quantity) and σ_i is the uncorrelated error of the measurement (quadrature sum of the statistical and uncorrelated systematic errors on A_{LL}).

In this calculation, there are two correlated systematic errors. One is associated with the relative luminosity ($\beta_1 = 0.0005$ in this measurement) and the other is associated with the jet energy scale. The error associated with the jet energy scale is $\beta_2 = \frac{\partial A_{LL}}{\partial M} \times \delta M$; the differential factor is from a 3rd order polynomial fit of the theory curve (similar to what has been done when calculating the trigger and reconstruction bias), and δM is the systematic error on the dijet invariant mass. r_1 and r_2 are the corresponding free parameters associated with these two correlated errors. Optimizing the χ^2 relative to r_1 and r_2, the expression for the χ^2 is (a detailed derivation can be found in appendix B):

$$\chi^2 = \sum_{i=1}^{N} \left(\frac{m_i - t_i}{\sigma_i}\right)^2 - (A^{-1})_{11}B_1^2 - (A^{-1})_{22}B_2^2 - 2(A^{-1})_{12}B_1B_2, \tag{6.14}$$

where B_j is a 2×1 matrix:

$$B = \begin{bmatrix} \sum_{i=1}^{N} \frac{\beta_{1i}(m_i - t_i)}{\sigma_i^2} \\ \sum_{i=1}^{N} \frac{\beta_{2i}(m_i - t_i)}{\sigma_i^2} \end{bmatrix}, \tag{6.15}$$

and $A_{jj'}$ is a 2×2 symmetric matrix:

$$A = \begin{bmatrix} 1 + \sum_{i=1}^{N} (\frac{\beta_{1i}}{\sigma_i})^2 & \sum_{i=1}^{N} (\frac{\beta_{1i} * \beta_{2i}}{\sigma_i^2}) \\ \sum_{i=1}^{N} (\frac{\beta_{1i} * \beta_{2i}}{\sigma_i^2}) & 1 + \sum_{i=1}^{N} (\frac{\beta_{2i}}{\sigma_i})^2 \end{bmatrix}. \tag{6.16}$$

Combining all the values described in previous sections, the values for χ^2, r_1 and r_2 at different dijet topologies and for these theory models can be calculated separately. The final results are shown in tables 6.16 and 6.17:

	DSSV			
	Barrel-Endcap	Endcap-Endcap	East Barrel-Endcap	West Barrel-Endcap
χ^2/NDF	2.05	2.36	1.63	1.64
χ^2	12.32	9.46	9.80	9.63
r_1	-0.08	0.01	-0.23	0.09
r_2	-0.10	0.06	-0.15	0.04

Table 6.16: χ^2 and r_1, r_2 for data/theory comparison for the DSSV model.

	NNPDF			
	Barrel-Endcap	Endcap-Endcap	East Barrel-Endcap	West Barrel-Endcap
χ^2/NDF	1.98	2.42	1.48	1.71
χ^2	11.87	9.66	8.87	10.25
r_1	0.07	0.03	-0.15	0.19
r_2	-0.02	0.06	-0.10	0.08

Table 6.17: χ^2 and r_1, r_2 for data/theory comparison for the NNPDF model.

Overall, the data are seen to be in good agreement with current theoretical expectations. In all topologies, $\chi^2/NDF < 2.5$. This suggests that incorporating these results into global analyses may not change the value of $\Delta g(x)$ significantly, but should lead to reduced uncertainties on this quantity, especially at lower Bjorken-x.

Chapter 7

Conclusions and Outlook

The spin of the proton can be decompsed into contributions from the intrinsic quark spin, the orbital angular momentum, and the intrinsic gluon spin. From polarized deep inelastic scattering studies, we know that the quarks only contribute $\sim 30\%$ to the total spin of the proton. Measuring the polarization of the gluons inside the proton is a key observable to solve the 'spin crisis' problem, not only to understand proton structure in its own right, but also to serve as a tool for uncovering properties of the strong interaction in the non-perburbative regime. RHIC is the world's first and only accelerator capable of colliding polarized protons, and its kinematic regime is particularly sensitive to the gluon's interactions. Therefore polarized *pp* collisions at RHIC provide a unique opportunity to unravel the internal structure and the QCD dynamics of nucleons with unprecedented preciesion.

Previous data from RHIC have been added to the DSSV and NNPDF global analyses. Including the STAR 2009 inclusive jet A_{LL} results showed, for the first time, a nonzero gluon polarization in the region of sensitivity. However, at lower Bjorken x, the behavior and shape of the gluon helicity distribution is still poorly constrained. Compared to inclusive jet measurements, correlation measurements such as dijets capture more information from the hard scattering initial states, and may place better constrains on the functional form of the gluon helicity. Forward dijet measurements, which arise from asymmetric partonic collisions, extend the current dijet program at mid-rapidity

and probe lower momentum gluons.

To carry out these forward jet measurements, however, presented several experimental challenges. Machine learning methods have been a hot topic in recent yerars, and there are many important problems in high energy physics that can only be solved using machine learning methods. These vary from online data filtering and reconstruction to offline data analysis. Applying machine learning methods to solve the problems of limited tracking efficiency in the Endcap Electromagetic Calorimeter (EEMC) resulted in a significant improvement in the measurements. The results looks reasonable and promising.

In summary, the first forward region dijet longitudinal double-spin asymmetries from STAR pp collisions at $\sqrt{s} = 200$ GeV are reported. The measured dijet A_{LL} values in the forward region are presented for several different topologies based on the jet pesudorapidities. The A_{LL} results support the most recent DSSV and NNPDF predictions, which included the 2009 RHIC inclusive jet and pion data, and should help to reduce the uncertainties at the lower x regions in further global fits.

In 2015, STAR recorded 52 pb^{-1} of longitudinally polarized data at 200 GeV, which is about twice the statistics of 2009. Furthermore, in 2012 STAR recorded 82 pb^{-1} of longitudinally polarized data at $\sqrt{s} = 500$ GeV and in 2013, 300 pb^{-1} were collected under similar beam conditions. As shown in Fig. 7.1, at the higher collision energy of 500 GeV, the interacting partons will have much lower momentum fractions. This, combined with the increased statistics, should lead to higher precision dijet A_{LL} measurements from STAR that will help to better constrain the value and shape of $\Delta g(x)$ at low Bjorken-x.
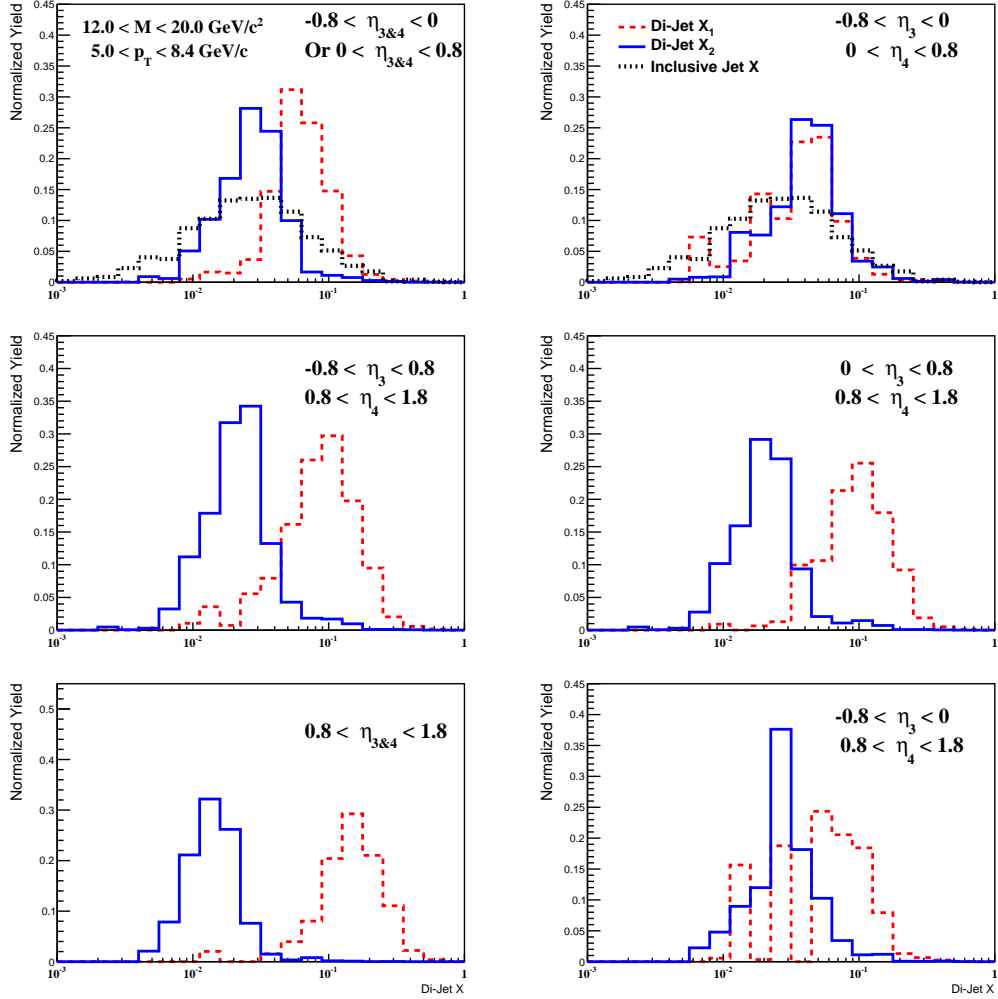
Figure 7.1: *pp* 500 GeV dijet kinematics for Barrel-Barrel same sign (upper left), Barrel-Barrel opposite sign (upper right) and inclusive jet (black line); Barrel-Endcap full topology (middle left), East Barrel-Endcap(middle right), West Barrel-Endcap (lower right) and Endcap-Endcap (lower left).

Appendix A

List of Runs and Fills

10120063 10120065 10120078 10120079 10120082 10120085 10120086 10120093 10120097
10120100 10121001 10121017 10121020 10121022 10121029 10121039 10121040 10121043
10121044 10122006 10122007 10122010 10122013 10122014 10122015 10122016 10122017
10122019 10122022 10122023 10122024 10122047 10122048 10122049 10122050 10122054
10122055 10122060 10122061 10122065 10122067 10122071 10122086 10122087 10122095
10122099 10123004 10123007 10123010 10123086 10123087 10123090 10124013 10124014
10124037 10124038 10124044 10124045 10124046 10124049 10124050 10124053 10124062
10124066 10124071 10124072 10124075 10124076 10124110 10124111 10124113 10125001
10125008 10125009 10125010 10125014 10125015 10125016 10125017 10125022 10125023
10125075 10125076 10125080 10125083 10125091 10126003 10126004 10126005 10126012
10126017 10126018 10126019 10126024 10126025 10126026 10126083 10126084 10126087
10126088 10126089 10126090 10127008 10127009 10127011 10128041 10128043 10128046
10128047 10128048 10128049 10128050 10128052 10128053 10128054 10128055 10128056
10128059 10128060 10128061 10128063 10128065 10128066 10128070 10128072 10128094
10128098 10128099 10128100 10128101 10128102 10129003 10129005 10129006 10129007
10129008 10129011 10129048 10129050 10130011 10130012 10130014 10130015 10131009
10131012 10131029 10131039 10131040 10131041 10131042 10131043 10131045 10131047

10131052 10131075 10131076 10134021 10134024 10134025 10134026 10134027 10134028

10134030 10134035 10134036 10134037 10134044 10134085 10134086 10134101 10134102

10134103 10135001 10135002 10135005 10135006 10135007 10135008 10135009 10135011

10135016 10135017 10135018 10135030 10135058 10135059 10135063 10135064 10135065

10135066 10135070 10135072 10135076 10135077 10135081 10135082 10135083 10136001

10136011 10136012 10136017 10136019 10136020 10136021 10136024 10136025 10136026

10136027 10136028 10136030 10136031 10136035 10136036 10136037 10136061 10136063

10136069 10136070 10136071 10136073 10136074 10136077 10136078 10136079 10136092

10136096 10136097 10136099 10136100 10137003 10137004 10137006 10137008 10137045

10137046 10137048 10137049 10137051 10137052 10137055 10137059 10137060 10137061

10137063 10137064 10137065 10137066 10137067 10138008 10138011 10138012 10138013

10138014 10138016 10138021 10138022 10138023 10138024 10138025 10138026 10138027

10138030 10138032 10138047 10138049 10138052 10138053 10138054 10138055 10138098

10138099 10138100 10139002 10139003 10139007 10139008 10139009 10139010 10139014

10139015 10139017 10139018 10139038 10139040 10139044 10139067 10139068 10139069

10139070 10139073 10139074 10139076 10139077 10139102 10139107 10140002 10140005

10140006 10140007 10140010 10140011 10141010 10141013 10141018 10141019 10141020

10141023 10141025 10141026 10141027 10141030 10141031 10141032 10142029 10142031

10142034 10142035 10142036 10142041 10142042 10142043 10142044 10142047 10142050

10142056 10142057 10142058 10142086 10142093 10142098 10143007 10143008 10143009

10143014 10143015 10143018 10143023 10143025 10143026 10143027 10143029 10143043

10143044 10143045 10143047 10143051 10143052 10143053 10143054 10143058 10143062

10143063 10143064 10143065 10143076 10143077 10143078 10143082 10143083 10143085

10143086 10143090 10143092 10143095 10143098 10143099 10143102 10143103 10143104

10143106 10144001 10144002 10144003 10144022 10144026 10144027 10144028 10144029

10144030 10144034 10144035 10144036 10144037 10144044 10144045 10144046 10144072

10144074 10144075 10144076 10144083 10144085 10144087 10144090 10144091 10144092

10144093 10144098 10145011 10145012 10145013 10145016 10145018 10145027 10145030

10145032 10145034 10145036 10145038 10145042 10145046 10145047 10145070 10145072

10145073 10145076 10145078 10145079 10145081 10145082 10146040 10146047 10146048

10146049 10146050 10146051 10146052 10146054 10146055 10146073 10146084 10146086

10146087 10146091 10148002 10148005 10148006 10148021 10148025 10148026 10148027

10148028 10148033 10148034 10148035 10149008 10149012 10149023 10149024 10149025

10149026 10149028 10149031 10149032 10149033 10149034 10149035 10149087 10150001

10150005 10150008 10150009 10150010 10150011 10150012 10150013 10150018 10150021

10150022 10150024 10150025 10150052 10150053 10150056 10150057 10151001 10151002

10151003 10151004 10151005 10151006 10151034 10151035 10151039 10151040 10151041

10151042 10151043 10151044 10151045 10151046 10151047 10152001 10152004 10152005

10152006 10152007 10152008 10152009 10152010 10154060 10154061 10154064 10154065

10154066 10154067 10154068 10154083 10155001 10155010 10155014 10155015 10155016

10155019 10155020 10155022 10155095 10155097 10156004 10156007 10156008 10156009

10156011 10156013 10156031 10156034 10156037 10156038 10156039 10156040 10156058

10156086 10156087 10156090 10156092 10156093 10156095 10156096 10157001 10157004

10157005 10157015 10157016 10157019 10157020 10157021 10157022 10157023 10157027

10157051 10157052 10157056 10157057 10157058 10158001 10158004 10158010 10158013

10158014 10158015 10158016 10158017 10158018 10158021 10158042 10158043 10158047

10158048 10158049 10158050 10158051 10158054 10158055 10158074 10158075 10158076

10158079 10158080 10158082 10158083 10158086 10158087 10158089 10158090 10159006

10159039 10159040 10159044 10159045 10159046 10159048 10159049 10160005 10160006

10160009 10160010 10160011 10160012 10160013 10160014 10160016 10160017 10160071

10160072 10160075 10160077 10160078 10160079 10160081 10160084 10161005 10161006

10161010 10161011 10161014 10161015 10161016 10161019 10161020 10161021 10161025

10161026 10161027 10161030 10162006 10162007 10162010 10162024 10162025 10162029

10162030 10162031 10162032 10162033 10162034 10162035 10162036 10162037 10162038

10162040 10163048 10163051 10163052 10163053 10163054 10163055 10163056 10163059

10164002 10164009 10164010 10164011 10164013 10164016 10164017 10164018 10164025

10164026 10164029 10164030 10164031 10164034 10164057 10164060 10164061 10164062

10164067 10164078 10164079 10164082 10165007 10165008 10165015 10165016 10165017

10165018 10165019 10165022 10165023 10165024 10165027 10166061 10166067 10167007

10167008 10167009 10167012 10167013 10167014 10167015 10167016 10167017 10167020

10167048 10167049 10167050 10167053 10167054 10167056 10167057 10167058 10167059

10169005 10169006 10169009 10169010 10169012 10169013 10169014 10169021 10169030

10169031 10169032 10169033 10169041 10169042 10169043 10169044 10169047 10169048

10169049 10169065 10169070 10169074 10169075 10169076 10169077 10169078 10169080

10170003 10170011 10170012 10170013 10170016 10170017 10170018 10170019 10170023

10170024 10170025 10170026 10170029 10170045 10170046 10170047 10170050 10170052

10170053 10170054 10170060 10170061 10170064 10170065 10170075 10170078 10170081

10170089 10171011 10171014 10171015 10171016 10171019 10171021 10171022 10171025

10171034 10171036 10171037 10171041 10171042 10171043 10171044 10171045 10171048

10171060 10171061 10171069 10171070 10171071 10171078 10172001 10172002 10172003

10172007 10172060 10172061 10172064 10172077 10172079 10172082 10172083 10172085

10172089 10172090 10172094 10173007 10173008 10173009 10173012 10173013 10173015

10173016 10173017 10173031 10173032 10173033 10173039 10173048 10173051 10173053

10173055 10174012 10174013 10174016 10174023 10174025 10174026 10174027 10174028

10174031 10174044 10174045 10174048 10174049 10174050 10174051 10174052 10174094

10175005 10175008 10175009 10175010 10175011 10175012 10175013 10175014 10175019

10175038 10176001 10176008 10176016 10176017 10176018 10176020 10176022 10176025

10176028 10177055 10177056 10177057 10177060 10177061 10178022 10178023 10178026

10178029 10178036 10179005 10179006 10179007 10179008 10179009 10179010 10179018

10179019 10179022 10179031 10179032 10179033 10179042 10179043 10179044 10179045

10179085 10179086 10179088 10179096 10179097 10179098 10180003 10180004 10180007

10180021 10180022 10180027 10180028 10180029 10180030

List of Fills:

10682 10704 10756 10786 10855 10889 10953 10971 10683 10706 10758 10789 10866 10890 10954 10973 10684 10708 10761 10790 10869 10904 10955 10986 10685 10712 10763 10791 10870 10919 10959 10987 10688 10713 10773 10800 10875 10920 10960 11001 10689 10729 10777 10806 10876 10921 10961 11002 10690 10746 10781 10814 10877 10932 10963 11003 10695 10748 10782 10820 10878 10935 10964 11005 10696 10753 10783 10825 10880 10937 10967 11006 10700 10754 10784 10826 10881 10951 10968 10703 10755 10785 10854 10884 10952 10970 10717 10730 10764 10813 10924 10957 10720 10749 10765 10864 10925 10998 10727 10759 10778 10902 10956

Appendix B

Some Derivations

B.1 Di-jet Kinematics Derivation

B.1.1 Di-jet Invariant Mass

We start with the 4-momentum vector:

$$P = \begin{bmatrix} E \\ p_x \\ p_y \\ p_z \end{bmatrix}, \qquad (B.1)$$

If we define $y = \frac{1}{2} \ln\left(\frac{E+p_z}{E-p_z}\right)$ (pseudorapidity), and $p_T = \sqrt{p_x^2 + p_y^2}$ with ϕ as the relative angle, then $p_x = p_T \cos\phi$ and $p_y = p_T \sin\phi$. We see that:

$$y = \frac{1}{2} \ln\left(\frac{E+p_z}{E-p_z}\right) = \ln\left(\sqrt{\frac{E+p_z}{E-p_z}}\right) = \ln\left(\frac{E+p_z}{\sqrt{E^2-p_z^2}}\right) = \ln\left(\frac{E+p_z}{m_T^2}\right) \tag{B.2a}$$

$$-y = -\frac{1}{2} \ln\left(\frac{E+p_z}{E-p_z}\right) = \ln\left(\sqrt{\frac{E-p_z}{E+p_z}}\right) = \ln\left(\frac{E-p_z}{\sqrt{E^2-p_z^2}}\right) = \ln\left(\frac{E-p_z}{m_T^2}\right), \tag{B.2b}$$

where $m_T = \sqrt{m^2 + p_x^2 + p_y^2}$ is the transverse mass. Then the energy and z component of momentum can be written as: $E = m_T \cosh y$ and $p_z = m_T \sinh y$.

The di-jet invariant mass is $M = \sqrt{(P_3 + P_4)^2}$, where P_3 and P_4 are the 4-momenta of two outgoing partons. We can express the individual 4-momenta as:

$$P_3 = \begin{bmatrix} m_T \cosh y_3 \\ p_T \cos\phi_3 \\ p_{T,3} \sin\phi_3 \\ m_{T,3} \sinh y_3 \end{bmatrix}, P_4 = \begin{bmatrix} m_T \cosh y_4 \\ p_T \cos\phi_4 \\ p_{T,4} \sin\phi_4 \\ m_{T,4} \sinh y_4 \end{bmatrix} \tag{B.3}$$

$$M = \sqrt{(P_3^2 + P_4^2 + 2P_3 * P_4)^2}, \tag{B.4}$$

where $P^2 = m^2$, and the cross term is:

$$P_3 * P_4 = m_{T,3} m_{T,4}(\cosh y_3 \cosh y_4 - \sinh y_3 \sinh y_4) - p_{T,3} p_{T,4}(\cos\phi_3 \cos\phi_4 + \sin\phi_3 \sin\phi_4)$$

$$= \sqrt{m_3^2 + p_{T3}^2}\sqrt{m_4^2 + p_{T4}^2}\cosh(y_3 - y_4) - 2p_{T3}p_{T4}\cos(\phi_3 - \phi_4). \tag{B.5}$$

Then the di-jet invariant mass is:

$$M = \sqrt{m_3^2 + m_4^2 + 2\sqrt{m_3^2 + p_{T3}^2}\sqrt{m_4^2 + p_{T4}^2}cosh(y_3 - y_4) - 2p_{T3}p_{T4}cos(\phi_3 - \phi_4)}. \qquad \text{(B.6)}$$

B.1.2 Scattering Kinematic Approximations

For simplicity, we assume that partons are massless and only move in the z-direction. Then the initial 4-momenta can be written as:

$$P_1 = \frac{\sqrt{s}}{2}\begin{bmatrix} x_1 \\ 0 \\ 0 \\ x_1 \end{bmatrix}, \qquad P_2 = \frac{\sqrt{s}}{2}\begin{bmatrix} x_2 \\ 0 \\ 0 \\ x_2 \end{bmatrix}. \qquad \text{(B.7)}$$

Define the initial state 4-momentum as $q = P_1 + P_2$, the invariant M would be:

$$M = \sqrt{q^2} = \sqrt{sx_1x_2}. \qquad \text{(B.8)}$$

The pesudorapidity can be defined using the momentum fractions:

$$\cosh y = \frac{E}{\sqrt{E^2 - p_z^2}} = \frac{1}{2}\frac{x_1 + x_2}{\sqrt{x_1x_2}} \qquad \text{(B.9a)}$$

$$\sinh y = \frac{p_z}{\sqrt{E^2 - p_z^2}} = \frac{1}{2}\frac{x_1 - x_2}{\sqrt{x_1x_2}}. \qquad \text{(B.9b)}$$

Then the pesudorapidity of the momentum q is:

$$y = \frac{1}{2}\ln\left(\frac{E - p_z}{E + p_z}\right) = \frac{1}{2}\ln\left(\frac{x_1}{x_2}\right). \qquad \text{(B.10)}$$

The Lorentz transformation is given by:

$$
\Lambda(y) =
\begin{bmatrix}
\cosh y & 0 & 0 & \sinh y \\
0 & 1 & 0 & 0 \\
0 & 0 & 1 & 0 \\
\sinh y & 0 & 0 & \cosh y
\end{bmatrix}
=
\frac{1}{2\sqrt{x_1 x_2}}
\begin{bmatrix}
x_1 + x_2 & 0 & 0 & x_1 - x_2 \\
0 & 1 & 0 & 0 \\
0 & 0 & 1 & 0 \\
x_1 - x_2 & 0 & 0 & x_1 + x_2
\end{bmatrix}.
\tag{B.11}
$$

In the center of mass frame, the outgoing partons can be written as:

$$
P_3^* = p_T
\begin{bmatrix}
\cosh y^* \\
\cos \phi \\
\sin \phi \\
\sinh y^*
\end{bmatrix},
\quad
P_4^* = p_T
\begin{bmatrix}
\cosh y^* \\
- \cos \phi \\
- \sin \phi \\
- \sinh y^*
\end{bmatrix}.
\tag{B.12}
$$

In the lab frame, using the Lorentz Transformation, we get:

$$
P_3 = \Lambda(y) P_3^* = p_T
\begin{bmatrix}
\cosh y & 0 & 0 & \sinh y \\
0 & 1 & 0 & 0 \\
0 & 0 & 1 & 0 \\
\sinh y & 0 & 0 & \cosh y
\end{bmatrix}
\begin{bmatrix}
\cosh y^* \\
\cos \phi \\
\sin \phi \\
\sinh y^*
\end{bmatrix}
= p_T
\begin{bmatrix}
\cosh(y + y^*) \\
\cos \phi \\
\sin \phi \\
\sinh(y + y^*)
\end{bmatrix}.
$$

$$
P_4 = \Lambda(y) P_4^* = p_T
\begin{bmatrix}
\cosh y & 0 & 0 & \sinh y \\
0 & 1 & 0 & 0 \\
0 & 0 & 1 & 0 \\
\sinh y & 0 & 0 & \cosh y
\end{bmatrix}
\begin{bmatrix}
\cosh y^* \\
- \cos \phi \\
- \sin \phi \\
- \sinh y^*
\end{bmatrix}
= p_T
\begin{bmatrix}
\cosh(y - y^*) \\
- \cos \phi \\
- \sin \phi \\
\sinh(y - y^*)
\end{bmatrix}.
\tag{B.13}
$$

In the lab frame, we can define the outgoing partons as:

$$
P_3 = p_T \begin{bmatrix} \cosh y_3 \\ \cos \phi_3 \\ \sin \phi_3 \\ \sinh y_3 \end{bmatrix}, \quad P_4 = p_T \begin{bmatrix} \cosh y_4 \\ \cos \phi_4 \\ \sin \phi_4 \\ \sinh y_4 \end{bmatrix}. \tag{B.14}
$$

Then $y_3 = y + y^*$ and $y_4 = y - y^*$, where $y = \frac{y_3 + y_4}{2}$ and $y^* = \frac{y_3 - y_4}{2}$. The invariant mass is $M = 2p_T \cosh y^*$ using the center-of-mass frame $P_3^* + P_4^*$. Using equation B.10, we can rewrite the expression:

$$
\begin{aligned}
x_1 &= \sqrt{x_1 x_2} e^y = \frac{M}{\sqrt{s}} e^y = \frac{p_T}{\sqrt{s}} 2 \cosh y^* e^y = \frac{p_T}{\sqrt{s}} (e^{y_3} + e^{y_4}) \\
x_2 &= \sqrt{x_1 x_2} e^{-y} = \frac{p_T}{\sqrt{s}} (e^{-y_3} + e^{-y_4}).
\end{aligned} \tag{B.15}
$$

The center-of-mass frame scattering angle can be expressed in terms of the pseudorapidity:

$$
\cos \theta^* = \frac{\sinh y^*}{\sqrt{\cos^2 \phi + \sin^2 \phi + \sinh^2 y^*}} = \tanh y^* = \tanh \left(\frac{y_3 - y_4}{2} \right). \tag{B.16}
$$

B.2 A_{LL} Derivation

In this section, details of the derivation of expressions for A_{LL} and δA_{LL} will be shown. This calculation is based on Brian Page's thesis.

B.2.1 Double Spin Asymmetry, A_{LL}

The final A_{LL} values are the combination of different measurements from each run. For a single fill, A_{LL} can be expressed as:

$$
A_{LL} = \frac{1}{P_B P_Y} \frac{(N^{++} + N^{--}) - R(N^{+-} + N^{-+})}{(N^{++} + N^{--}) + R(N^{+-} + N^{-+})}, \tag{B.17}
$$

where P_B and P_Y are the polarizations of the beams, and R is the relative luminosity, while the N^{++} and N^{+-} are the spin-sorted yields. To simply the calculation, we can use the single-spin asymmetry with fewer terms:

$$A_i = \frac{1}{P_i} \frac{N_i^+ - R_i N_i^-}{N_i^+ + R_i N^-}. \tag{B.18}$$

The associated uncertainty for A_i can then be expressed as:

$$\sigma_i^2 = (\frac{\partial A_i}{\partial N_i^+} \sigma_{N_i^+})^2 + (\frac{\partial A_i}{\partial N_i^-} \sigma_{N_i^-})^2 + (\frac{\partial A_i}{\partial P_i} \sigma_{P_i})^2 + (\frac{\partial A_i}{\partial R_i} \sigma_{R_i})^2$$

$$= \frac{1}{P_i^2 (N_i^+ + R_i N^-)^2} [(1 - P_i A_i)^2 \sigma_{N_i^+}^2 + (1 + P_i A_i)^2 R_i^2 \sigma_{N_i^-}^2 + (1 + P_i A_i)^2 (N^-)^2 \sigma_{R_i}^2] + \frac{A_i^2}{P_i^2} \sigma_{P_i}^2. \tag{B.19}$$

To get the best value of the asymmetry ($\bar{A}$), the maximum likelihood method is used to minimize the function:

$$\chi^2 = \sum_{i=1}^{N} (\frac{A_i - \bar{A}}{\sigma_i})^2. \tag{B.20}$$

Then we can get:

$$2\chi \frac{\partial \chi}{\partial x_i} = \sum_{i=1}^{N} 2(\frac{A_i - \bar{A}}{\sigma_i})(\frac{1}{\sigma_i}) = 0$$

$$\sum_{i=1}^{N} \frac{A_i}{\sigma_i^2} = \sum_{i=1}^{N} \frac{\bar{A}}{\sigma_i^2} \tag{B.21}$$

$$\bar{A} = \frac{\sum_i^N (A_i / \sigma_i^2)}{\sum_i^N (1 / \sigma_i^2)}.$$

To get the final expression, we need to calculate and simplify the σ_i. The scale uncertainty from polarization is about 6.5%, $A_i \sim 10^{-2}$, $P_i \sim 50\%$, $(\sigma_{N_i})^2 = N$, $R_i \sim 1$ and $\sigma_{R_i} \sim 0$. With these assumptions, we can ignore the last two terms, and the uncertainty can be approximated as:

$$\sigma_i^2 \approx \frac{1}{P_i^2 (N_i^+ + R_i N^-)}. \tag{B.22}$$

Then the $\bar{A}$ is:

$$\bar{A} = \frac{\sum_{i=1}^{N} P_i (N_i^+ - R_i N^-)}{\sum_{i=1}^{N} P_i^2 (N_i^+ + R_i N^-)}. \tag{B.23}$$

Replacing the polarization and spin state yields, the final double spin asymmetry A_{LL} can be expressed as:

$$A_{LL} = \frac{\sum_{i=1}^{N} P_{B,i} P_{Y,i} [(N_i^{++} + N_i^{--}) - R_{3,i}(N_i^{+-} + N_i^{-+})]}{\sum_{i=1}^{N} P_{B,i}^2 P_{Y,i}^2 [(N_i^{++} + N_i^{--}) + R_{3,i}(N_i^{+-} + N_i^{-+})]}. \tag{B.24}$$

B.2.2 A_{LL} Uncertainty

Similar to what has been calculated before, the uncertainty in $\bar{A}$ can be expressed as:

$$\sigma_{\bar{A}}^2 = \sum_{i=1}^{N} [(\frac{\partial \bar{A}}{\partial N_i^+} \sigma_{N_i^+})^2 + (\frac{\partial \bar{A}}{\partial N_i^-} \sigma_{N_i^-})^2 + (\frac{\partial \bar{A}}{\partial P_i} \sigma_{P_i})^2 + (\frac{\partial \bar{A}}{\partial R_i} \sigma_{R_i})^2]. \tag{B.25}$$

We still ignore the last two terms here, and the differential can be written as:

$$\frac{\partial \bar{A}}{\partial N_j^+} = \frac{P_j}{\sum_{i=1}^{N} P_i^2 (N_i^+ + R_i N^-)} (1 - P_j \bar{A}) \tag{B.26}$$

$$\frac{\partial \bar{A}}{\partial N_j^-} = \frac{-P_j R_j}{\sum_{i=1}^{N} P_i^2 (N_i^- + R_i N^-)} (1 + P_j \bar{A}). \tag{B.27}$$

Then the uncertainty is:

$$\sigma_{\bar{A}}^2 = \frac{\sum_{i=1}^{N} P_i^2 [(1 - P_i \bar{A})^2 N_i^+ + (1 + P_i \bar{A})^2 R_i^2 N_i^-]}{(\sum_{i=1}^{N} P_i^2 (N_i^+ + R_i N^-))^2} \tag{B.28}$$

. $\bar{A} \sim 10^{-2}$ is small and can be neglected in the expression. Then the final expression is:

$$\sigma_{\bar{A}}^2 = \frac{\sum_{i=1}^{N} P_i^2 (N_i^+ + R_i^2 N_i^-)}{[\sum_{i=1}^{N} P_i^2 (N_i^+ + R_i N^-)]^2}. \tag{B.29}$$

Placing the proper beam polarization, relative luminosity, and yield factors into the equation, then the statistical uncertainty of A_{LL} is:

$$\delta A_{LL} = \frac{\sqrt{\sum_{i=1}^{N} P_{B,i}^2 P_{Y,i}^2 [(N_i^{++} + N_i^{--}) + R_{3,i}^2(N_i^{+-} + N_i^{-+})]}}{\sum_{i=1}^{N} P_{B,i}^2 P_{Y,i}^2 [(N_i^{++} + N_i^{--}) + R_{3,i}(N_i^{+-} + N_i^{-+})]}. \tag{B.30}$$

The statistical error is approximately equal to $\delta A_{LL} \approx \frac{1}{P_B P_Y} \frac{1}{\sqrt{N}}$, where $P_{Y,B}$ are the average beam polarizations for blue and yellow beams, and N is the total yield, summed over all spin states.

B.3 χ^2 Derivation

In this section I will show the derivation of the χ^2 analysis. The calculation is based on [32] appendix B. The purpose of this calculation is to derive the appropriate expression of the χ^2 for data with correlated systematic errors. The defining condition is that χ^2 should obey a chi-squared distribution, and it is:

$$\chi^2 = \sum_{i=1}^{N} \left(\frac{m_i - t_i - \sum_j \beta_{ji} r_j}{\sigma_i}\right)^2 + \sum_{j=1}^{K} r_j^2, \tag{B.31}$$

where $\{m_i\}$ is a set of measurements, and $i = 1, 2, 3, ..., N$. t_i is the true value (theoretical value of the ith measured quantity). σ_i is the uncorrelated error of measurement. And there are K correlated errors denoted as $\beta_{1i}, \beta_{2i}, ..., \beta_{Ki}$.

χ^2 is a function of $r_1, ..., r_K$, and these variables could be used as fitting parameters to account for the systematic errors: minimizing χ^2 with respect to r_j can provide the best model to correct for the systematic error.

We can rewrite the expression to be:

$$\chi^2 = \sum_{i=1}^{N} \left(\frac{m_i - t_i}{\sigma_i}\right)^2 - \sum_{j=1}^{K} 2B_j r_j + \sum_{j,j'=1}^{K} A_{jj'} r_j r_{j'}, \tag{B.32}$$

where B_j is a vector with K components or $(K \times 1$ matrix),

$$B \rightarrow B_j = \sum_{i=1}^{N} \beta_{ji} (m_i - t_i)/\sigma_i^2, \tag{B.33}$$

and $A_{jj'}$ is a $K \times K$ symmetric matrix, is:

$$A \rightarrow A_{jj'} = \delta_{jj'} + \sum_{i=1}^{N} \beta_{ji}\beta_{j'i}/\sigma_i^2. \tag{B.34}$$

If we define the free parameters r_j as a $K \times 1$ matrix, then to minimize the χ^2 we get:

$$2\chi \frac{\partial \chi}{\partial r_{j'}} = -2B_{j'} + 2\sum_{j=1}^{K} A_{jj'}r_j = 0$$

$$\sum_{j=1}^{K} A_{jj'}r_j = B_{j'} \tag{B.35}$$

$$Ar = B$$

$$r = A^{-1}B.$$

Then the final expression of the χ^2 is:

$$\chi^2 = \sum_{i=1}^{N} (\frac{m_i - t_i}{\sigma_i})^2 - 2B^T r + r^T A r$$

$$= \sum_{i=1}^{N} (\frac{m_i - t_i}{\sigma_i})^2 - 2B^T A^{-1}B + (A^{-1}B)^T A A^{-1}B$$

$$= \sum_{i=1}^{N} (\frac{m_i - t_i}{\sigma_i})^2 - B^T A^{-1}B \tag{B.36}$$

$$= \sum_{i=1}^{N} (\frac{m_i - t_i}{\sigma_i})^2 - \sum_{j}^{K}\sum_{j'}^{K} B_j(A^{-1})_{jj'}B_{j'}.$$

Appendix C

Code Structure and Parameters

C.1 Location of computer codes

The data and simulation production follows the procedure of the 2009 inclusive jet analysis, see "offline/paper/psn0573" for details.

The dijet analysis follows the procuedure of the 2009 dijet analysis at mid-rapidity, see "offline/paper/psn0649" for details.

The code of this analysis is available here: "/star/u/tinglin/public/final_code/".

C.2 EEMC Gains Into the Simulation

For the 2009 pp 200 GeV data, the EEMC calibration was done much later than the embedding production, which means the EEMC trigger information may not be very precise in the simulation. A significant amount of computing time is needed to fully simulate the STAR detector response to a Pythia event, so an afterburner method was needed for the measurements in the EEMC region.

In order to implement the method, we need to figure out the program flow of the simulation. Simulation starts from the Pythia events (physics), which then go into Geant. The simulated energies are multiplied by the EMC tower gain factors from the database to get the corresponding ADC values, and then converted to the same format as the data. The ADC values are used in the

trigger simulator for the trigger category determination.

The idea is to recalculate the skim trees, which store all the trigger informations from the jet finder. The method is simple: change the tower adc to a new value by $Adc_{new} = Adc_{old} \times \frac{Gain_{new}}{Gain_{old}} +$ *pedestal* before the event goes into the trigger simulator. The key simulators for EEMC are the L2Emulator and EemcTriggerSimu. As shown in chapter 1, the data and simulation agreement is better after we implemented the new EEMC gains.

C.3 TMVA Parameters

The parameter settings for Multilayer Perceptron are:

- BookMethod(TMVA::Types::kMLP, "MLP", "!H:!V:VarTransform=Norm:NeuronType=tanh:
  NCycles=10000:HiddenLayers=N+100:EstimatorType=MSE:TestRate=10:
  LearningRate=0.02: NeuronInputType=sum:DecayRate=0.6:TrainingMethod=BFGS:
  Sampling=0.1:SamplingEpoch=0.8: ConvergenceImprove=1e-6:
  ConvergenceTests=15:!UseRegulator");

The parameter settings for Linear Discriminant (LD) are:

- BookMethod(TMVA::Types::kLD, "LD","!H:!V:VarTransform=None");

The parameter settings for K-Nearest Neighbour (KNN) are:

- BookMethod(TMVA::Types::kKNN, "KNN","nkNN=20:ScaleFrac=0.8:SigmaFact=1.0:
  Kernel=Gaus:UseKernel=F:UseWeight=T:!Trim");

Bibliography

[1] Star 2009 eemc mip calibration.

[2] Charged jet cross sections and properties in proton-proton collisions at $\sqrt{s} = 7$ TeV. *Phys. Rev. D*, 91:112012, Jun 2015.

[3] Abelev et al. Longitudinal double-spin asymmetry for inclusive jet production in $\vec{p} + \vec{p}$ collisions at $\sqrt{s} = 200$ GeV. *Phys. Rev. Lett.*, 100:232003, Jun 2008.

[4] K. H. Ackermann et al. STAR detector overview. *Nucl. Instrum. Meth.*, A499:624–632, 2003.

[5] L. Adamczyk et al. Longitudinal and transverse spin asymmetries for inclusive jet production at mid-rapidity in polarized $p + p$ collisions at $\sqrt{s} = 200$ GeV. *Phys. Rev.*, D86:032006, 2012.

[6] L. Adamczyk et al. Neutral pion cross section and spin asymmetries at intermediate pseudorapidity in polarized proton collisions at $\sqrt{s} = 200$ GeV. *Phys. Rev. D*, 89:012001, Jan 2014.

[7] L. Adamczyk et al. Precision measurement of the longitudinal double-spin asymmetry for inclusive jet production in polarized proton collisions at $\sqrt{s} = 200$ GeV. *Phys. Rev. Lett.*, 115:092002, Aug 2015.

[8] L. Adamczyk et al. Measurement of the cross section and longitudinal double-spin asymmetry for dijet production in polarized pp collisions at $\sqrt{s} = 200$ GeV. *Phys. Rev. D*, 95:071103, Apr 2017.

[9] S. Agostinelli et al. GEANT4: A Simulation toolkit. *Nucl. Instrum. Meth.*, A506:250–303, 2003.

[10] Ahmed Ali and Gustav Kramer. Jets and QCD: A Historical Review of the Discovery of the Quark and Gluon Jets and its Impact on QCD. *Eur. Phys. J.*, H36:245–326, 2011.

[11] Richard D. Ball, Valerio Bertone, Stefano Carrazza, Luigi Del Debbio, Stefano Forte, Alberto Guffanti, Nathan P. Hartland, and Juan Rojo. Parton distributions with QED corrections. *Nucl. Phys.*, B877:290–320, 2013.

[12] F. S. Bieser et al. The STAR trigger. *Nucl. Instrum. Meth.*, A499:766–777, 2003.

[13] Gerald C. Blazey et al. Run II jet physics. In *QCD and weak boson physics in Run II. Proceedings, Batavia, USA, March 4-6, June 3-4, November 4-6, 1999*, pages 47–77, 2000.

[14] Matteo Cacciari and Gavin P. Salam. Pileup subtraction using jet areas. *Phys. Lett.*, B659:119–126, 2008.

[15] Matteo Cacciari, Gavin P. Salam, and Gregory Soyez. The anti- k t jet clustering algorithm. *Journal of High Energy Physics*, 2008(04):063, 2008.

[16] Matteo Cacciari, Gavin P. Salam, and Gregory Soyez. The Anti-k(t) jet clustering algorithm. *JHEP*, 04:063, 2008.

[17] Matteo Cacciari, Gavin P. Salam, and Gregory Soyez. FastJet User Manual. *Eur. Phys. J.*, C72:1896, 2012.

[18] Zilong Chang. Gluon Polarization in Longitudinally Polarized *pp* Collisions at STAR. *Int. J. Mod. Phys. Conf. Ser.*, 40:1660021, 2016.

[19] Daniel de Florian, Stefano Frixione, Adrian Signer, and Werner Vogelsang. Next-to-leading order jet cross sections in polarized hadronic collisions. *Nuclear Physics B*, 539(3):455 – 476, 1999.

[20] Daniel de Florian, Rodolfo Sassot, Marco Stratmann, and Werner Vogelsang. Evidence for polarization of gluons in the proton. *Phys. Rev. Lett.*, 113:012001, Jul 2014.

[21] S. Frixione, Z. Kunszt, and A. Signer. Three-jet cross sections to next-to-leading order. *Nuclear Physics B*, 467(3):399 – 442, 1996.

[22] Andreas Hocker et al. TMVA - Toolkit for Multivariate Data Analysis. *PoS*, ACAT:040, 2007.

[23] Liaoyuan Huo. In-Jet Tracking Efficiency Analysis for the STAR Time Projection Chamber in Polarized Proton-Proton Collisions at sqrt(s) = 200GeV. Master's thesis, Texas A&M University, (2012).

[24] Hal Spinka Bernd Surrow James Hayes-Wehle, Joe Seele. Relative luminosity analysis for run9 pp 200 gev running. Nov. 2012.

[25] J. Kiryluk. Local polarimetry for proton beams with the STAR beam beam counters. In *Spin physics. Polarized electron sources and polarimeters. Proceedings, 16th International Symposium, SPIN 2004, Trieste, Italy, October 10-16, 2004, and Workshop, PESP 2004, Mainz, Germany, October 7-9, 2004*, pages 718–721, 2005.

[26] Ting Lin. Longitudinal Double-Spin Asymmetries for Forward Di-jet Production in Polarized *pp* Collisions at $\sqrt{s}$ = 200 GeV. In *22nd International Symposium on Spin Physics (SPIN 2016) Urbana, IL, USA, September 25-30, 2016*, 2017.

[27] A. D. Martin, W. J. Stirling, R. S. Thorne, and G. Watt. Parton distributions for the LHC. *Eur. Phys. J.*, C63:189–285, 2009.

[28] Emanuele R. Nocera, Richard D. Ball, Stefano Forte, Giovanni Ridolfi, and Juan Rojo. A first unbiased global determination of polarized pdfs and their uncertainties. *Nuclear Physics B*, 887:276 – 308, 2014.

[29] C. Patrignani et al. Review of Particle Physics. *Chin. Phys.*, C40(10):100001, 2016.

[30] Gavin P. Salam. Towards Jetography. *Eur. Phys. J.*, C67:637–686, 2010.

[31] Peter Z. Skands. The Perugia Tunes. In *Proceedings, 1st International Workshop on Multiple Partonic Interactions at the LHC (MPI08): Perugia, Italy, October 27-31, 2008*, pages 284–297, 2009.

[32] D. Stump, J. Pumplin, R. Brock, D. Casey, J. Huston, J. Kalk, H. L. Lai, and W. K. Tung. Uncertainties of predictions from parton distribution functions. i. the lagrange multiplier method. *Phys. Rev. D*, 65:014012, Dec 2001.

[33] S. Mrenna T. Sjostrand and P. Z. Skands. Pythia 6.4 physics and manual. *Journal of High Energy Physics*, 2006(05):026, 2006.